SANDIA REPORT

SAND2018-10612
Unlimited Release
Printed September, 2018

X-Ray Diffraction Measurements on Laser-Compressed Polycrystalline Samples Using a Short-Pulse Laser Generated X-Ray Source

LDRD 191235

Marius S. Schollmeier, Tommy Ao, Ella S. Field, Benjamin R. Galloway, Patricia Kalita, Mark W. Kimmel, Joel Long, Dane V. Morgan, Patrick K. Rambo, Jens Schwarz, Christopher T. Seagle

Prepared by
Sandia National Laboratories
Albuquerque, New Mexico 87185 and Livermore, California 94550

Sandia National Laboratories is a multimission laboratory managed and operated by National Technology
and Engineering Solutions of Sandia, LLC., a wholly owned subsidiary of Honeywell International, Inc.,
for the U.S. Department of Energys National Nuclear Security Administration under contract DE-NA0003525.

Sandia National Laboratories

Issued by Sandia National Laboratories, operated for the United States Department of Energy by National Technology and Engineering Solutions of Sandia, LLC.

Printed in the United States of America. This report has been reproduced directly from the best available copy.

Available to DOE and DOE contractors from
U.S. Department of Energy
Office of Scientific and Technical Information
P.O. Box 62
Oak Ridge, TN 37831

Telephone: (865) 576-8401
Facsimile: (865) 576-5728
E-Mail: reports@osti.gov
Online ordering: http://www.osti.gov/scitech

Available to the public from
U.S. Department of Commerce
National Technical Information Service
5301 Shawnee Rd
Alexandria, VA 22312

Telephone: (800) 553-6847
Facsimile: (703) 605-6900
E-Mail: orders@ntis.gov
Online ordering: https://classic.ntis.gov/help/order-methods/

SAND2018-10612
Printed September, 2018
Unlimited Release

X-Ray Diffraction Measurements on Laser-Compressed Polycrystalline Samples Using a Short-Pulse Laser Generated X-Ray Source

Marius S. Schollmeier, Ella S. Field, Benjamin R. Galloway,
Mark W. Kimmel, Patrick K. Rambo, Jens Schwarz
Laser Operations and Engineering Department

Tommy Ao, Patricia Kalita, Christopher T. Seagle
Dynamic Material Properties Department

Sandia National Laboratories
P. O. Box 5800, Albuquerque, New Mexico 87185-1192

Dane V. Morgan
Mission Support and Test Services LAO
2900 East Road, Los Alamos, New Mexico 87544

Joel Long
Model World LLC, 12129 Menaul Blvd NE, Apt. 3
Albuquerque, New Mexico 87112

Abstract

Existing models for most materials do not describe phase transformations and associated lattice dynamics (kinetics) under extreme conditions of pressure and temperature. Dynamic x-ray diffraction (DXRD) allows material investigations *in situ* on an atomic scale due to the correlation between solid-state structures and their associated diffraction patterns. In this LDRD project we have developed a nanosecond laser-compression and picosecond-to-nanosecond x-ray diffraction platform for dynamically-compressed material studies. A new target chamber in the Target Bay in building 983 was commissioned for the ns, kJ Z-Beamlet laser (ZBL) and the 0.1 ns, 250 J Z-Petawatt (ZPW) laser systems, which were used to create 8-16 keV plasma x-ray sources from thin metal foils. The 5 ns, 15 J Chaco laser system was converted to a high-energy laser shock driver to load material samples to GPa stresses. Since laser-to-x-ray energy conversion efficiency above 10 keV is low, we employed polycapillary x-ray lenses for a 100-fold fluence increase compared to a conventional pinhole aperture while simultaneously reducing the background significantly. Polycapillary lenses enabled diffraction measurements up to 16 keV with ZBL as well as diffraction experiments with ZPW. This x-ray diffraction platform supports experiments that are complementary to gas guns and the Z facility due to different strain rates. Ultimately, there is now a foundation to evaluate DXRD techniques and detectors in-house before transferring the technology to Z.

This page intentionally left blank.

ACKNOWLEDGMENTS

The authors express their great appreciation to staff and management for their help and support during this project: Darrell Armstrong, Anthony Colombo, Raymond Fasano, Matthias Geissel, Damon Kletecka, Quinn Looker, Jonathon Shores, Ian Smith, Shane Speas, John Stahoviak, Jamison Wagner for technical advice and support in all matters regarding facility build-out, WP&C, laser operations, and engineering; Roger Harmon, Daniel Headley, Jeff Kellogg, Andrew Maurer, Grafton Robertson for mechanical engineering & hardware support, as well as safety documentation; Dan Dolan, Brian Esquibel, Sheri Payne for their support designing and building the PDV system and expertise in fiber optics; Nicole Cofer, Randy Hickman, Keith Hodge, Joshua Usher, Tim Webb for target & diagnostics fabrication; Levi Cortez, Jeff Georgeson, Drew Johnson, Aaron Lombrozo, for their motion and shot control support; Gary Cooper, Kelly Hahn, Sara Pelka for simulation support and valuable discussion about the nature of the ZPW background; John Benage, Dawn Flicker, Brent Jones, Michael Jones, John Porter, Greg Rochau, Daniel Sinars for their enthusiastic support of the project and its required infrastructure developments, the quarterly meetings and general oversight of the project.

This work was sponsored by the Laboratory Directed Research and Development (LDRD) Program at Sandia National Laboratories.

This page intentionally left blank.

TABLE OF CONTENTS

FIGURES

TABLES

NOMENCLATURE AND ACRONYMS

CAD	Computer-Aided Design
CCD	Charge-coupled device
(h)CMOS	(hybrid) complementary metal-oxide-semiconductor [camera]
CRITR	Compact, Rugged In-chamber TRansmission spectrometer
DOE	Department of Energy
DXRD	Dynamic X-ray Diffraction
FOA	Final Optics Assembly
FOV	Field of View
FWHM	Full Width at Half Maximum
HEDP	High Energy Density Physics
IP	Image Plate
keV	kilo-Electron volt
LDRD	Laboratory Directed Research & Development [project]
LOS	Line of Sight
MeV	Mega-Electron volt
PACMAN	Phase and Crystallographic Measurement ANalyzer diagnostic
PI	Principal Investigator
PDV	Photonic Doppler Velocimetry
SNL	Sandia National Laboratories
SPC	Single Photon Counter camera
TCC	Target chamber center
WP&C	Work Planning and Control
XRD	X-ray Diffraction
Z	Z Pulsed Power Facility [located in bldg. 983]
ZBL	Z-Beamlet Laser [located in bldg. 986]
ZPW	Z-Petawatt Laser [located in bldg. 986]

This page intentionally left blank.

1. EXECUTIVE SUMMARY

1.1 Purpose

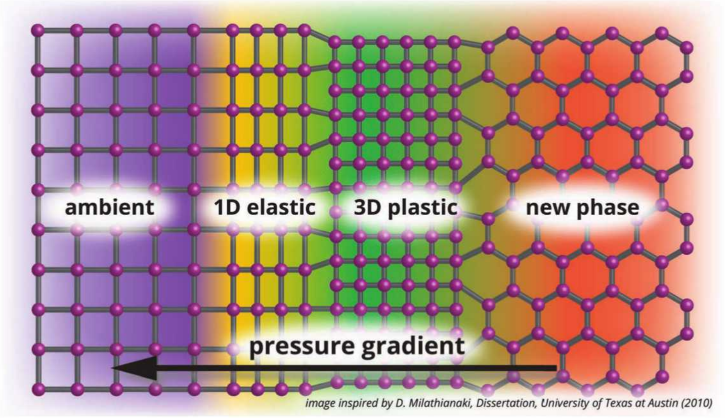

Figure 1.1. Cartoon of crystal phase transitions during dynamic compression.

Detection of material phases is a powerful constraint for models of high pressure applications. Under dynamic compression, materials may be loaded to stresses above phase transition pressures known from static studies, on time scales of nanoseconds to microseconds. Existing models for most materials do not describe the kinetics or time-dependent nature of phase transitions under dynamic loading; dynamic phase transitions may be different from static ones and material properties can be affected by the kinetics of nanosecond to microsecond-scale compressions. Exploring the material structural dynamics can be performed with x-ray diffraction (XRD) since it provides explicit information of a solid's crystallographic structure. X-ray diffraction data from dynamically compressed samples are extremely valuable as they provide a direct measurement of the elastic compression of the crystal lattice, onset of plastic flow, strength-strain-rate dependence, phase transitions, and density of crystal defects.

In-situ dynamic x-ray diffraction (DXRD) is being performed on explosive-driven (e.g.,[1]), gas gun (e.g., [2–6]) and laser-driven shock experiments (e.g., [7–10]) in various forms including Bragg reflection from single crystals or powders (e.g., [11–14]) and quasi-white light Laue diffraction (e.g., [15–17]). Sandia's Z Pulsed Power Facility ("Z") [18, 19] has the capability to create shock and ramp compressed states [20–22] at much higher pressures than achievable using gas guns, and with greater uniformity, larger size and longer duration than laser-driven experiments. The long-term goals of the Science Program at Sandia include the development of an x-ray diffraction capability for Z to measure whether materials are undergoing a phase change while under compression in order to validate models. Accordingly, the key scientific development goal addressed by this Laboratory Directed Research and Development (LDRD) project is to determine the suitability of a laser-driven x-ray source for XRD on Z.

1.2 Goals

The overarching technical deliverables of this project were aimed to establish a test platform in the Z-Backlighter Target Bay [23] for time-resolved, x-ray diffraction measurements on dynamically compressed, high-atomic-number polycrystalline matter. This platform benefits from a higher laser shot rate compared to Z. Nominally, Z performs 1 shot per work day (as limited by daily operational processes) while the Z-Beamlet (ZBL) [24, 25] and Z-Petawatt (ZPW) [26, 27] lasers can fire up to 3 shots per day each (as limited by the thermal loading of the main amplifiers). The scarcity of Z shots for development and the extra capacity of laser shots motivates having stand-alone capabilities in addition to Z in order to scope and develop new experimental methods and applications. It utilizes the same laser systems to create the x-ray source as Z, hence development results are directly transferable to Z experiments. Furthermore, this compression platform is complementary to experiments utilizing gas guns or Z to compress the sample, which allows the investigation of phase transition kinetics under different strain rates.

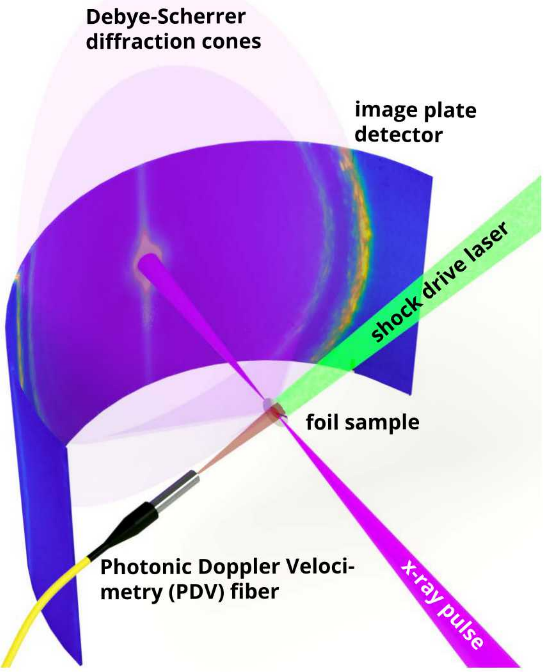

Figure 1.2. Concept of DXRD experiment developed in this project.

1.3 Approach and Summary of Results

Lacking Z to perform the compression, material samples were to be compressed using a separate, ns-duration laser pulse. Laser compression is a technique to dynamically load samples at high pressures for equation-of-state studies. Laser irradiances required to reach GPa pressures are in the range of 10^{10}- 10^{12} W/cm^2 [11, 28]. The Chaco and Z-Petawatt (ZPW) laser systems at Sandia are well suited to load material samples to GPa stresses using laser compression and to probe them with high-energy K_α x-rays for time-gated x-ray diffraction measurements during compression. Our approach was to activate the Chama target chamber for these experiments, which had not been used for experiments before (see Sec. 3.1). We prepared the Chaco laser system for high-energy

($\approx$10 – 20 J) operation with >4 ns pulses at the Chama target chamber (see Sec. 3.2), and used it to shock-load samples (Sec. 5.1). Laser compression was benchmarked with aluminum calibration samples, diagnosed with Photonic Doppler Velocimetry (PDV), see Sec. 3.4.

The high-risk, high-payoff nature of our R&D lies in the approach of performing time-gated DXRD measurements with hard x-ray pulses created by a high-energy short-pulse laser system, something that has not been done before at a large-scale facility. Additionally, in contrast to most other short-pulse laser systems that use off-axis parabolic mirrors for final focusing of the laser pulse, ZPW was set up to be focused with a lens (see Sec. 3.3.1). Lens-based focusing was investigated because it would simplify future ZPW alignment at Z and enables the use of traditional glass vacuum windows and debris shields for operational safety. The difficulty of this approach lies in the fact that lens-based focusing requires comparatively long laser pulses of about 100 ps, but K_α x-ray generation requires near-10^{18} W/cm^2 laser intensity, which is traditionally achieved by shortening the laser pulse to a few ps. It was not known if hard x-rays, such as K_α x-rays from period-5 transition metals in the range of 15-25 keV, can be created efficiently with such long laser pulses and with a high enough yield to generate an XRD pattern. Hard x-rays are needed to penetrate high-atomic-number samples by more than a few microns. Results of our investigations are presented in Sec. 5. We have demonstrated static diffraction patterns generated with ZPW at 8 keV, but were not yet successful with 16 keV x-rays. We have found that the laser generates a higher-than-expected, high-energy radiation background when it irradiates a target, which requires more than 1 inch of tungsten to block and which requires a larger-than-planned standoff between x-ray source and diffraction sample. X-ray optics in the form of polycapillary x-ray lenses (see Sec. 3.6) were utilized to mitigate this issue. X-ray polycapillary lenses are very efficient x-ray optics that offer a large collection solid angle and can be used to focus x-rays over several feet distance. Photometric calculations were benchmarked to the experimental data. Sec. 4.3 discusses the expected signal levels for current and future laser capabilities. The results suggest that a polycapillary optic in combination with an x-ray source generated by ZPW at maximum intensity ($\approx 10^{20}$ W/cm^2, $\approx$500 J/500 fs or 1 kJ/1 ps) could yield sufficient detector signal for DXRD on high-Z samples.

As a short-term workaround to the issues encountered with ZPW, we demonstrated that, despite expectations due to the low conversion efficiency, the nanosecond, kJ Z-Beamlet laser can be used to generate 16 keV XRD patterns from a Zr sample. While ZBL's laser-to-x-ray conversion efficiency at this x-ray energy is much lower than ZPW's (see Sec. 5.2.3), the experiment is virtually background-free and a diffraction pattern with only a few photons per pixel exposure could be measured.

This page intentionally left blank.

2. PROJECT MANAGEMENT

Contrary to waterfall project management methodologies, which require detailed planning and task estimates before the execution begins (e.g., construction projects), the nature of this LDRD made it impossible to estimate activity durations accurately—much less the tasks needed to complete the solution. Agile project management was deemed not suitable for this project as the tasks included complex dependencies and the team consisted of non-interchangeable experts with clear roles and responsibilities, both of which required careful task planning and coordination. We chose an adaptive project management approach [29] as a hybrid between waterfall and agile project management practices.

2.1 Project Management Plan

The general goals of this project and suggested path towards reaching these goals were documented in the LDRD proposal, which served as our project charter. The project management plan further included the work breakdown structure (WBS) as our scope baseline, a project schedule baseline, stakeholder register, risk register, and an issue log. The WBS deliverables were derived by the team from the charter and used as a guide to keep the project focused on these deliverables. The actual activities to complete the WBS were planned and developed as we went along, by learning from outcomes from previous stages in the project. The initial duration estimate was made by the team and entered in project management software (Merlin Project). This software was used to visualize task inter-dependencies (Gantt chart or network diagram), to develop the critical path and to track task completion, as well as to communicate progress amongst the team and stakeholders. A web-based wiki software (Atlassian Confluence) was used to document meeting minutes, experiment results and miscellaneous notes. The risks (threats and opportunities) identified during the project were collected and tracked in a spreadsheet. An issue log was kept, logging the major issues encountered, their impact on the triple constraint (scope/schedule/cost, mainly schedule and scope here), and lessons learned for each issue. The PI kept a changelog for the first months, but this practice was quickly abandoned because it did not add value.

2.2 Scope of Work and WBS

The WBS consisted of the four main deliverables:

1. Create a laser-shock compression platform to dynamically load samples at high pressures for equation-of-state studies.
2. Develop a short-pulse x-ray source suitable for diffraction experiments.
3. Demonstrate multi-pulse x-ray diffraction on dynamically compressed targets.
4. Develop simulation capabilities for dynamic diffraction experiments to predict phase transition dynamics.

The work packages required to complete these deliverables are shown below. Sec. 2.3 shows the schedule to complete the WBS as estimated at the beginning of the project. Due to various issues encountered during the project, the actual and completed scope changed significantly, which is documented in Sec. 2.4.

Work Breakdown Structure

1. Create a laser compression platform to dynamically load samples at high pressures for equation-of-state studies by Q1/CY2016, which includes:
    - 1.1. Convert the Chaco laser system to a high-energy shock driver at the Chama target chamber, which includes:
        - 1.1.1. Install beam transport tubes and complete pressure safety documentation
        - 1.1.2. Design and develop a final focusing optic that generates a flat-top focal spot of sufficient intensity to drive a shock
        - 1.1.3. Develop a temporal laser pulse profile to hold the sample pressure constant over several nanoseconds
    - 1.2. Complete work planning and control process and obtain work authorization for laser-drive experiments at the Chama target chamber
    - 1.3. Integrate existing Photonic Doppler Velocimetry (PDV) system to infer material pressures during dynamic compression
    - 1.4. Perform laser compression experiments with calibration samples to develop scaling relation of sample pressure vs. laser input drive parameters
2. Develop a short-pulse x-ray source suitable for diffraction experiments by end of Q3/CY2016, which includes:
    - 2.1. Commission the Chama target chamber for short-pulse laser operation, which includes:
        - 2.1.1. Complete the work planning and control process and obtain work authorization for Chama experiments
        - 2.1.2. Demonstrate multi-pulse high-energy ZPW operation with lens-based focusing at the Chama target chamber
    - 2.2. Develop and field diagnostics to characterize the x-ray source w.r.t. yield and laser-to-x-ray conversion efficiency, spectrum, and signal-to-background ratio
    - 2.3. Perform material scans (e.g., Cu, Ge, Zr, Mo, Ag, Sn) to find the best x-ray source for DXRD
3. Demonstrate multi-pulse x-ray diffraction on dynamically compressed targets by end of Q3/CY2018, which includes:
    - 3.1. Develop a platform for dynamic diffraction experiments, which includes:
        - 3.1.1. Collect and document requirements for an integrated experiment

    - 3.1.2. Design, procure and test the new instrument
    - 3.1.3. Develop data reduction procedures to infer material parameters from the measured two-dimensional diffraction patterns
  - 3.2. Perform single pulse x-ray diffraction with ZPW, which includes:
    - 3.2.1. Integrate the Chaco laser into the facility shot control software to enable combined laser shots with ZPW or ZBL
    - 3.2.2. Conduct integrated shots using a single x-ray pulse generated by ZPW
    - 3.2.3. Demonstrate the capability to map out the material phase transition in ns steps by performing repeated shots with changing delays
  - 3.3. Develop and demonstrate a multi-pulse x-ray diffraction capability, which includes:
    - 3.3.1. Design and implement ZPW multi-pulse operation
    - 3.3.2. Verify multi-pulse x-ray source performance with a time-resolving detector
    - 3.3.3. Desgin and implement a multi-frame detector system
    - 3.3.4. Conduct multi-pulse dynamic diffraction experiments

4. Develop simulation capabilities for dynamic diffraction experiments, which includes:
  - 4.1. Benchmark a rad-hydro simulation code for laser-compression experiments
  - 4.2. Develop a dynamic diffraction simulation code to predict diffraction spectra vs. time
  - 4.3. Develop the capability to match the data with simulations and predict phase transition dynamics

2.3 Project Baseline Schedule and Milestones

The initially estimated time line is displayed as a Gantt chart in Fig. 2.1. The four main deliverables are highlighted in bold font; the milestones are displayed as diamonds. The project started on October 1st, 2015. Starting with WBS elements 1.1–1.4, our initial estimate was that the Chaco laser could be activated quickly as most components for the vacuum beam transport pipes and final focusing optics could be bought quickly. It was estimated that writing the required work planning and control (WP&C) documentation (i.e., pressure safety data package, technical work documents) could be completed by December 1st, 2015. By this time the existing PDV system would have been moved and installed at the Chama chamber. Shock compression experiments would be performed for three months with the goal of developing a pressure scaling relation vs. drive laser parameters for calibration samples (e.g., aluminum).

It was further assumed (WBS 2.1) that the large-format laser optics and required mounting hardware plus motion controls were in place and ready to be commissioned when this project started. Thus, in order to commission the Chama chamber, WP&C documentation had to be completed (WBS 2.1.1), with the goal to demonstrate lens-based focusing of a high-energy ZPW pulse by March 1st, 2016.

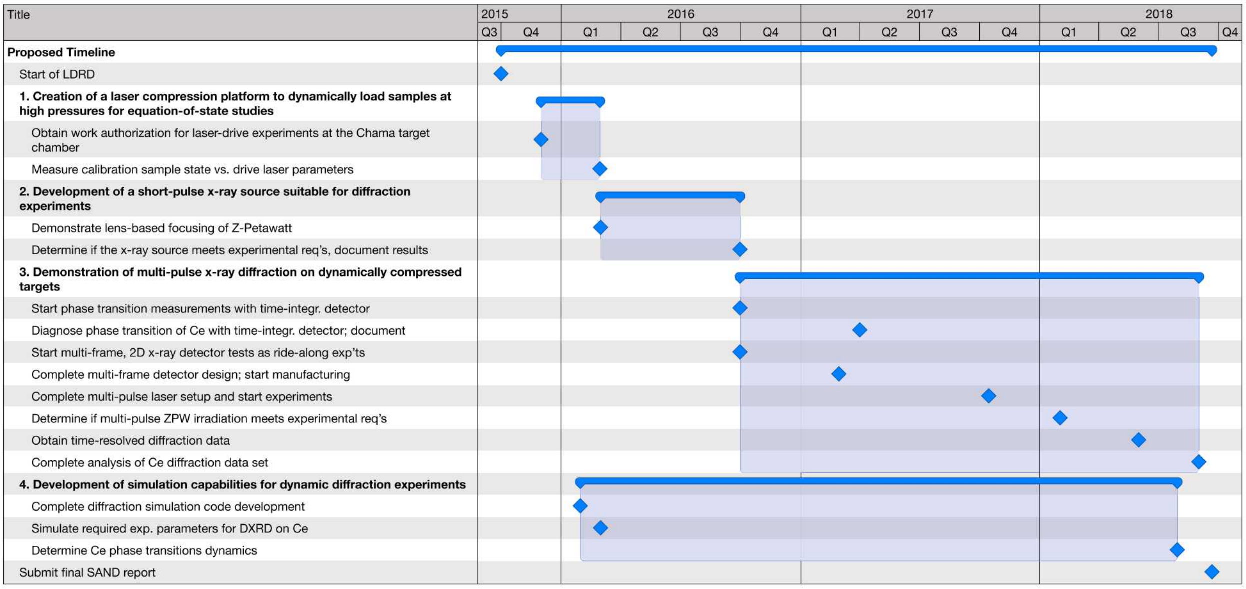

Figure 2.1. Initial time line and completion of milestones (◆) estimated at project start. Time is given in calendar years, not fiscal years.

The goal for WBS item 3 was to develop an instrument (sample and detector enclosure) using a time-integrating detector (image plate) in the first year, then start experiments after ZPW commissioning on September 30th, 2016 and detect a phase transition (e.g., the $\gamma - \alpha$ phase transition in cerium, see Sec. 4.4) half a year later by April 1st, 2017.

Simultaneously with the start of time-integrated experiments we would do ride-alongs with time-gated or time-resolving detectors, such as a scintillator and relay optic system or gated CCD camera. Here, the goal was to decide by end of February 2017 which detector system performed best. After that, we planned to design and procure a suitable experimental platform and convert the ZPW laser to double-pulse operation using a concept shown in the proposal presentation. These activities would be completed by October 15th, 2017, which also marked the starting point for multi-pulse experiments. We set the goal to determine if double-pulse operation with ZPW produces a source that meets the requirements for DXRD four months later by February 1st, 2018, and if it did, obtain time-resolved DXRD data by June 1st, 2018.

During these experimental activities we would work on simulation capabilities (WBS deliverable 4). As stated in the WBS, we had planned to develop rad-hydro simulation capabilities to get more insights into laser-compression experiments and to develop scaling relations. We needed a DXRD simulation code that takes the input from the rad-hydro code or experimental data to predict diffraction patterns and guide experiments. These activities were planned to be completed by March 1st, 2016 and then used throughout the experiments. Towards the end of the LDRD, if everything would go as planned, we would use these codes to learn more about phase transition kinetics of Ce. Finally, for late Summer 2018 we had planned to write this report and submit it in September 2018, which marks the closing date of this LDRD.

2.4 Actual Project Schedule and Milestones

The actual project schedule reflects the impact of several issues that occurred during this project. Many of the risks identified as threats to the project schedule did occur, and workarounds had to be developed. Within the first months of the project two major issues were identified: i) the already-existing Photonic Doppler Velocimetry (PDV) system could not be integrated into the Z-Backlighter laser facility (see Sec. 3.4), which delayed the milestone to determine the calibration sample pressure, and ii) completion of the ZPW beam transport to the Chama chamber would be significantly delayed due to various issues that were out of the control of this project.

The Chama activation delay created a chain of changes, both in schedule and scope. We decided to change the scope for the first year by exploiting the opportunity of reactivating the 100 TW target chamber for ZPW shots instead of waiting for the Chama completion. We could start x-ray source characterization and XRD measurements on June 28th, 2016. The first XRD pattern was obtained on February 2nd, 2017, 5 months later than initially estimated. This was still significantly quicker than had we waited for the Chama chamber: The first ZPW target shot into Chama would not occur before August 15th, 2017—14 months later than planned. The majority of this delay was due to programmatic reprioritizations, which impacted the schedules for optics coating, installation and implementation of motion control. On our side, creating the WP&C documents took longer than anticipated because the additional hazards (i.e., vacuum, radiation) created by routing ZPW to Chama required a complete rewrite of existing technical work documents and procedures, including their approval by various stakeholders. The completion of the last milestone of this activity, determining if a short-pulse-laser-generated x-ray source is suitable for diffraction, was completed 9 months after the first ZPW shot into Chama occurred (vs. 7 months planned).

At the same time, we identified the opportunity that polycapillary x-ray lenses offered for XRD. These lenses can be used to increase the x-ray flux from a source to the diffraction sample by at least ten times (see Sec. 3.6) compared to a pinhole collimator. This opportunity resulted in a significant scope change for the second year and considerable time was spent procuring, characterizing and testing these optics. These activities changed the focus of attention from activating Chama and characterizing the source to developing an off-line polycapillary lens alignment procedure and integration into our XRD experiment. The work on the polycapillary optic was prioritized over Chama activation because we discovered during the first 100 TW experiments that without the polycapillary lens the background on the detector was many times larger than the signal. Hence, what was an opportunity at first quickly became a requirement. The overall development, testing and integration of polycapillary lenses into our XRD experiment took about 12 months.

The issue of significant background in ZPW shots further dictated the addition of dedicated background characterization experiments to the scope. First measurements started at 100 TW and continued at Chama into early 2018. Sec. 5.4 provides a detailed description of these experiments and supporting simulations. The continuing background issues in ZPW experiments led us to search for other options to make progress on DXRD experiments. An obvious choice was to switch from using ZPW to ZBL to create the x-ray source. This scope change was added to the project, and ZBL diffraction shots began on October 26th, 2017. We discovered that ZBL, in conjunction with a polycapillary lens, can be used to perform XRD at 16 keV. Because of this result and the higher chances of success, we decided to change scope again and use ZBL instead of ZPW for the first dynamic diffraction shots with Chaco.

Integrated diffraction shots with Chaco were not only delayed due to source development issues. The main setback was that shortly after Chaco's legacy shot control system had been integrated into the facility shot control software, the main hardware control unit of Chaco broke during a combined ZBL/Chaco test shot on October 7th, 2016. First repair attempts of the more than 30-year-old control unit failed. The manufacturer had stopped support decades ago, and replacement parts were unavailable. The decision was made to replace the outdated control unit with an in-house solution using modern hardware that could be maintained by Sandia. Overall it took about 21 months before Chaco was ready again to fire an amplified shot with ZBL or ZPW into Chama. The first integrated DXRD shot with Chaco and ZBL was performed on July 26th, 2018.

Since we encountered severe issues in activating the various lasers and diagnostics, as well as unexpected background issues, task 3.3 of the WBS (multi-pulse XRD) had to be lowered in priority. We had performed ride-along shots with a detector capable of multi-frame operation, but first results did not look promising. Work on this task was stopped in early 2018 to focus on implementing integrated Chaco and ZBL/ZPW shots in Chama.

The development of DXRD simulation capabilities suffered a similar fate. A simulation code showing the change of diffraction patterns vs. sample pressure and phase was developed. Further development had to be put on hold because experimental data for comparisons and benchmarks were not available. We expect that interest in simulation results will rise again once data from integrated DXRD experiments after this LDRD will be available.

3. EXPERIMENTAL CAPABILITIES DEVELOPMENT

3.1 Chama Vacuum Chamber

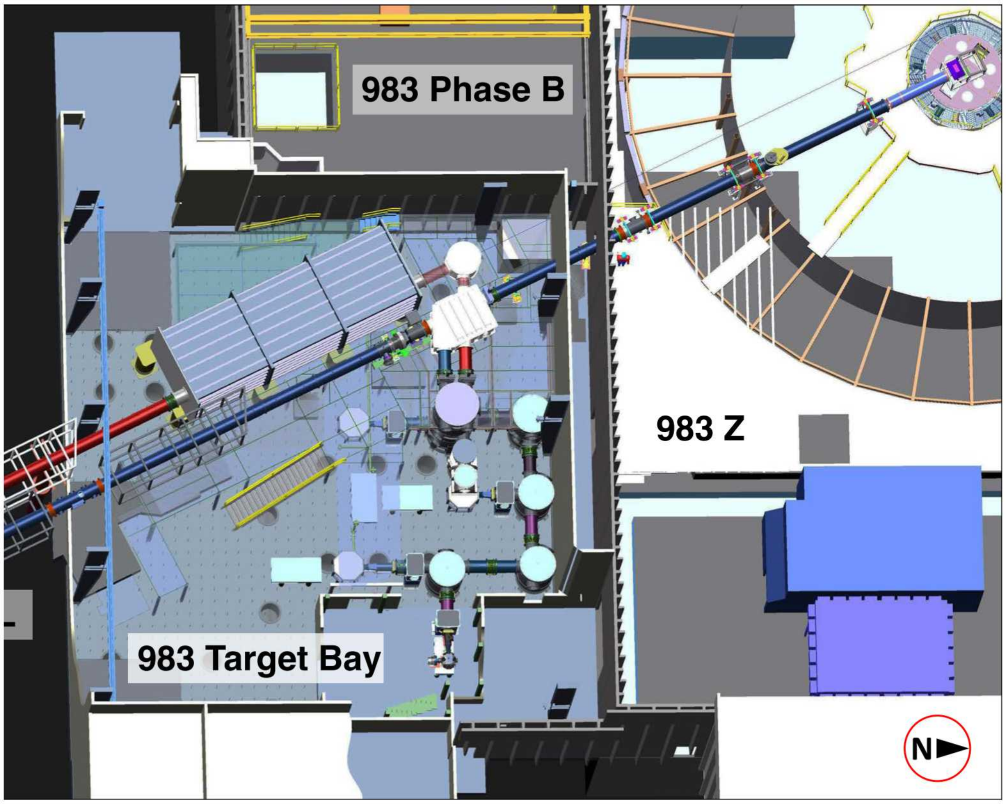

Figure 3.1. Location of the Target Bay in Bldg. 983, Phase C.

A large part of this project was the preparation of the Chama target chamber for experiments, including commissioning of the ZBL, ZPW and Chaco laser beam paths. The Chama target chamber is located in the Target Bay in building 983, south of the Z machine. (see Fig. 3.1). The Z-Backlighter Facility, where both ZBL and ZPW are located, is south of the Target Bay (left in the picture). Both laser beams enter the Target Bay on the upper mezzanine (red beam pipe for ZPW, blue beam pipe for ZBL). ZPW is routed to the vacuum compressor chamber, inside of which a pair of gratings are used to compress the pulse to about 100 ps. After the compressor, the ZPW pulse can be guided to Z or to the Chama target chamber. ZBL has a "straight shot" to the Z machine, or it can be routed to the Target Bay target chambers.

Fig. 3.2 shows a more detailed overview of the Target Bay. The 5 local stand-alone vacuum target chambers, named for New Mexico rivers, each have different emphasis, which allows several experimental campaigns to take place in parallel. The 1.5-m octagonal Chama target chamber is located in the center of the Target Bay, and is the only target chamber (other than Z) that can accommodate the short-pulse ZPW laser at its full energy. Due to the expected high-energy radiation background during a ZPW target shot, the Chama chamber is made out of 4-inch thick stainless steel, including the doors. The otherwise identical Jemez and Pecos target chambers have 2-inch thick aluminum doors. A fourth target chamber, Conchas, is the only one currently with access to a 30-T magnetic-field pulser for studying magnetized HEDP conditions. Details about the Target Bay and recent laser developments have been reported in [23, 30].

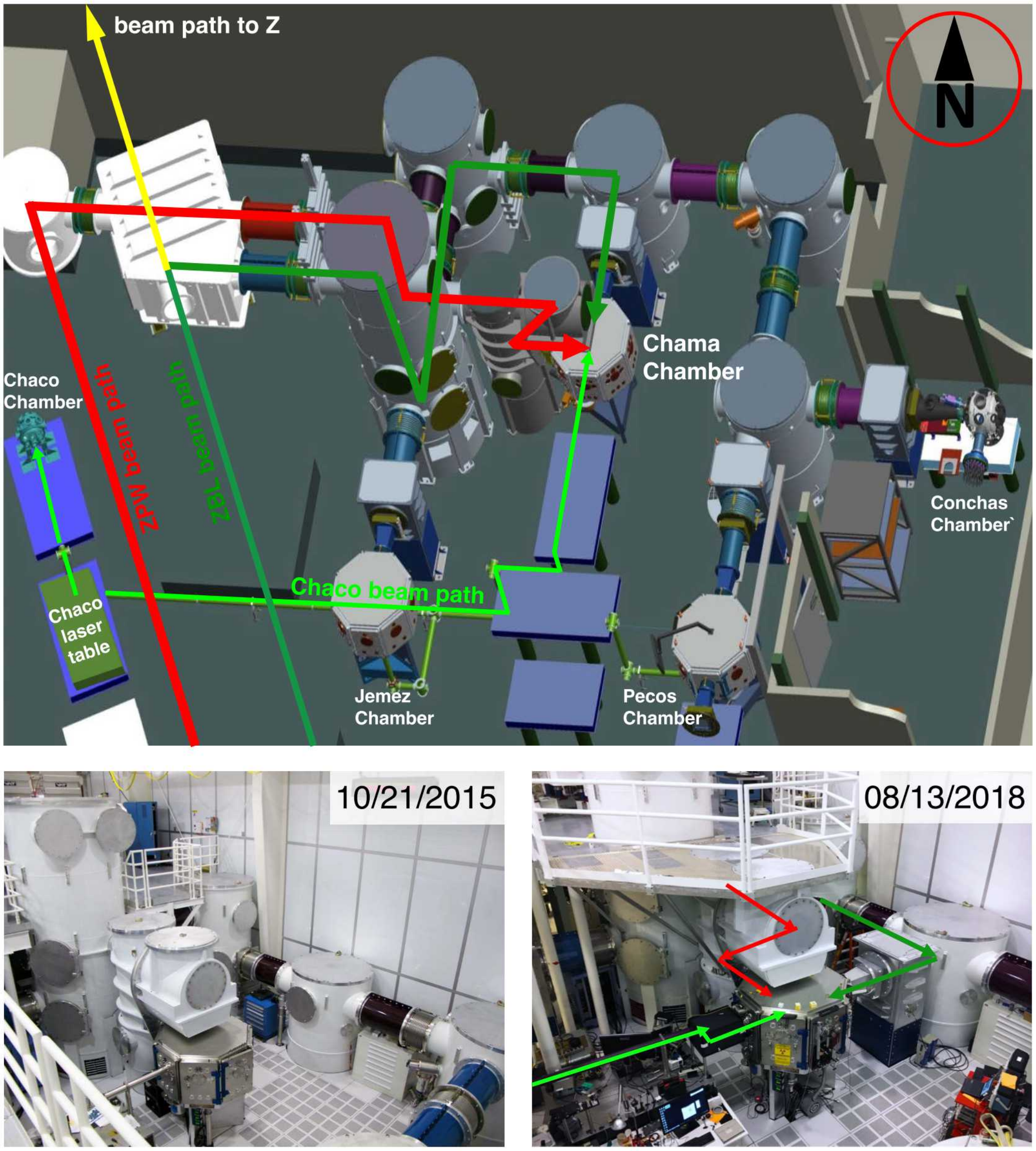

Figure 3.2. Bird's eye view of the Target Bay. Colored arrows denote the ZBL, ZPW and Chaco beam paths to the Chama target chamber. The bottom photographs show the inactive Chama chamber at project start on the left. Its current condition is shown on the right: The chamber has been activated for experiments, and all three lasers have been commissioned for Chama.

3.1.1 Chama chamber interior

The Chama chamber interior in its current configuration is shown in Fig. 3.3. Note that the placement and orientation of the x-ray diffraction diagnostic (PACMAN, see Sec. 3.5) has changed considerably during the last three years, reflecting the various changes to the experiment as we developed this capability. The current configuration facilitates experiments that can use ZPW or ZBL to create the x-ray source, a polycapillary lens to enhance the x-ray flux from source to sample, and the Chaco laser to shock-compress a sample inside the PACMAN.

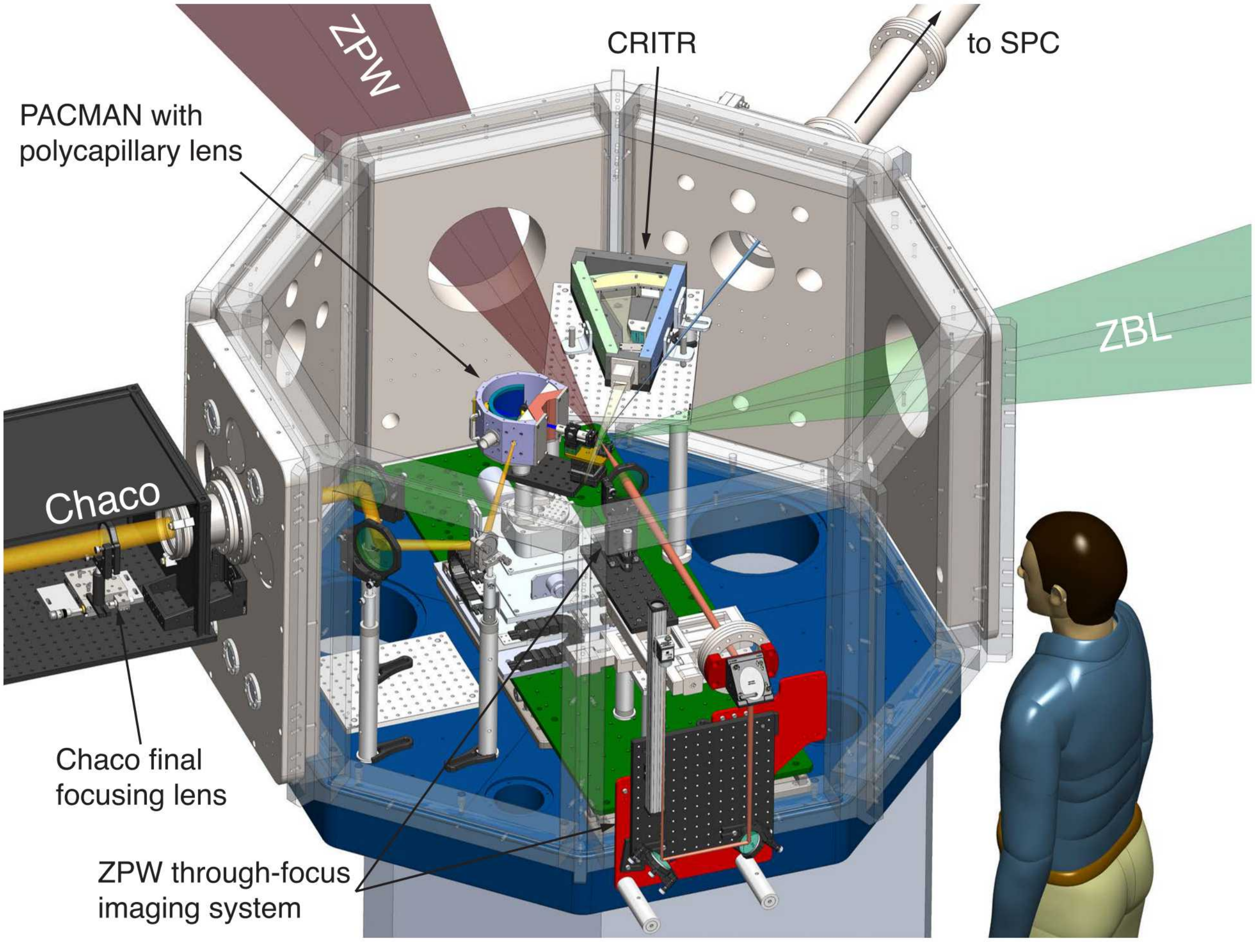

Figure 3.3. Chama chamber interior. This CAD model rendering shows the focusing cones of the ZBL and ZPW lasers, the ZPW through-focus imaging system beam path, the Chaco laser beam path on the left, the orientation of PACMAN, the location of the CRITR spectrometer [31] and the vacuum beam pipes to the single photon counter (SPC). The reference person shown is 185 cm (6′ 1′′) tall.

The focusing beam cones of the ZBL and ZPW lasers enter the chamber through large-diameter holes in dedicated doors. The beams are focused to a target at target chamber center (TCC). A polycapillary lens is used to transport x-rays to a diffraction sample inside the PACMAN enclosure. The Chaco laser enters the chamber from the left. It is focused with a lens outside the chamber and guided to the diffraction sample through a hole in the PACMAN wall with three steering mirrors inside the chamber. A CRITR spectrometer [31] is used to measure the x-ray spectrum emitted by the source. The vacuum beam pipes to the single photon counter (SPC) diagnostic (see Sec. 3.7) are shown on the top right. A lens is placed near TCC to image the ZPW focal spot with high magnification onto a camera placed outside on the chamber door.

Not shown are the ZBL focus alignment camera, which is mounted outside at the door that holds the SPC pipes, and the Chaco alignment camera mounted at the door between Chaco and ZPW. The Chaco camera uses mirrors to observe the sample inside the PACMAN through a hole in the Chaco enclosure. The ZBL and ZPW beams are transported in vacuum; for clarity, the beam pipes and final focusing lenses are not shown.

Fig. 3.4 shows a closeup view of the TCC area inside Chama. The PACMAN enclosure is shown on the left side. Both ZPW and ZBL can be aimed at TCC to irradiate the x-ray source target. The debris shield at the front of the polycapillary lens protects it from shot debris and accidental laser exposure with a 16-μm thick Al foil sandwiched between two layers of 50-μm thick Kapton. The polycapillary lens transports x-rays from the laser target to the diffraction sample inside the PACMAN. Chaco enters the PACMAN through a half-inch diameter hole. Behind the sample the focusing optic of the PDV fiber probe can be seen.

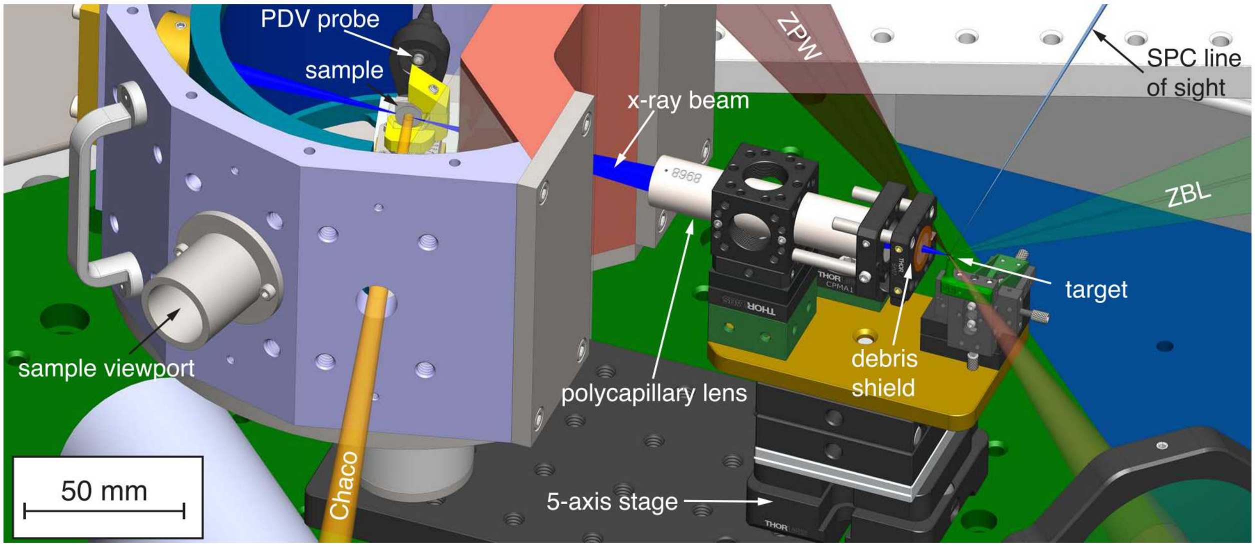

Figure 3.4. Chama chamber TCC closeup view. The rendering shows the polycapillary lens assembly on a 5-axis stage. The target at TCC can be irradiated by either ZPW or ZBL. On the left side is the PACMAN.

3.2 Chaco Vacuum Beam Transport and Final Focusing

Prior to this project, the Chaco laser was delivered only to the Chaco and Pecos target chambers. A sub-aperture beam delivery to Pecos was established using vacuum-ready beam pipes underneath the raised floor. These pipes are shown in green in Fig. 3.5. Before the system could be brought under vacuum, a vacuum pump and pressure gages were installed at position (1) in Fig. 3.5 (bottom left photo) and the system was sealed with blank flanges and laser entrance/exit windows. The pressure safety data package had to be completed as part of this project; the final authorization was obtained on December 1^{st}, 2015.

At full energy, the Chaco laser pulse is about 50 mm in diameter, requiring 4-inch dielectric-coated laser mirrors to guide the beam to Chama. At the end of the Chaco laser table (position (1) in Fig. 3.5) we installed steering mirrors to inject the full-aperture laser beam into the vacuum beam line. At the exit of the vacuum transport section (position (3) in Figure 3.5) the existing beam transport to Pecos was modified by adding a divertor mirror on a kinematic base. The kinematic upper platform now has two options: the first option delivers the Chaco beam to the Pecos target chamber as before; the second option diverts the Chaco beam to the north, where mirrors and beam tubes were inserted on the neighboring optical table for delivery to the Chama target chamber through the southern chamber port. The two options are shown in the bottom right photographs.

The beam path to the Chama chamber was established by adding an extension on the west side of the optical table south of Chama for a steering mirror and a periscope to bring the beam to the same level as the Chama input port. This beam path had to be encapsulated to protect bystanders from stray light during an amplified Chaco laser shot, which was realized using custom-made purple beam tubes as shown in Fig. 3.6a. At the Chama chamber, an 18×24 inch breadboard was installed to hold the final two steering mirrors, the final focusing lens as well as output laser diagnostics such as energy meter and photo diode (Fig. 3.5b).

The final focusing and beam transport was modeled in Zemax OpticStudio (optical design) and Solidworks (distances, location of optics) simultaneously to make sure that distances/angles were correct and mirrors could be installed at Chama at the correct locations, that the beam footprint is not too big on the mirrors to fulfill damage threshold requirements, that no mirror or vacuum window was near a ghost focus, and that the focal spot had the desired diameter of 5 mm. The resulting beam path is shown in Fig. 3.7 on the left side.

The large-diameter focal spot required a large f-number lens (CVI PLCX 76.2-772.6-BK7-532) and placing the target a few mm before or after best focus. The beam had to be routed to the sample inside the PACMAN using steering mirrors past the final focusing lens. The last steering mirror had to placed as far from the focus as feasible to make sure the beam intensity was below the damage threshold of the dielectric coating of the mirror. No commercially available optic could be used for the last mirror, and an in-house-coated 2-inch mirror with very high damage threshold was used [32]. Additionally, the orientation of the sample inside the PACMAN and position of the

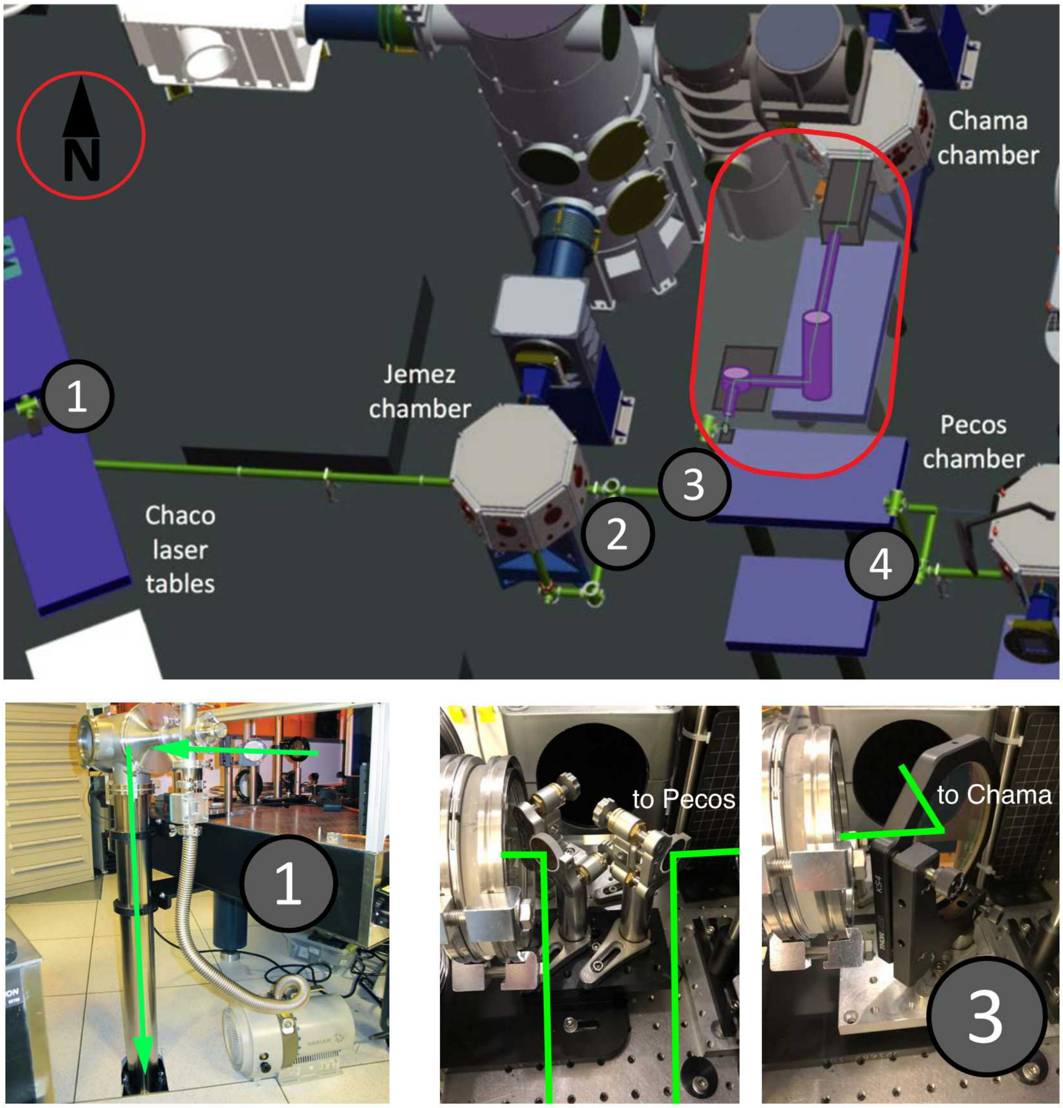

Figure 3.5. Chaco laser relay vacuum system (green tubes). The laser is coupled into the vacuum system at position (1). A periscope guides the laser underneath the raised floor in the Target Bay. Position (2) marks a cross piece, where a relay lens was installed. Position (3) marks the periscope where the beam exits the vacuum system. The vacuum tubes continue underneath the raised floor to position (4), where another periscope is used to couple the laser beam back in and guide it to the Pecos vacuum chamber. Between (3) and (4) the laser beam routing was modified with a periscope and mirrors to guide the beam to the Chama chamber (outlined in red). The lower images show the end of the amplifier table where Chaco is injected into the vacuum relay system (left, 1) and the kinematic mount placed at position (3), with options to deliver the Chaco beam to the Pecos chamber (left) or to the Chama chamber (right).

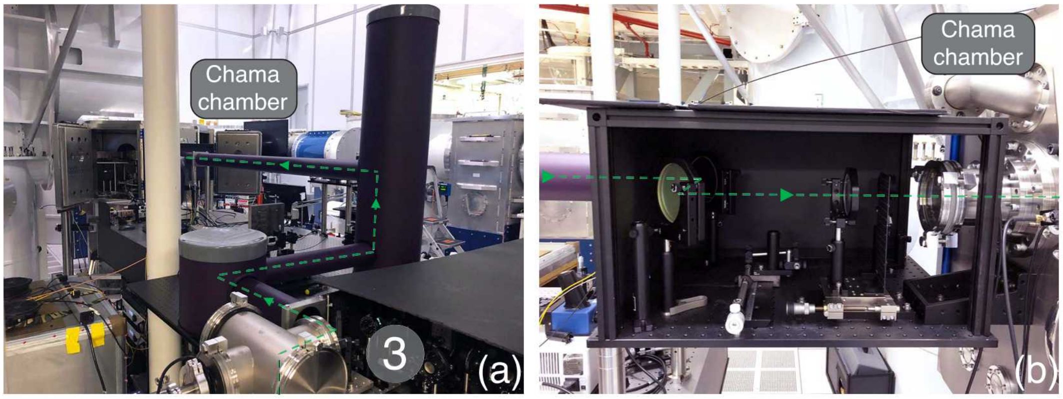

Figure 3.6. Chaco laser beam tubes: (a) Beam delivery system from position (3) of Figure 3.5 to the Chama target chamber, encapsulated in purple beam tubes. (b) The Chaco laser enters the Chama target chamber through its southern entrance port. Final alignment mirrors, focusing lens, and diagnostics are located just before the entrance window.

laser entrance hole prohibited using mirrors at a 45° angle of incidence (AOI). Instead of using an optic with a custom 60° AOI coating, the difference was split among the three mirrors. Reflection measurements confirmed that the AR coating supported high reflection at 40–50° AOI.

The right image in Fig. 3.7 shows a measurement of the focal spot profile using the un-amplified Chaco alignment beam. The beam diameter is 5 mm. The profile is relatively smooth but has a "hole" near the center due to a damaged spot in the 64-mm diameter amplifier rod. All the experiments discussed in this report were performed with this focal spot. For a 15-J beam in 5 ns, the irradiance is about 1.5×10^{10} W/cm^2, which is sufficient to compress samples without generating a hot plasma at the front side [28]. However, it is desirable to achieve a smoother focal spot to reduce hot spots, which create pressure gradients, and to achieve a more one-dimensional shock compression. For this reason we investigated beam smoothing options.

3.2.1 Beam homogenizer design and evaluation

High-fidelity laser compression experiments require a large-area, one-dimensional shock region with no transverse gradients. Hence, we decided to design a random-phase-plate for the $f = 217$ cm lens that could homogeneously illuminate a 5 mm diameter round spot. The phase-plate design was performed via the physical optics and laser analysis software GLAD (General Laser Analysis and Design) from Applied Optics Research (www.aor.com). The modeling code closely follows the "Example #98" in the GLAD examples manual (free download under `http://www.aor.com/anonymous/pub/examples.pdf`) and is based on a technique called simulated annealing, which is also described in great detail in this same example manual.

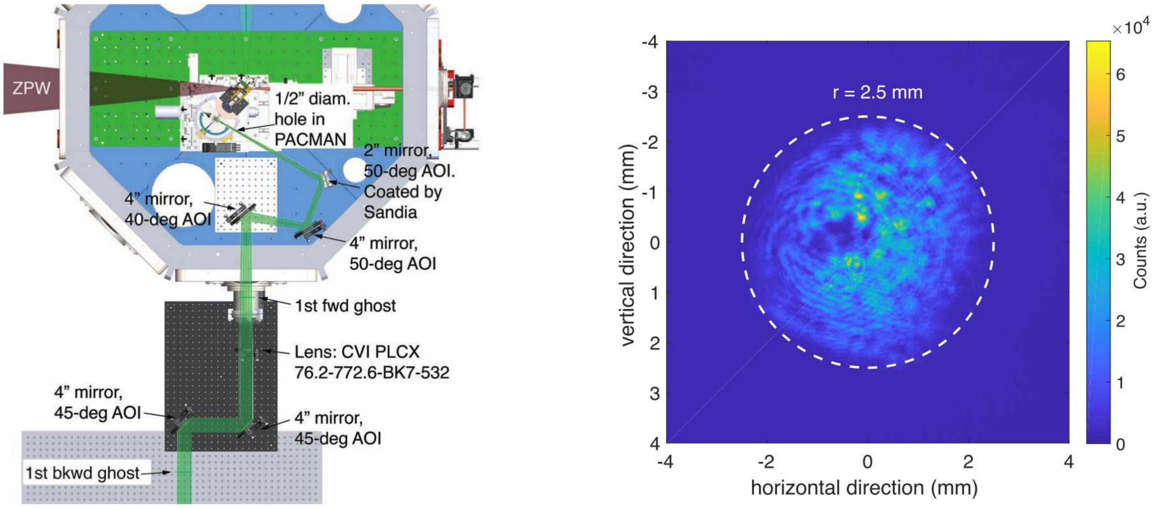

Figure 3.7. Chaco final focusing at Chama. The left image shows the beam path and optics. The right image shows the focal spot, acquired by directly irradiating a Basler aCA2040-25gm CMOS camera. The image was taken 20 mm past the focal spot of an $f = 217$ cm lens to achieve a 5-mm diameter focal spot.

The phase plate design requirements were as follows:

- Phase plate diameter: 6 cm
- Input laser wavelength: 532 nm
- Focal distance: 217 cm
- Target spot size: 5 mm diameter with 8th order super-Gaussian fall-off

These design requirements are quite challenging because they ask for a large focal spot over a short focal distance, i.e., a large focusing angle. Furthermore, the size of the optic is small, which limits the number of random phase elements that can be created. One has to find a balance between the number of phase elements and the homogeneity of the desired target spot. As one may expect, as the number of phase elements goes down, the inhomogeneity of the target spot increases. Fig. 3.8a shows a random phase plate with a spatial frequency of about 1.5/ cm and its associated far field plane (b). As one can see, the speckle pattern is roughly located within a circle of 5 mm diameter but far from a high order super-Gaussian fall-off. In contrast, Fig. 3.8c depicts a random phase pattern with a spatial frequency of 2.5/ cm. One can see that the resulting speckle pattern is more strongly defined, although not quite at the requirements we desire. As the spatial frequency increases, the total optical path difference (OPD) decreases by the ratio of the spatial frequency, i.e., $\frac{15\,\text{waves}}{9\,\text{waves}} = \frac{2.5/\text{cm}}{1.5/\text{cm}}$. This is intuitively clear because the angle has to be the same for all cases. In principle, further increase of the spatial frequency will yield even better results, but the spatial features will be too small to be fabricated. In fact, even the sub-optimal design from Fig. 3.8c was too difficult to manufacture due to the small feature sizes and the large OPDs.

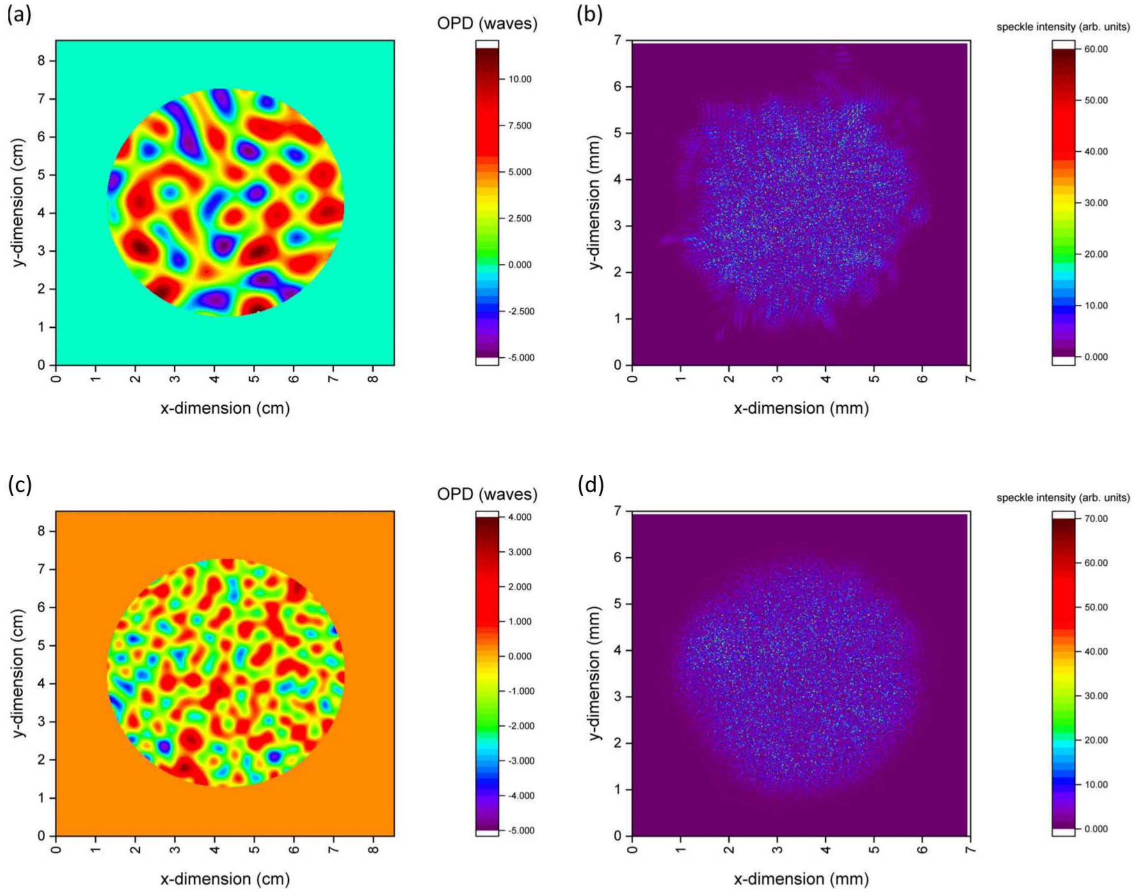

Figure 3.8. Random phase plate designs. a) Calculated phase-plate optical path difference in "waves" for design 1. b) Focal plane speckle pattern resulting from design 1 random phase pattern. c) Calculated phase-plate optical path difference in "waves" for design 2. (d) Focal plane speckle pattern resulting from design 2 random phase pattern.

Since a random phase plate cannot be manufactured for our application, we investigated alternative options for beam smoothing. Diffractive optical elements (DOE's) represent an alternative to phase plates for beam homogenization, which has been well applied in recent years in medium energy lasers (≤20 J) of modest beam size [33, 34]. The French company Silios, appearing to be one of the most prominent vendors, was contracted to provide such a diffractive beam homogenizer. During the design phase, Silios pointed out that a simple homogenizing diffractive optic, when used with a lens to provide a uniformly illuminated disk from the 1st order of diffracted light, will have a central hot spot from the undiffracted (0th order) light at focus. This can be avoided by either causing the 1st order pattern to be angularly separated from the undiffracted light or by adding a diffractive Fresnel lens to the DOE which causes the 1st order pattern to focus at a different position than the undiffracted light. Silios indicated that the former method did not work under our proposed parameter space, so the latter option was taken. When the DOE was delivered and testing began, the uniform flattop spot location also had the central hot spot. As such, the device could not be used to drive uniform shocks. The optic was shipped back to the vendor in Summer 2018, who upon closer examination found a manufacturing error in the optic. The device will be replaced, which may lead to a useful product in future work.

3.3 ZPW Commissioning and Final Focusing

The Chama target chamber is the only location suited for combined ZPW and ZBL experiments. The chamber was physically positioned in its final destination by 2012, but the various elements required to deliver a ZPW beam to this chamber were not fully in place until late 2016 based on budget and programmatic prioritizations. For example, in order to enable optics installation, a catwalk area had to be designed and was finally installed in mid-2016. The ZPW beam path would use a new lens-based focal capability (see Sec. 3.3.1). Once the ZPW path was available, optimization and target shots began in Chama in August, 2017. By early 2018, the additional vacuum path and optics for Z-Beamlet were implemented, allowing delivery of multiple kiloJoules in a few nanoseconds at 527 nm. The photos in Fig. 3.2 show the large-scale changes that occurred to the Chama chamber from the time of initial installation to the present. It is worth clarifying that these large scale facility efforts were funded via programmatic monies rather than those of this project (as evidenced in part by the time frame that long exceeds that of the LDRD) .

3.3.1 Lens-based focusing of sub-nanosecond ZPW pulses

Prior to 1990, many high-energy laser systems used mode-locked oscillators to seed their amplifier chains [35, 36]. The resulting pulses would typically be in the 30–100 ps range at sub-kJ energy levels and were focused by lenses. While these systems performed reasonably, the near field beam quality was marred by non-linear phase effects associated with the B-integral accumulation (see next section) from propagating through the entire laser chain at the same pulse width. As chirped pulse amplification (CPA) short-pulse laser technology rapidly developed to larger and larger beam sizes from the early 1980's, laser scientists began to realize the need to use vacuum beam transport with reflective focusing elements to eliminate deleterious B-integral effects after pulse compression (typically in systems above 10 TW of peak power). Since that time, virtually all CPA lasers have used off-axis parabolic mirrors in vacuum for focusing. If, however, the peak powers are lowered then lens-based focusing could again be considered, with the benefit that the B-integral is reduced from the previous scenario via CPA. Preliminary estimates suggested that a chirped pulse of $\gtrsim$100 ps could be used as long as at least 10^{18} W/cm^2 could still be achieved on target. This loose intensity threshold allows access to the relativistic regime where K_α x-ray generation is still efficient (see Sec.5.2.3), while the shielding from hard bremsstrahlung radiation generated by fast electrons can be manageable (see Sec.5.4). Lens-based focusing has three key strengths over an off-axis parabola:

1. the reduced cost of a lens compared to a parabola,
2. the simplified alignment with a lens (especially when considering aplanatic singlets),
3. the ability to use traditional glass vacuum windows and debris shields.

B-integral

If the decision is made to use a longer laser pulse for the x-ray source, one must weigh the strengths and weaknesses of a refractive lens-based focal technique versus a reflective off-axis parabola focal technique. First, one must actually analyze the B-integral limits to the final optics assembly (FOA) lens versus power. Local and large-scale variations in beam intensity I induce nonlinearities in the refractive index n of a medium (e.g., glass) such that it becomes intensity dependent: $n(I) = n_0 + n_2 I$, where n_0 in the constant refractive index and n_2 is the nonlinear refractive index caused by the Kerr effect. For a given vacuum wavelength λ and propagation distance z, the typical phase $\phi = \frac{2\pi}{\lambda} \cdot nz$ is expanded to examine only the nonlinear phase contribution (called the B-integral) thus:

$$B = \frac{2\pi}{\lambda} \int_0^L n_2 I(z) dz. \tag{3.1}$$

To calculate the B-integral for a system, we evaluate Eq. (3.1) for each optical element of length L and sum the contributions through the laser chain. The "running" total B-integral (called ΣB) contributes to whole beam self-focusing effects, which can be mitigated when kept below a value of 4 radians (per the ZBL design [37]). Note that local intensity fluctuations within the beam can lead to small-scale self-focusing. Since such smaller high spatial frequency features tend to be removed at spatial filter pinholes, one refers to a ΔB that resets to zero at these pinholes. Keeping $\Delta B \leq 2$ radians (per the ZBL design [37]) will then mitigate small-scale self-focusing and its associated damage. An example is shown in Fig. 3.9 for 10 TW (1 kJ/100 ps) of compressed beam for two different chirped pulse widths in the amplifier chain. Note that, even at the modest compression to only 10 TW of peak power, the B-integral climbs rapidly after compression. The model indicates that a slightly longer chirped pulse of 1.5 ns duration (as opposed to the standard gain-narrowed duration of approximately 1 ns) is needed to keep both $\Delta B \leq 2$ and $\Sigma B \leq 4$. Recent efforts with shaped pump pulses in the optical parametric chirped pulse amplifier section of the front-end have demonstrated over 2 ns duration at 77 J on full system laser shots, indicating that the objective is achievable. Note that the lens-based focusing in Chama has lower B-integral values than shown in Fig. 3.9 as there are no vacuum windows or debris shield.

Gain Narrowing

Gain narrowing is the effect whereby the amplified bandwidth in a laser pulse is reduced with increasing amplification due to the spectrally non-uniform gain profile. Typically, due to limitations imposed by the time-bandwidth product, reducing the bandwidth of a laser pulse increases the minimum achievable pulse width. Hence, gain narrowing in a CPA system prevents one from achieving the same minimum pulse width that existed prior to chirping and amplification. Typically for Nd:Phosphate glass, the gain-narrowed bandwidth of 4 nm allows compression to just under 500 fs (without any uncompensated phase). However, in the chirped regime for a pulse centered in the amplifier's spectral gain window, the spectral reduction from gain narrowing simply eliminates wavelengths at the front and rear of the temporal waveform, resulting in pulse shortening. This is why the pulse width reduces from 2.5 ns (or 10 nm of spectrum) at the input to the Nd:Phosphate glass part of the amplifier chain to 1.0 ns (or 4 nm of spectrum) at the output, which is a reduction to 40% of the input duration. If the pulse is only partially compressed (as applied here for lens-based focusing in Chama), gain narrowing will reduce the duration of the partially compressed pulse by the same amount. In our case with partial compression, we measured 180 ps FWHM with a

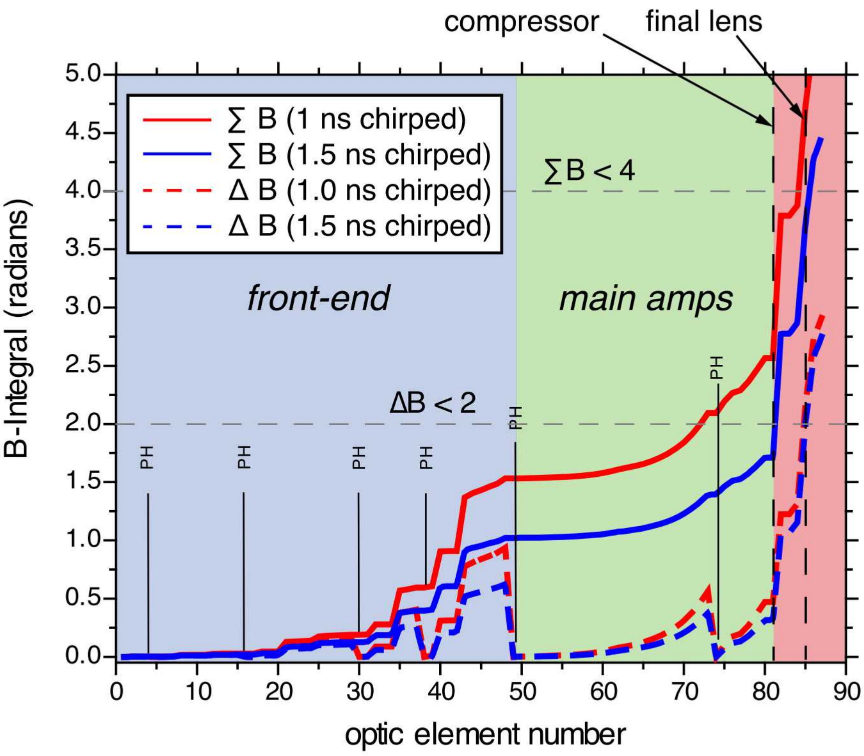

Figure 3.9. B-integral calculation for ZPW assuming lens-based focusing in Z for fixed chirped pulse widths of 1.0 ns and 1.5 ns in the amplifier chain.

streak camera for an unamplified 2.5 ns input into the compressor. Upon amplification, the partially compressed chirped pulse also reduces its duration by 40% to about 72 ps. Standard 250 J ZPW operation showed some variation in the gain narrowed width, with usual results being from 0.8 to 1.1 ns, which corresponds to a range of 58 to 79 ps.

The gain narrowing also comes back into play for lens-based focusing in the impact on chromatic aberration. The assumption at the time of implementation on Chama was that the impact of chromatic aberration on a gain narrowed spectral width of roughly 4 nm would be minimal. However, initial alignments showed the contrary. Chromatic aberration was indeed blurring the focal spot when using the OPCPA seed. An analysis with Zemax OpticStudio was performed on the nominal 2 m focal length lens that was repurposed from ZBL. At its design wavelength of 527 nm over the 39 cm × 39 cm clear aperture of the optic, for a back focal distance (BFD) of 1968.8 mm, the RMS wavefront error is 0.0049 waves and the Strehl ratio is SR = 0.9991. [1] As the Strehl ratio is essentially 1.0, this lens exhibits ideal design performance at 527 nm. However, at 1054 nm over the clear aperture (which is filled by the current beam), the BFD shifts to 2018.422 mm (due to the longitudinal chromatic aberration) in order to get the best Strehl ratio. At that focal length, the Strehl ratio drops to 0.772. Typically, laser users will consider a Strehl ratio of 0.8 to be essentially diffraction-limited, so this performance is acceptable. However, when the wavelength

---

[1] The Strehl ratio is the ratio of measured peak intensity to the ideal diffraction-limited performance [38].

shifts away from 1054 nm, the Strehl ratio quickly drops to zero at both 1050 nm and 1058 nm due to chromatic aberration. The OPCPA seed spans more than 8 nm in a flattop spectrum centered at 1054 nm, meaning the OpticStudio model explains blurring of the focal spot when using the OPCPA seed. The bandwidth at which the Strehl ratio drops below 0.5 is 2.3 nm. This indicates that the best performance region is still not quite the full gain-narrowed amplified spectral width but that the on-shot gain-narrowed focal performance will significantly exceed that of the OPCPA seed alone. To minimize the impact of chromatic aberration on alignment, the continuous wave (CW) alignment beam at 1052.7 nm was used to set the focal spot. Subsequently, the system was switched to the OPCPA seed and the spot quality was checked at the position deemed optimal with the CW alignment beam.

The future full-aperture upgrade to ZPW will increase the beam size in the main amplifiers (to significantly increase the extracted energy) while reducing the beam size within the final target focus lens aperture to about 32 cm × 28 cm. With the same lens, the modeled spectral performance for this beam size at focus shows good improvement for the lens used on Chama (see Tab. 3.1). Regarding a future ZPW focusing on Z, the longer focal length $f = 3.2$ m lens used by ZBL on Z shows even better performance at the 32 cm × 28 cm beam size.

Table 3.1. Beam size and lens type impact on Strehl ratio.

Parameters	Peak Strehl Ratio (SR)	Bandwidth where SR $\geq$ 0.5
39 cm × 39 cm, $f = 2.0$ m	0.772	2.3 nm
32 cm × 28 cm, $f = 2.0$ m	0.831	4.4 nm
32 cm × 28 cm, $f = 3.2$ m	0.997	7.3 nm

3.4 1064-nm Photonic Doppler Velocimetry (PDV) System

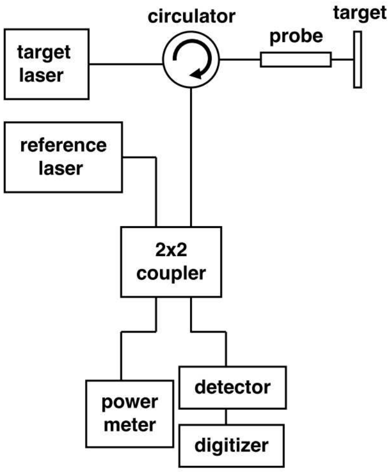

Figure 3.10. Schematic of 1064-nm PDV system.

Photonic Doppler Velocimetry (PDV) is a compact displacement interferometer system using a heterodyne technique to measure the velocity of a moving surface [39]. PDV is essentially fiber-based Michelson interferometry, utilizing advances in near-infrared detector technology and fast digitizers to record beat frequencies in the gigahertz (GHz) range. This method uses single-mode optical fibers and fiber lasers with narrow line widths to produce a usable fringe contrast in the beat signal. Its basic operating principle is briefly described here, see Figs. 3.10 and 3.11.

Typically, PDV systems have used fiber lasers operating at 1550 nm. However, the laser safety eyewear used at the Z-Backlighter Facility does not shield against 1550 nm light. A conversion of the PDV system to a class 1 laser system (for which no laser safety eyewear is needed) was evaluated but did not get approved by management due to remaining safety concerns. A new PDV system operating at 1064 nm—which the ZBL laser eyewear does shield against—was designed and integrated into the facility. The new PDV system consists of two 1064-nm NKT Photonics Koheras AdjustiK Y10 fiber-coupled lasers with up to 100 mW of continuous power, and commercial-off-the-shelf 1064-nm fiber components (e.g., single-mode fibers, circulator, coupler).

The "target" laser is used to illuminate the target's moving surface. Optical fibers are used to transport light from the laser source to a probe containing a lens that focuses the light onto the target surface inside the target chamber. This same probe then collects a fraction of the light that is scattered/reflected from the target surface. As the target moves, the reflected light will be Doppler-shifted. The reflected light is sent via the same fiber through a fiber circulator, and combined with light from the "reference" laser using a fiber 2×2 coupler. The interference between the two optical frequencies creates a beat frequency that is proportional to the target velocity ($f = 2v/\lambda_0$). For example, a target moving at a constant velocity of 1 km/s would produce a measured PDV signal with a beat frequency of 1.88 GHz. This beat signal is measured with a detector (Optilab PR-23-M, 20 GHz) and recorded on a digitizer (Keysight DSA9130A, 13 GHz, 40 GSa/s).

The analysis of the measured PDV signal was performed using the Matlab-based SIRHEN program [40], see Fig. 3.12 for an example. The frequency content of the PDV signal is determined by a short-time Fourier transform (STFT), generating power spectra from signal segments of duration τ. The beat frequency f is determined from the peak location in each spectrum [41]. In the SIRHEN program, a discrete Fourier transform (DFT) analysis is used to transform the input function $s(t)$ (detector signal in the time domain) into an output function $S(f)$ called the frequency domain representation.

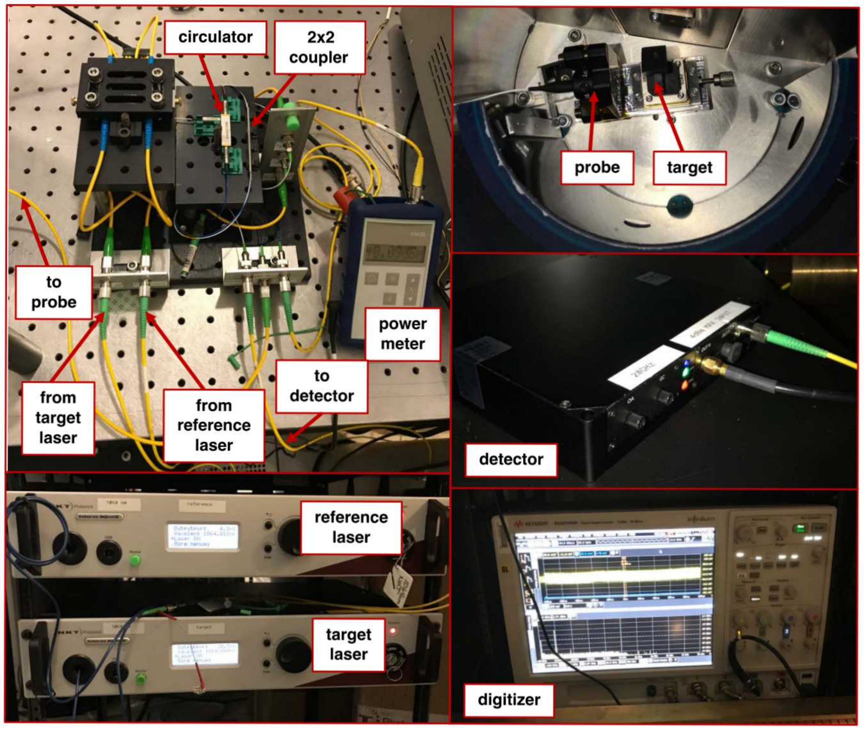

Figure 3.11. Photographs of the 1064-nm PDV system. Clockwise from top left: the PDV instrument, probe and target inside PACMAN, the detector on top of the digitizer, and the two fiber lasers.

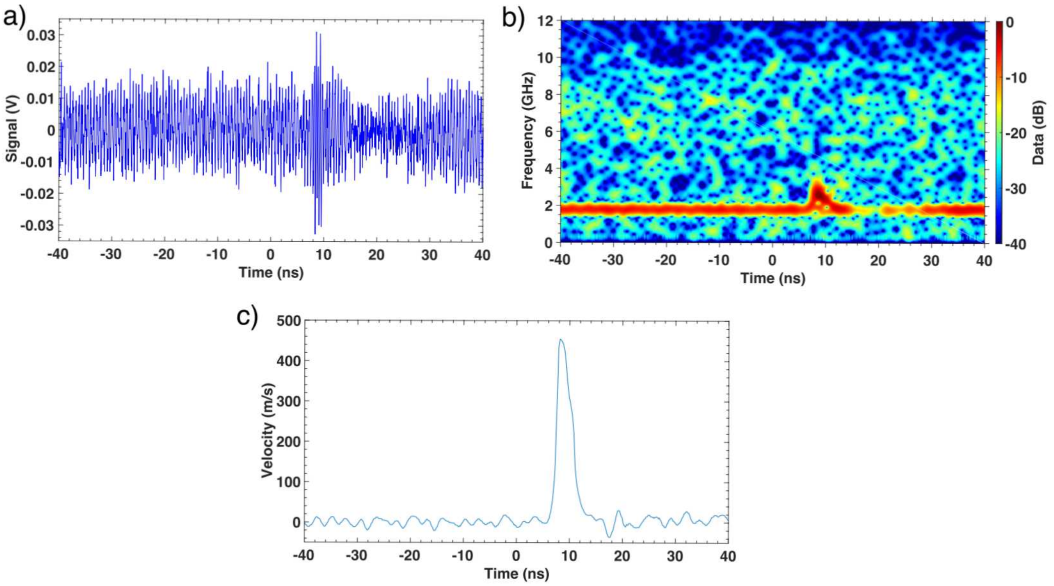

Figure 3.12. PDV analysis using the SIRHEN program: (a) detector signal, (b) beat frequency spectrogram, and (c) target velocity.

3.5 Phase And Crystallographic Measurement ANalysis (PACMAN) Instrument

3.5.1 Initial design

The new PACMAN (Phase And Crystallographic Measurement ANalysis) instrument was designed and fabricated to enable XRD measurements of dynamically compressed samples at Chama. Examination of XRD instruments currently fielded on other laser-driven dynamic compression facilities, such as the Powder X-Ray Diffraction Image Plate (PXRDIP) diagnostic at OMEGA [12] and the Target Diffraction In-Situ (TARDIS) diagnostic at NIF [42, 43], guided its initial design parameters. The PACMAN instrument was designed to meet the following primary requirements:

1. Load geometry analogous to Z-DMP (Dynamic Material Properties) experiments
2. A line-of-sight for the incident x-rays
3. A line-of sight for the drive laser
4. Detection of diffracted x-rays over large range of diffraction angles with sufficient angular resolution
5. Space for a photonic Doppler velocimetry probe
6. Shielding from x-ray background
7. Operational size and weight limitations

1. Load geometry

The goal of this work is to develop an XRD technique transferable to Z-DMP experiments. Z-DMP experiments use thick samples (≈1–2 mm) to produce compressed material states with large uniformity (≈5–10 mm) and long duration (≈50–100 ns), which enable the study of mesoscale (i.e., grain size and orientations) and time-dependent (i.e., phase change kinetics) effects at different strain rates compared to laser experiments. For comparison, laser-driven XRD diagnostics such as the above-mentioned PXRDIP and TARDIS use thin samples (few μm) to produce compressed material states with smaller spatial (lateral) uniformity (≈0.1–0.5 mm) and shorter duration (≈1–10 ns).

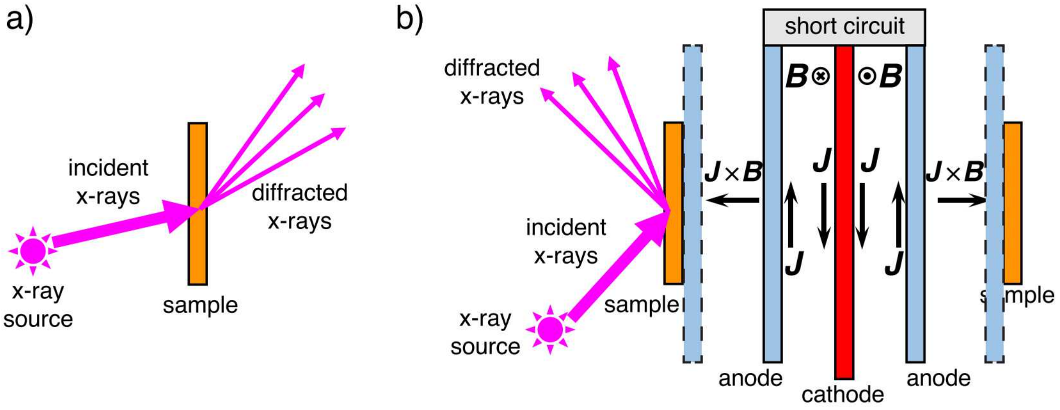

Figure 3.13. X-ray diffraction geometries. a) Transmission geometry. b) Cross-section view of a Z-DMP coaxial load with reflection geometry.

X-ray diffraction on laser-driven experiments typically employs a "transmission geometry" in which both the incident x-ray beam and diffracted x-rays propagate through the sample. The XRD data are detected behind the sample (see Fig. 3.13a). However, this transmission geometry would not be feasible on Z-DMP experiments due to size and geometrical constraints as depicted in Fig. 3.13b. Instead, a "reflection geometry" is employed in which the x-ray beam impinges on the sample at a small angle with respect to the surface (about 10–15°). The diffracted x-rays do not propagate through the entire sample, and XRD data are detected on the same side of the sample where the x-ray beam comes in. Note that the terms 'reflection' and 'transmission' refer to the sample orientation and shockwave propagation direction. In both geometries the XRD diffraction cones being measured are the forward-directed cones, not the backscattered cones.

The Z-DMP coaxial load consists of two anode plates arranged around a central cathode stalk to form two anode-cathode (A-K) vacuum gaps. The short circuit is created between the anode plates and the cathode stalk through a shorting cap at the top of the coaxial load. The current density **J** flowing on the anode and cathode produces a planar magnetic field **B** between them, and the $\mathbf{J} \times \mathbf{B}$ force produces a smooth mechanical stress wave that is proportional to the magnetic field squared. The generated impulsive pressure provides sufficient momentum to launch the anode flyer plates at high velocities across the flyer–sample gap, which then impact and compress the load samples. Such a load has linear dimensions of a few cm in all directions [44]. In a transmission geometry most of the incident x-rays would be absorbed within the sample material's thickness. Any diffracted x-rays that are actually transmitted through the sample would not penetrate the anode plates, cathode stalk, and shorting cap material, and could not be detected. The PACMAN was designed for both reflection and transmission geometry XRD, which consequently determined the orientation of the incident x-rays relative to the load sample as well as the detector geometry.

2. Incident x-rays

Fig. 3.14 shows a schematic of the PACMAN instrument, which is generically represented by the large circle. The sample, image plate detector, and velocimetry probe are located inside the PACMAN. The x-ray source, drive laser, and velocimetry fiber originate from the outside. For reflection geometry XRD, the x-rays are incident to the sample at some modestly shallow angle (≈10–20°) with respect to the sample's surface. On reaching the sample, the x-rays may interact with the sample's material in a variety of ways. Some of the x-rays will be absorbed and some will be scattered. If neither process occurs, the x-rays will be transmitted straight through the material.

For the specific case of elastic scattering from a crystalline material, the x-rays undergo constructive interference and produce diffracted x-rays that satisfy Bragg's Law [45]:

$$E = \frac{mhc}{2d\ \sin\vartheta}$$

where E is the x-ray energy, m is an integer denoting the reflection order, hc is the Planck constant times the speed of light, d the lattice spacing between crystal planes, and ϑ the grazing angle (Bragg angle).

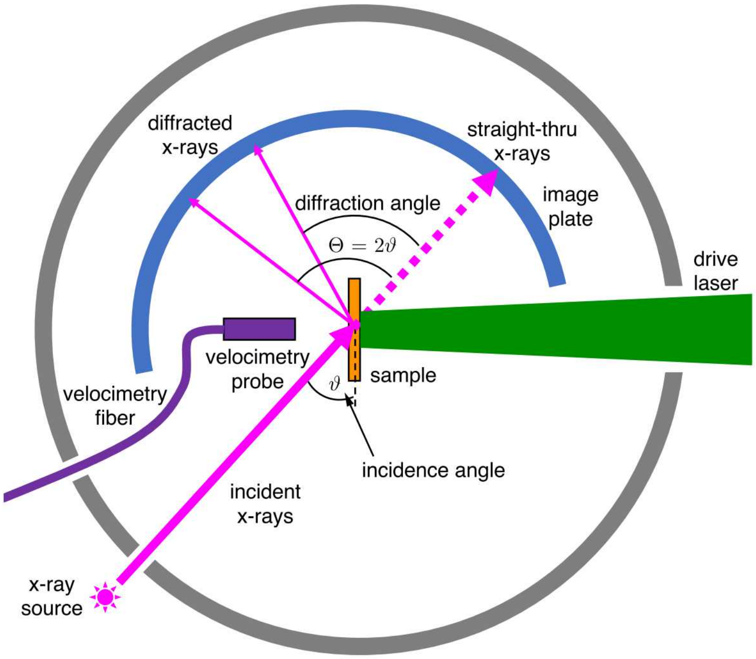

Figure 3.14. Schematic of the PACMAN instrument (top view).

Relative to the straight-through x-rays, the diffracted x-rays would have a measured diffraction angle of

$$\Theta = 2\vartheta.$$

Depending on the diffraction angles of interest, the proper angle between the incident x-rays and sample surface require some rotational adjustment of the sample. For example, to measure diffraction angles as small as 30°, the x-ray incident angle needs to be less than 15°. Note that for an x-ray beam with a circular spot with 1 mm diameter, at the sample surface it would be an ellipse with one axis elongated to a length of 3.9 mm.

3. Drive laser

To perform dynamic compression, a laser is used to drive a pressure wave into the sample that mimics the load geometry of the Z-DMP experiment. The drive laser beam is directed into the PACMAN through a small aperture in its side wall, and focused onto the sample surface opposite of the incident x-rays. Typical samples are 8–13 mm in diameter, so the focused laser spot size is about 4–6 mm in diameter to obtain adequate lateral drive uniformity.

4. Range of diffraction angles and angular resolution

The diffracted x-rays are detected by an image plate (IP) that is cylindrically curved around the sample. This enables the simultaneous measurement of both the diffracted x-rays over a large range of diffraction angles and the straight-through x-rays on a single, long IP. For a cylindrical IP with a fixed radius of r, the measured angle of a given diffracted x-ray is

$$\Theta = \frac{s}{r},$$

where s is the arc length at that given position.

Although the IP may be scanned with a pixel resolution as small as 25 µm, the effective spatial resolution is between 60–90 µm [46, 47]. Using a conservative spatial resolution of 100 µm and a radius of 60 mm, an angular resolution of 1.7 mrad or 0.1° could be achieved. Increasing the IP's radius would improve the angular resolution, but consequently reduce the signal intensity and therefore signal-to-noise ratio (SNR). For comparison, the PXRDIP diagnostic at Omega provides an angular resolution of $\approx 0.8°$ [12], the TARDIS linewidths are typically $\approx 1°$ [48].

The expected diffraction patterns span a large angular range (see Sec. 4.1). The forward-diffracted cones span the range of $\Theta_{\max} \approx \pm 90°$. The PACMAN is designed to work both in transmission and reflection geometry, therefore we require a measurement range of $\Theta \approx [-55°, +100°]$ to capture as many diffraction rings as possible for any given x-ray energy/sample combination while leaving room for the Chaco laser pulse. Taking the resolution requirement into account, the cylindrical detector needs to span an arc length of more than 6 inches. The detector height had to be similar to the radius in order to capture enough of a ring section to determine its curvature, which is important for data analysis. These requirements determined the overall size of the PACMAN diagnostic: it should be cylindrical with an inner radius of 80 mm and a clearance height of 75 mm (3 inches).

For each XRD experiment, the same IP position relative to the sample is maintained with reasonable reproducibility by holding the IP in a rigid, curved frame that is mounted to the base of the PACMAN. This rigid, curved frame for the IP was fabricated with 3d-printing, allowing us to quickly test and iterate on different prototypes (mainly different radii and filter mounting options) until a suitable design was determined.

5. Velocimetry probe

Optical light from the 1064-nm photonic Doppler velocimetry (PDV) system described in Sec. 3.4 is transmitted through fiber into the PACMAN through a small opening. The fiber-coupled PDV probe is positioned facing the sample surface opposite the drive laser. To optimize the light return from the sample surface, the PDV probe is fine-tuned with longitudinal translation and tilt-tip adjustments.

6. X-ray background shielding

Because XRD is a scattering-type measurement it has inherently low signal levels. Thus, achieving sufficient SNR is an essential requirement. X-ray background from the x-ray source, especially when generated by the ZPW short-pulse laser, would overwhelm the XRD signal without appropriate shielding. Accordingly, the PACMAN housing needs to be fabricated of materials with sufficient x-ray attenuation properties (e.g. tungsten), specifically near the x-ray source. A rule-of-thumb for Z diagnostics inside the center vacuum chamber, which face similarly strong background radiation, is to encapsulate the detector in a 1-inch thick tungsten housing. Earlier x-ray imaging experiments at the 100 TW target chamber [49] also required a thick detector enclosure. The laser target-facing side of PACMAN should be equipped with a high-atomic-number shield such as tungsten of at least 1-inch thickness.

7. Operational size and weight limitations

The entire PACMAN housing could not be fabricated from tungsten because of operational size and weight limitations. Specifically, to enable positioning within the Chama chamber, the PACMAN was planned to be mounted on a 4-axis (x, y, z, ϕ) stage, which has a load rating of 40 lbs (18 kg). In addition, the PACMAN needs to be lifted and moved in and out of the Chama chamber by hand without any hoisting apparatus. Since the PACMAN is large (see #4), the main shield at the front side was made of a tungsten alloy and the side walls were made of stainless steel. The side walls are 3/8-in. (9.5 mm) thick. The front faceplate is 1 inch. To avoid long lead time issues for pure tungsten and to keep costs reasonable, various materials and compounds (e.g., Ta, WCu, W, stainless steel) were evaluated for their x-ray shielding properties using tabulated x-ray attenuation values [50]. We decided on an alloy of tungsten (70%) and copper (30%), which is also better to machine and less brittle than pure tungsten. This faceplate is perpendicular to the x-ray source and has a tapered aperture that defines an entrance path for the incident x-rays to the sample.

3.5.2 Mechanical design

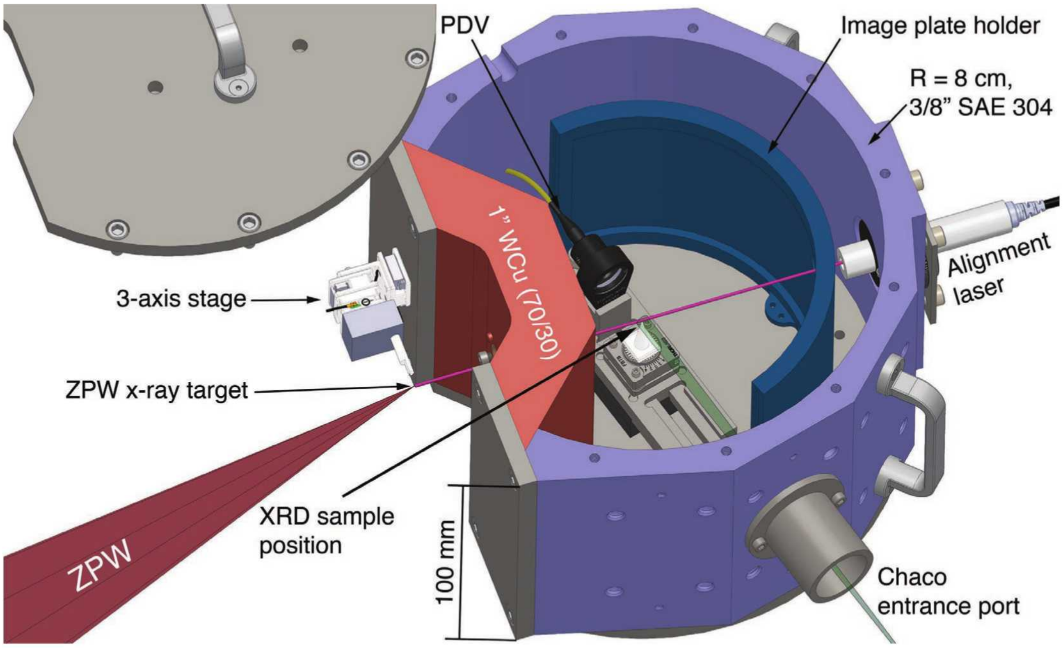

Figure 3.15. First version of the PACMAN diagnostic. At the center of the PACMAN cylinder is the diffraction sample (shown here is an alignment cone). ZPW irradiates an x-ray target outside of PACMAN (left side), the Chaco laser enters through an entrance port. The PDV probe observes the target rear side to infer the sample pressure. Diffracted x-rays are detected by an image plate (IP) detector with 60 mm radius. An alignment laser can be installed at the back side. Not shown is the light filter foil in front of the IP holder.

The first version of the PACMAN diagnostic is shown in Fig. 3.15. In this version, the target was glued to a stalk and held by an ultra-small, 3-axis piezo stage (Mechonics MS15) in front of the PACMAN. The U-shaped WCu front shield assures that there is at least 1 inch of WCu between the target and the detector. A 0.05-in. (1.27 mm) WCu (70/30) pinhole can be installed on either the inside or outside of the 1-inch WCu plate. The stainless steel (SAE 304) housing is up/down symmetric, 100 mm tall, and the inner radius is 80 mm. The outside is faceted into nine straight sections; each section has four 1/4-20 tapped holes to mount additional equipment in the future. The side opposite of the ZPW laser target has a 1-in. diameter hole for an alignment laser (Thorlabs CPS635R) in a tip/tilt mount (Thorlabs KAD11F). The XRD sample surface is nominally oriented at 15° with respect to the alignment laser axis. A facet of the housing has a 20-mm diameter laser entrance port for the Chaco laser. This entrance port is equipped with a collimator, which protects the inside of PACMAN from scattered ZPW laser light and background radiation. The facet on the opposite side has a small cutout on the top and bottom to route the PDV fiber. The 7×3 in. image plate detector is held by a 3d-printed holder with 60 mm radius ($\Theta = [-80^\circ, +70^\circ]$, negative angles are on the PDV side, positive angles on the Chaco side).

3.5.3 PACMAN enhancements

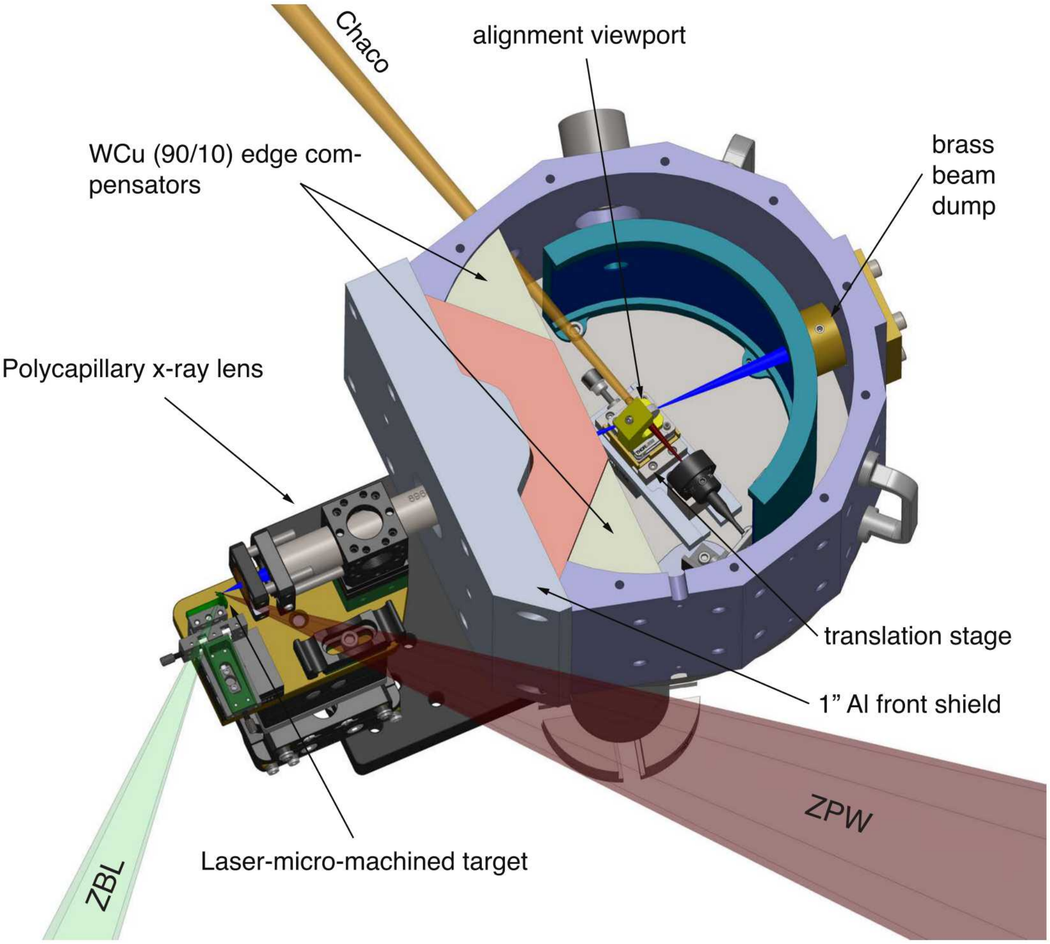

Figure 3.16. Current version of PACMAN, see text for details.

The PACMAN, shown in Fig. 3.15, was designed and fabricated to meet the specifications described in the previous sections. However, some enhancements to this initial design were included over time to improve the diagnostic. The following paragraphs provide details about the problems that were encountered, and the solutions that were developed, which lead to the final setup of the PACMAN shown in Fig. 3.16.

X-ray polycapillary lens
In addition to the shielding efforts, an x-ray polycapillary lens was included to increase the x-ray yield reaching the sample. The final mounting solution is shown in Fig. 3.16. The next section describes polycapillary lenses and their integration into PACMAN in much more detail.

Additional shielding
The original PACMAN design in ZPW experiments was susceptible to high background levels that

were not well understood, and therefore the original shielding proved to be insufficient. Additional shielding was added in various places:

- Two wedges (90% tungsten/10% copper) were fabricated to fill empty space within the PACMAN as an extension of the faceplate.
- A plastic-lined brass x-ray beam dump was added to the back side.
- A 1-in. Al front shield was made to decelerate fast electrons escaping the target before they hit the WCu shield to reduce bremsstrahlung.
- Additional 1/4-in. (6.35 mm) thick plates of brass, aluminum and polyethylene were added to the front to reduce hot electron and bremsstrahlung background (not shown).
- The inside of PACMAN was lined with 1-mm polypropylene to mitigate internal fluorescence (not shown).
- Enclosures (one 90% tungsten/10% copper, one ABS plastic) were fabricated to envelop the x-ray target (not shown).

The enclosure and additional shielding plates were tools used in a few ZPW experiments to isolate the x-ray source in the target chamber. See Sec. 5.4 for a description of these experiments as well as modeling results.

Linear motion

Fig. 3.17 shows a detailed view of the sample holder in its current version. Starting at the top left side the image shows the PDV probe, which is used to measure the sample pressure. Since this diagnostic is sensitive to the relative alignment between the fiber probe exit and the sample surface, both the sample and PDV focusing lens are mounted on rigid platform. The sample (a thin foil) is glued onto the surface of a 12.5-mm diameter, 1064 nm AR-coated, $\lambda/4$ N-BK7 laser window (Edmund Optics #49-148) to guarantee flatness. The glass disk is mounted in a custom, 3d-printed sample holder. This sample holder sits on top of a tip/tilt/rotation stage (Thorlabs FBTB), which is used to adjust the sample orientation such that the PDV probe signal is maximized. A linear translation stage ($x = \pm 2.5$ mm) had to be installed to allow precise positioning of the sample surface to the x-ray beam axis. No commercially available products could fulfill the tight space requirements, hence a custom stage was designed. On the bottom of the platform is a 1×1-in. kinematic base for a repeatable installation. Prior to a shot the entire stage can be removed outside of PACMAN to accurately position the sample in its holder and to align the sample to the PDV beam.

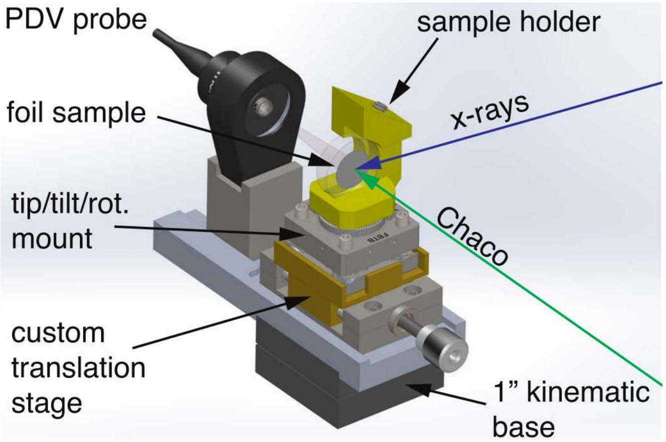

Figure 3.17. XRD sample holder in PACMAN.

Chaco laser entrance hole and diagnostic viewing hole

The Chaco laser entrance hole in the initial design (Fig. 3.15) was designed for the PACMAN centered at the Chama target chamber, where Chaco had a "straight shot" from the focusing lens outside of Chama into the PACMAN and ZPW would irradiate the x-ray source target right in front of the WCu shield. This plan had to be changed once we discovered that we needed to use polycapillary lenses to increase the distance and shielding between source and PACMAN. In its current configuration, see Fig. 3.7, the PACMAN is mounted at 45° with respect to the Chaco laser entrance beam axis. Compared to the initial design, Chaco now enters from the opposite side, and therefore a 10-mm diameter hole and to be drilled into a side. The former Chaco laser entrance hole is now being used as view hole for the Chaco alignment camera, which allows precise beam pointing and focal spot size alignment while the chamber is under vacuum. In the initial design we had set up a retro-imaging telescope behind one of the Chaco steering mirrors further upstream. The new design is much easier to keep aligned and the field of view of the camera is much larger than before.

Image plate alignment fiducial

The foil samples we used did not generate perfectly smooth diffraction rings, but highly structured rings due to preferred orientation in the foil. This, in combination with the subtle changes observed in the first DXRD experiments (Sec. 5.6), required a very precise determination of the location of the undiffracted x-ray beam to find the origin of the diffraction rings ($\Theta = 0$). Even though we placed additional attenuators in front of the IP at the location of the undiffracted x-ray beam, the signal was still overexposed in some shots or somewhat irregular, which added errors to the analysis. In its current configuration, the IP area near the PDV probe does not detect diffracted x-rays because it is behind the glass disk. The background in this area is high enough to place a permanent alignment fiducial in front of the IP that casts an x-ray shadow that is visible when the IP is being scanned. A 1.5 mm thick Al plate with three 2-mm diameter holes and an adapter plate for PACMAN were machined in-house (Othermill Pro) and installed in the PACMAN. This occurred in the late August 2018 and only a few laser shots could be taken before this project ended. The first results look promising, and future experiments will determine if this fiducial helps reduce measurement uncertainties.

3.6 Polycapillary X-ray Lenses

An x-ray optic can be used to collect and re-focus x-rays from the source to the sample, while the source–sample distance is increased compared to a pinhole. The most efficient optic for this purpose is an x-ray polycapillary lens [51]. X-ray polycapillary lenses consist of a bent array of 5–10 μm diameter hollow glass fibers in a hexagonal configuration [52–55]. These lenses differ from single-bore capillaries and x-ray mirrors in that the focusing or collecting effects come from the overlap of the beams from thousands of channels, rather than from a few surfaces. Generally, this results in relatively efficient collection, especially from highly divergent sources such as the laser-plasma sources generated here. Interestingly, polycapillary lenses to enhance the x-ray flux for laser-plasma x-ray sources had already been mentioned in one of the first publications presenting polycapillary lenses [52]. While x-ray polycapillary lenses have demonstrated their usefulness in high-repetition-rate, fs laser experiments (e.g. [51, 56–58]), they are not yet in broader use in single-shot experiments. A recent publication by Maddox *et al.* [4] showed that polycapillaries can be used to enable XRD with a rod pinch pulsed power diode in an experiment that required a large standoff. A polycapillary lens was also used in a recent static short-pulse laser XRD experiment at the Vulcan laser facility [59].

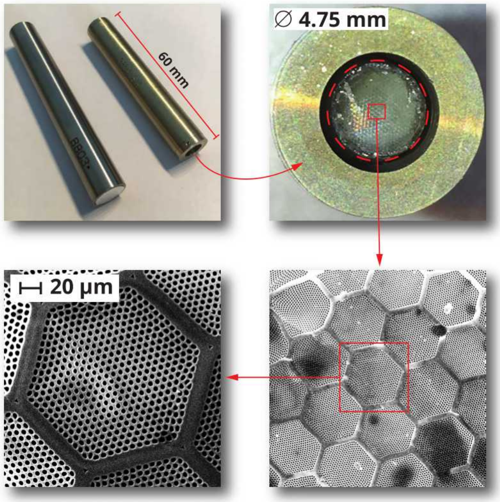

Figure 3.18. Photos and microscope images of an x-ray polycapillary lens.

Fig. 3.18 shows clockwise starting from the top left: a photograph of two of the four purchased lenses inside their cylindrical housings; the input side with the polycapillary bundle; a microscope image showing a subsection of the array revealing a capillary arrangement in hexagonal sub-bundles; and finally an electron microscope image showing the individual hollow channels. X-rays propagate in these curved and tapered hollow tubes by multiple reflections in a manner analogous to the way fiber optics guide light, which is visualized by the cartoon in Fig. 3.19. The images in the bottom row of Fig. 3.19 show measured x-ray beam profiles vs. distance for 6.4 keV x-rays (Fe K_α). An image plate (Fuji BAS-TR, scanned with 25 μm pixel size on a Fuji FLA-7000 scanner) was used as the detector. Directly at the output of the lens, the beam profile is hexagonal. A close inspection of the image reveals the individual hexagonal sub-bundles. At the focus, the Gaussian spot is <500 μm FWHM.

3.6.1 Key performance parameters

Since this type of x-ray optic is still not well known in our field, the following paragraphs describe x-ray polycapillaries in detail. Laser-driven diffraction is an inherently photon-starved experiment, therefore we focus on calculating the throughput vs. x-ray energy for a given lens.

The x-rays are guided inside the hollow capillaries by the process of total external reflection (TER) at the boundary between vacuum and the inside glass surface. Total external reflection occurs because the x-ray index of refraction of glass is smaller than 1. X-rays are reflected whenthe incidence angle with respect to the surface is below the critical angle θ_c for TER. For borosilicate glass,

$$\theta_\mathrm{c} \approx 30\,\mathrm{keV}/E\ [\mathrm{mrad}],$$

where E is the x-ray energy in keV [54, 55]. Key to an efficient reflection and x-ray transport of the lens is the small capillary size. Most of the x-rays are entering a capillary at a shallow angle much less than θ_c and will therefore be totally reflected.

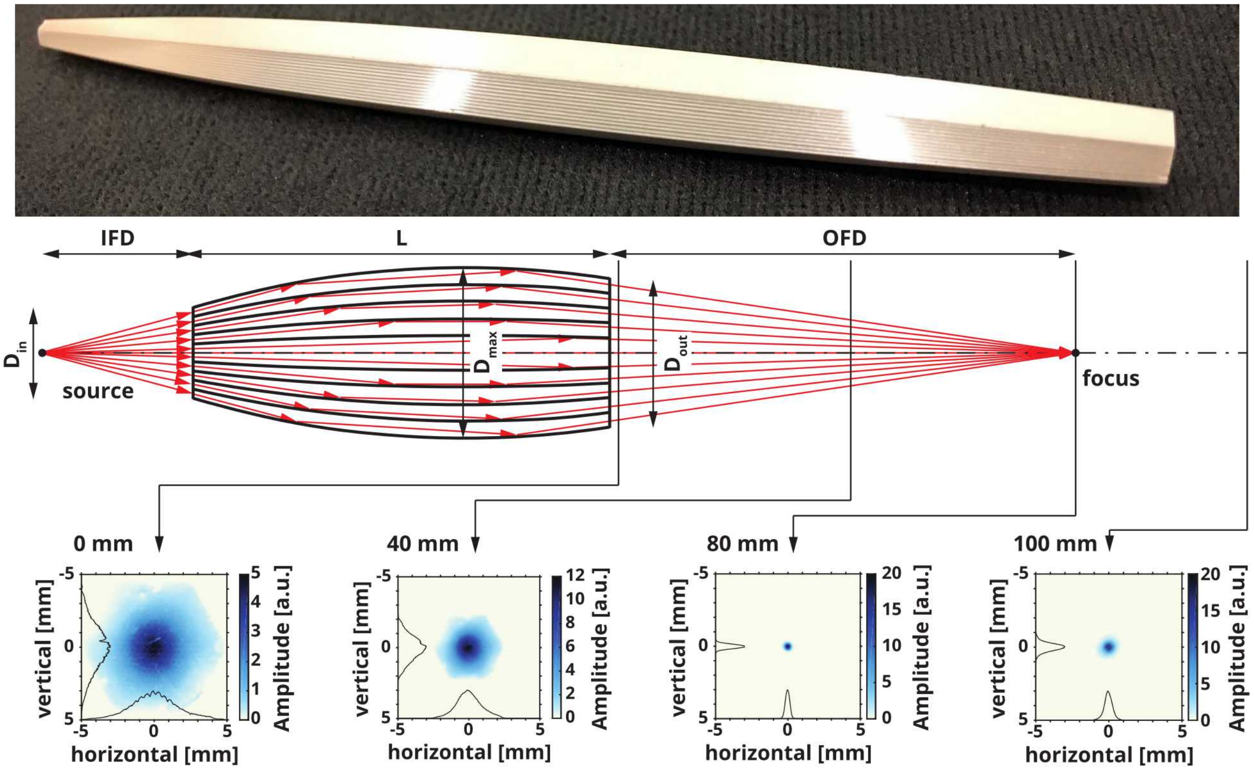

Figure 3.19. Polycapillary lens geometry. The upper images show a photo of a polycapillary lens and a cartoon visualizing the geometry. The images in the bottom row show measured x-ray beam profiles for XOS #8968. The dimensions are listed in Tab. 3.2.

3.6.1.1 Technical data

During this project, six polycapillaries were purchased and tested for their suitability to enhance the x-ray flux emitted from the laser-plasma source and to increase the standoff between source and diffraction sample to lower the background. Two lenses were designed by IfG Adlershof[2] and four designed by XOS.[3]. The technical data are listed in Tab. 3.2.

The initial XRD tests were performed with IfG #246mls19 and XOS #8803. The lens by IfG, due to its longer input focal distance (IFD) compared to the XOS model, was easier to align but had about 4× less throughput. After the initial tests we asked the vendors to design new lenses that had higher throughput. These are the models IfG #239mls07 and XOS #8968. The XOS lens, due to its much larger diameter, has superior throughput compared to the IfG model and therefore the final experiments were performed with this lens. However, even with this lens the background encountered in ZPW experiments (see Sec. 5.4) was still too high for XRD experiments

---

[2] now Helmut Fischer GmbH, Institut für Elektronik und Messtechnik, Rudower Chaussee 29/31, 12489 Berlin, Germany

[3] 15 Tech Valley Drive, East Greenbush, NY 12061, USA

Table 3.2. Polycapillary lens technical data. For each lens the table shows the serial number, input focal distance (IFD), optic enclosure length (L), output focal distance (OFD), total system length, input diameter (D_{in}), output diameter (D_{out}), maximum diameter (D_{max}), input solid angle (Ω_{in}), measured (by the vendor) focal spot FWHM at 17.4 keV (Mo K_α). The single-capillary diameter and capillary-to-capillary spacing for IfG #246mls19 were taken from the bottom-left image of Fig. 3.18. The number of capillaries is numerically calculated under the assumption of hexagonal packing (see Eq. (3.7)).

	IfG	**IfG**	**XOS**	**XOS**	**XOS**	**XOS**
Serial number	246mls19	239mls07	8803	8968	9312	9311
IFD [mm]	31.3	31	26	24.8	26	26
L [mm]	57.3	78.2	69	69	72	72
OFD [mm]	105	109.3	80	80	404	1104
System length [mm]	185	210	174	173.8	502	1202
D_{in} [mm]	4.75	4.4	4.5	5.8	5.8	5.8
D_{out} [mm]	6.8	6.9	-	-	-	-
D_{max} [mm]	7.25	7.35	6.4	10	10	10
Fill factor ζ (%)	20	20	$\approx$ 20	-	-	-
Ω_{in} [mrad]	15	13	19.5	38	34.6	34.6
17.4 keV focus [µm]	235	245	< 250	197	570	1200
Cap. radius R [µm]	4	-	-	-	-	-
Cap. spacing s [µm]	4.5	-	-	-	-	-
No. of capillaries N	$\approx$57k	$\approx$ 50k	$\approx$ 52k	$\approx$ 90k	$\approx$ 90k	$\approx$ 90k

with x-ray energies above 8 keV. A promising background mitigation strategy is to further increase the distance between laser target and PACMAN. XOS designed two large-diameter lenses with a much-increased system length to accomplish this. XOS lens #9312 will allow us to put PACMAN right at the Chama chamber vacuum door for maximum distance inside the chamber. XOS lens #9311 enables us to move the PACMAN outside of the chamber to use the 4-in. stainless steel door as an additional shield. The lenses have been tested in our alignment chamber and we confirmed their functionality. The implementation of these lenses requires a major redesign of the experiment, which is planned to start after this project has ended.

3.6.1.2 Critical angle and field of view

The critical angle can be calculated using Snell's law and tabulated index of refraction (n) data from [60]. For example, the refractive index for BK7 glass (85 % SiO_2, 15 % B_2O_3, $\rho = 2.23\ \mathrm{g/cm^3}$) for Cu K_α at 8.048 keV is $n = 0.999992807$. A numerical fit to the tabulated data for x-ray energies above 1 keV reveals only a small correction to the approximation discussed above:

$$\theta_{\mathrm{crit}} = 30.36/E\ [\mathrm{mrad}]. \tag{3.2}$$

Fig. 3.20 shows a plot of Eq. (3.2). The discrete data points were calculated in non-sequential ray-tracing runs with Zemax OpticStudio using the tabulated n from above. Given the fixed IFD, a

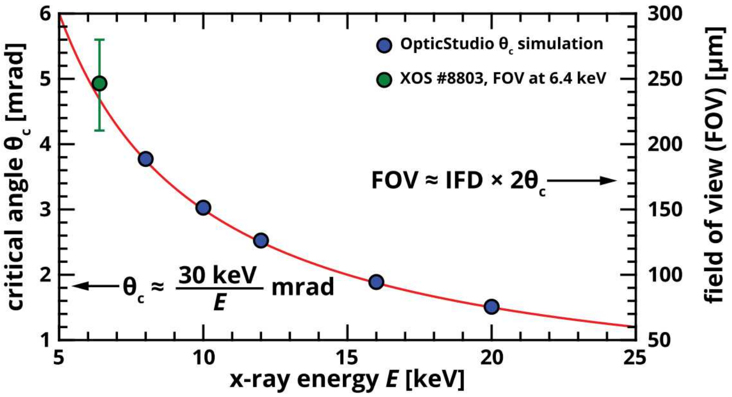

Figure 3.20. Polycapillary critical angle and field of view (FOV) vs. x-ray energy. The red line is a plot of Eq. (3.2), the blue data points are from a Zemax OpticStudio simulation. The critical angle determines the input field of view of the polycapillary lens (Eq. 3.2). The right vertical axis shows the FOV calculated for an IFD of 25 mm. The green data point represents the measurement in Fig. 3.21.

major consequence of the small critical angle is that the capillaries can only reflect x-rays from a small source area. This can be expressed by the input field of view [54, eq. 5]

$$\mathrm{FOV} = \mathrm{IFD} \times 2\,\theta_\mathrm{c}, \tag{3.3}$$

which is shown on the right vertical axis of Fig. 3.20. The FOV was calculated for an IFD of 25 mm (XOS lenses). For an isotropic source, the FOV describes the source size “seen” by the polycapillary lens. X-rays emitted from within the FOV can be reflected and transported, x-rays emitted from outside the FOV will be rejected. Since the critical angle is energy-dependent, so is the FOV. For example, the lens will collect 5 keV x-rays from a source with 300 μm diameter, but 20 keV x-rays will only be collected from a 75-μm diameter source.

The green data point in Fig. 3.20 is a measurement of the FOV for XOS #8803 using 6.4 keV Fe K_α x-rays. The FOV was determined by measuring the x-ray flux vs. source position for a 100-μm stainless steel x-ray source while keeping the lens static. An x-ray CCD camera was used to observe the x-ray beam behind the polycapillary. Details about this procedure will be given in Sec. 3.6.2. The x-ray source was translated step-wise in longitudinal (x: focus) or transverse (y: left/right, z: up/down) direction and the relative x-ray flux was measured by integrating the CCD image.

Fig. 3.21a shows the results for XOS #8803. The lens is clearly much more sensitive to a transverse offset of the x-ray source than to an axial offset. The data were fitted with Gaussians to determine their FWHM. The difference between the L/R and U/D data is probably caused by the experimental geometry such as errors in the x, y, z stage translation and calibration, source orientation, etc. The measured width of the distribution had to be corrected for the source size. This was done using forward-convolution and least-squares fitting of a 100-μm tophat function, representing the source distribution, and a Gaussian, representing the polycapillary FOV, to the

Gaussian fitted to the data. The mean value of the L/R and U/D data is plotted by the green circle in Fig. 3.20, the error bars are the min/max difference between the mean value and the two measured widths. This data point agrees very well with the calculated FOV and critical angle curve.

A similar measurement was made using IfG #246mls19, see Fig. 3.21b. For this lens the FOV and critical angle were significantly larger, about 430 μm and 6.8 mrad. Furthermore the focus measurement (blue data points) of this lens resulted in a skewed Gaussian fit, indicating that the measurement was out of focus. The measured L/R, U/D widths and θ_{crit} from Eq. (3.2) suggest an IFD of 43 mm, which is much larger than the 31.3 mm specified by the vendor. Another possible explanation for the discrepancy is that Eq. (3.3) needs to be modified because it describes the FOV for a single capillary and not necessarily a large array of thousands of capillaries. It is conceivable that for example the actual polycapillary lens input diameter, capillary curvature or single polycapillary diameter need to be included. A polycapillary ray-tracing code is under development to look into this.

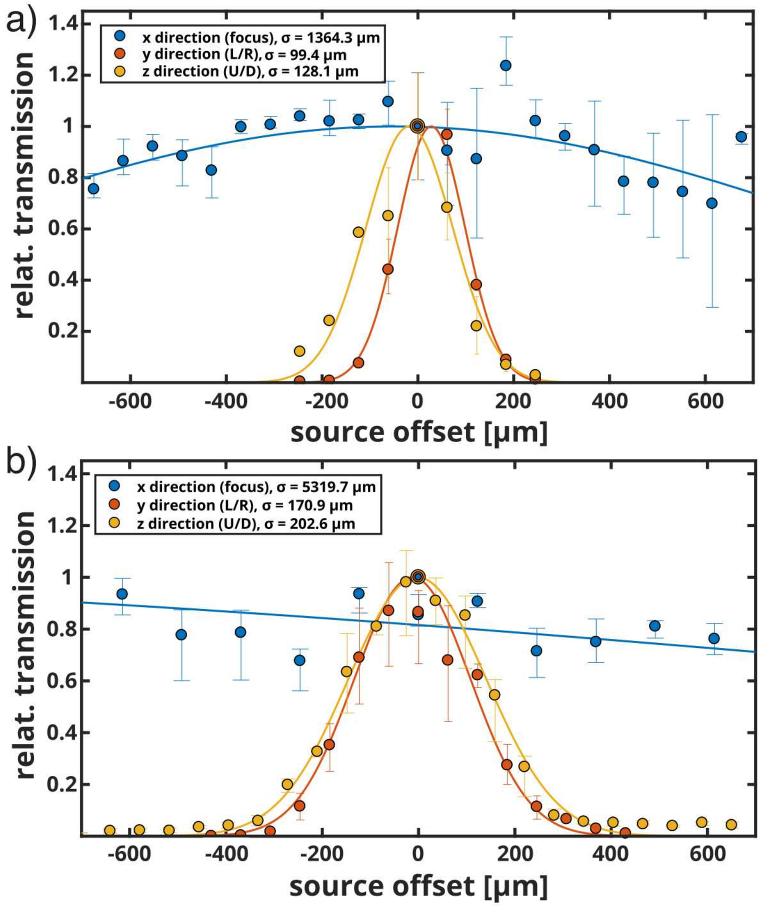

Figure 3.21. Alignment sensitivity measurement for two polycapillary lenses. a) Shows data for XOS #8803, b) Shows data for IfG #246mls19. The data were fitted with Gaussians to determine the width (lines) as shown in the figure legends.

3.6.1.3 Transmission and fill ratio

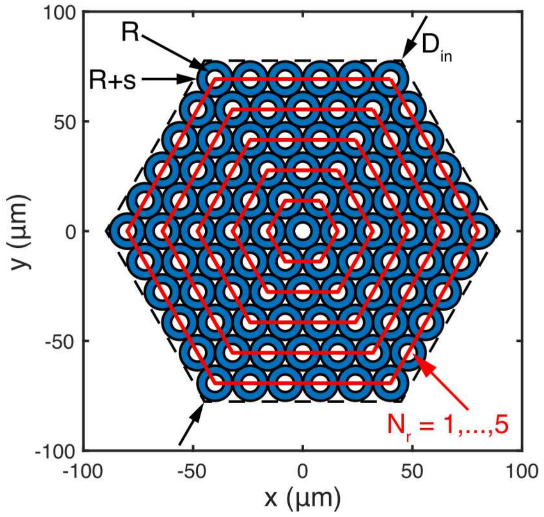

Figure 3.22. Hexagonal capillary array.

The throughput T of a polycapillary lens depends on the solid angle Ω subtended by the entrance aperture, the fill factor ζ and the transmission efficiency of the optic ε_T:

$$T = \varepsilon_T \times \zeta \times \Omega/4\pi. \tag{3.4}$$

The solid angle for our polycapillary lenses is given in Tab. 3.2. It was calculated using the area of the hexagonal structure:

$$\Omega = \frac{3\sqrt{3}}{8}\left(\frac{D_{\text{in}}}{\text{IFD}}\right)^2. \tag{3.5}$$

The fill factor ζ takes into account that the capillaries in the hexagonal lattice have a finite wall thickness. We assume that the entire polycapillary array is composed of perfectly round individual tubes and neglect that some actual polycapillary lenses (see Fig. 3.18) are made of closely stacked hexagonal sub-bundles that are arranged in a hexagonal pattern to create the large bundle. Under this assumption, the fill factor is:

$$\zeta = \frac{8N\pi R^2}{3\sqrt{3}D_{\text{in}}^2}. \tag{3.6}$$

Here, R is the inner radius of a single capillary as shown in Fig. 3.22 and D_{in} the maximal diameter. N is the number of capillaries, which can be calculated by

$$N = 1 + 6\sum_{i=1}^{N_r} i, \quad N_r = \left\| \frac{1}{2}\left(\frac{D_{\text{in}}}{2(R+s)} - 3\right) + 1 \right\|. \tag{3.7}$$

N_r is the number of hexagonal rings the array is composed of, s the spacing (wall thickness) between capillaries. For example, the array in Fig. 3.22 is composed of 5 rings, 91 capillaries, $R = s = 4\,\mu\text{m}$, and $D_{\text{in}} = 176\,\mu\text{m}$. The ratio of capillary spacing to capillary radius is 1, resulting in a fill factor of $\zeta = 22.73\,\%$.

Fig. 3.23 shows a plot of Eq. (3.6) versus the ratio of polycapillary spacing to capillary radius. D_{in} and R were kept constant, s, N_r and N were calculated for each data point. The blue curve is from a Monte-Carlo ray-tracing simulation, the orange curve is Eq. (3.6). At zero spacing ($s = 0$), ζ reaches the densest-possible packing of $\pi\sqrt{3}/6 = 90.69\,\%$, which can be calculated by selecting an N_r to calculate N and D_{in} from Eq. (3.7) and inserting into Eq. (3.6). In real polycapillary lenses, though, for example IfG #246mls19 shown in the electron microscope image on the bottom left of Fig. 3.18 and Tab. 3.2, the walls have non-zero thickness. For IfG #246mls19 the ratio is $s/R \approx 1.125$, resulting in $\zeta \approx 20\,\%$.

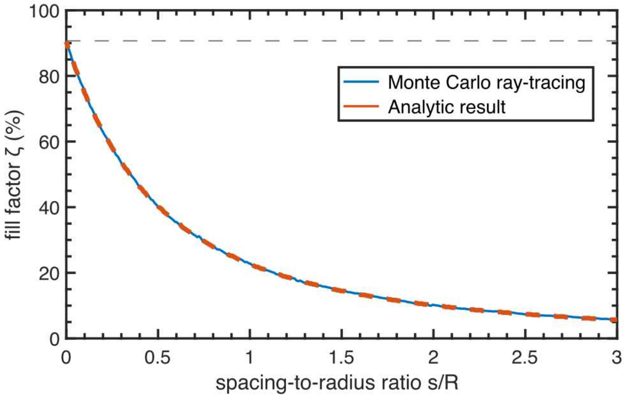

Figure 3.23. Fill factor ζ vs. ratio of capillary spacing to capillary radius s/R. For zero spacing, the maximum fill factor is $\pi\sqrt{3}/6 = 90.7\,\%$ (gray dashed line). The blue curve is from a Monte-Carlo simulation, the orange curve is Eq. (3.6).

The last remaining quantity describing the total transmission of a polycapillary lens is the transmission efficiency ε_T. The transmission efficiency describes the total reflection efficiency of the bundle of capillaries, which in turn depends on the curvature and diameter of the capillaries, the x-ray energy and θ_c, surface roughness, waviness, etc. ε_T is hard to describe analytically. The stronger a capillary is bent, i.e., the outer capillaries in the bundle are curved stronger to re-focus the diverging x-rays, the more sensitive is the transmission efficiency to the incidence angle (and therefore θ_c) with respect to the local surface. While an analytic description may exist we could not find any description in the literature and have to refer to ray-tracing calculations. Fig. 3.24a shows throughput (T) vs. x-ray energy provided by the vendor for two of our polycapillary lenses. A third result is shown using our own ray-tracing simulation and a different geometry. Since ζ and Ω are constant for any given optic, ε_T clearly scales inversely proportional to the x-ray energy. This is in part due to the energy-dependence of the critical angle (see Eq. (3.2)), the second contribution is most likely due to the curvature. At low energies (6 keV), our ray-tracing code indicates all x-rays entering a capillary impinge on the inside surface with $\vartheta < \vartheta_c$ and therefore $\varepsilon_T = 1$. For higher energies ε_T decreases. For example, at 10 keV (17.4 keV) in our particular geometry, about 10 % (18 %) of x-rays are lost in transmission. Since this loss is geometry-dependent, the three curves shown have different slopes. The annotations show the power functions that fit the data. Developing scaling laws is left open for future work.

The throughput ratio of both XOS data sets is shown in Fig. 3.24b. The improved XOS #8968 not only has larger solid angle, the transmission efficiency ε_T has been much improved and actually increases towards higher energies compared to the smaller-diameter design. At 17.4 keV the larger-diameter capillary is 2.5× more efficient than the smaller-diameter model. Future optimizations might yield even better performance as indicated by the geometry simulated using our ray-tracing code.

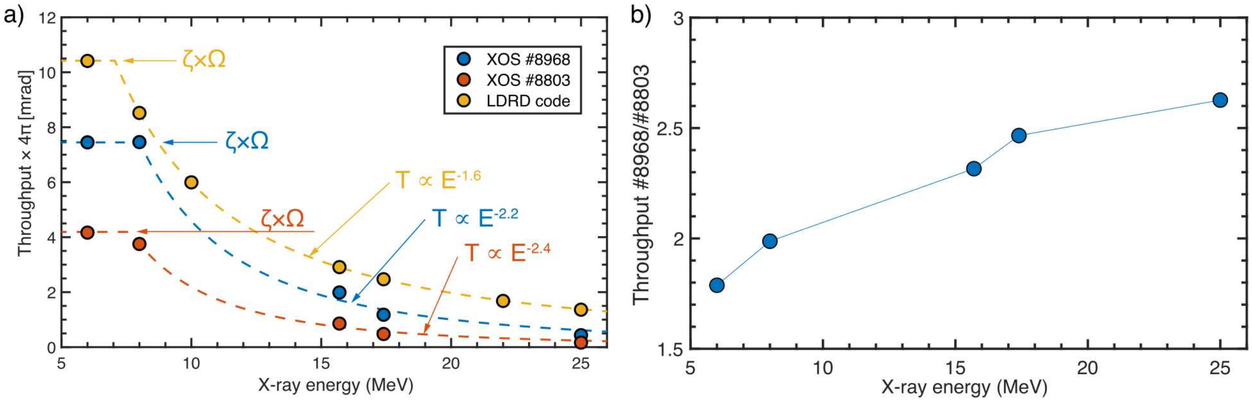

Figure 3.24. Polycapillary throughput vs. x-ray energy. The XOS data points are provided by the vendor, the LDRD code data points were generated in this project. The dashed lines in a) are fits indicating that the throughput vs. energy is geometry-dependent. The input efficiency $\zeta \times \Omega$ is calculated with Eqs. (3.6) and (3.5). b) Shows the relative throughput improvement of the enhanced design #8968 compared to the previous design #8803.

3.6.2 Polycapillary integration into PACMAN

The integration of a polycapillary lens to the PACMAN required retrofitting the PACMAN with a suitable holder for the the lens. The arrangement of the glass capillaries strongly scatters visible light, which means an alignment laser beam cannot be used to mark the capillary axis. Following the suggestion by Maddox *et al.* [4] a holder with double pinhole collimator was designed. The initial tests at the 100 TW target chamber from December 2016 to February 2017 were done with a 3d-printed holder with two adjustable irises before and after the lens. A rendering of this holder is shown in Fig. 3.25. The lens holder is mounted to a 5-axis stage (x, y, z, tip, tilt), which is mounted onto a breadboard in front of PACMAN. The 25-μm thick, $\approx 250 \times 250\,\mu\mathrm{m}^2$ laser target was glued onto a 7-μm diameter, few-mm long fiber held by a stalk on the target positioner. Such a small target was chosen because it matches the capillary FOV (see Fig. 3.20). Small targets can increase the energy density and K_α yield when irradiated by the short laser pulse [61]. An alignment laser was mounted to the back side of PACMAN to mark the x-ray beam axis from the alignment laser position to the ZPW target. The polycapillary lens was removed from the holder and the double pinholes—which are coincident with the polycapillary axis—were used to translate the holder to the alignment laser axis. Following this alignment, the polycapillary lens was put back and a ZPW laser shot was taken. While we could successfully align the lens and acquire a diffraction pattern, the shot-to-shot reproducibility was very poor. We determined that pointing a laser to the ZPW target and aligning the double pinhole collimator by eye was not precise enough. Furthermore, the polycapillary holder still had a rotational degree of freedom. If the capillary array is not perfectly co-aligned to the central axis of its stainless steel enclosure, the x-ray beam axis determined by the polycapillary lens would differ from the optical alignment axis, i.e., the lens exhibits a bias angle.

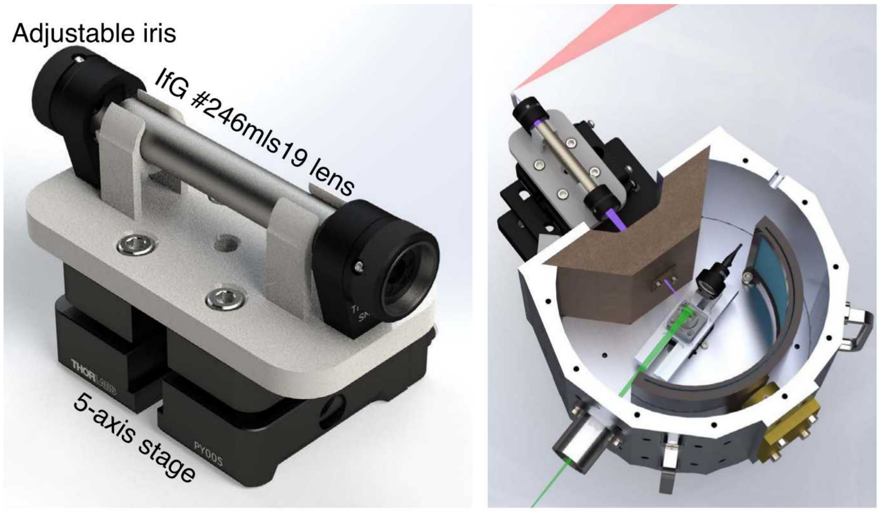

Figure 3.25. Initial polycapillary holder. The left image shows the capillary clipped into a 3d-printed holder, which is mounted to a 5-axis stage (Thorlabs PY005). An adjustable iris (Thorlabs SM05D5D) is mounted on each side of the lens. The right image shows the assembly installed in front of the PACMAN.

3.6.2.1 Pre-shot alignment procedure

A major effort was started to design and build an integrated platform that enabled a pre-shot alignment of the x-ray source to the polycapillary axis using x-rays emitted by the source to avoid bias angle issues. The new design should remove all possible degrees of motional freedom in the polycapillary lens, allow for a precise laser-target positioning, and protect the polycapillary adequately from target debris and accidental laser exposure.

Fig. 3.26 shows a CAD rendering of the integrated platform. Both the polycapillary lens and the laser target are mounted to the same bottom plate (dark yellow). The polycapillary lens is held inside of a precision-machined Al cage cube (Thorlabs SC6W). Commercial cage cube parts are used to hold a polyimide-Al-polyimide debris shield in front of the lens. This debris shield is replaced after each laser shot. The polycapillary cage is mounted to the top part of a 1″×1″ kinematic base, which allows repeatable removal of the lens for alignment purposes. The commercial kinematic base only has a central tapped hole for an #8-32 screw, which does not restrict rotational motion. Two perpendicular grooves were milled into the top of the base and a matching pair of lips were machined into the cage cube adapter plate to remove this rotational freedom. For alignment to the PACMAN optical axis, the polycapillary cage plus kinematic base adapter can be replaced with a double pinhole cage cube equipped with adjustable irises. The cage-to-base-plate adapters have the same machined lips and grooves. The bottom piece of the kinematic base sits on a 3d-printed riser (recognizable by the circular vent holes on the side).

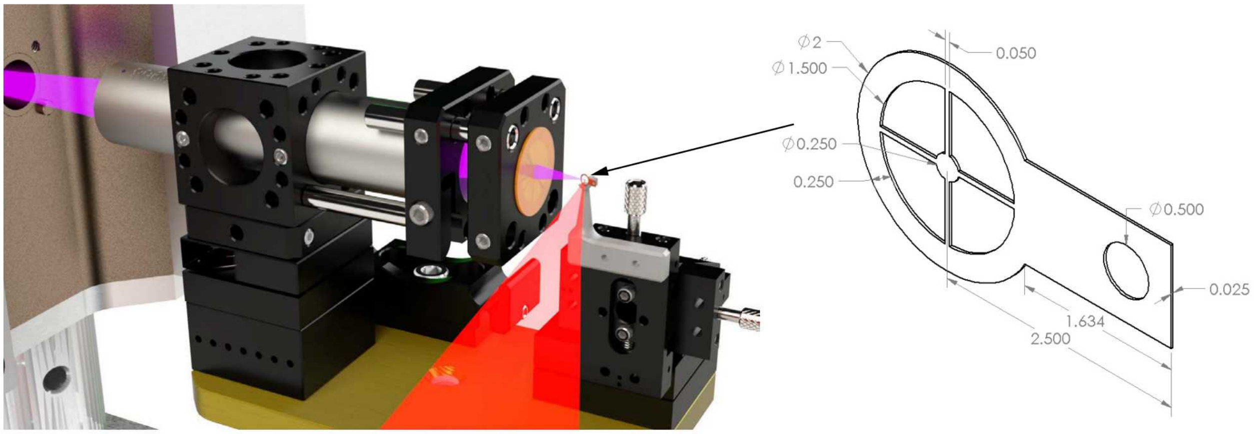

Figure 3.26. Integrated polycapillary and laser target platform. The dimensions of the laser-micro-machined target are in mm.

Since the polycapillary FOV is about 300 µm in diameter, new laser targets, shown in Fig. 3.26 on the right side, were designed that have a central disk of either 250 µm or 500 µm diameter. This central disk is connected to an outer 1.5-mm diameter support ring with four 50 µm strands. This design serves two purposes: the small disk can be centered accurately at the alignment source location, and the ZBL or ZPW laser focus can be accurately pointed to the center of the disk. The ring can be glued to a mount that connects it with the 3-axis alignment stage. For both easier handling with tweezers and to connect a grounding wire in alignment tests with the electron beam (see below), the laser target has an about 1.5-mm long tab with a 0.5-mm diameter hole on one side. These targets were fabricated by Oxford Lasers with fs-laser micro-machining. A total of 600 targets were made: four materials (Mo, Sn, Zr, Cu), three thicknesses (25, 50 and 100 µm), and for each combination 25 targets with 250 µm diameter central disk and 25 with 500 µm central disk. Target mounts are produced in-house using a Formlabs Form2 stereo-lithography printer. The mounts holds the target at a reproducible angle with respect to the ZBL/ZPW laser and polycapillary axes. This mount gets destroyed on shot and has to be replaced.

The initial alignment of the x-ray source to the polycapillary axis is performed in a dedicated small vacuum chamber equipped with a Kimball Physics 30 keV electron source with up to 100 µA. The polycapillary alignment assembly is shown in Fig. 3.27a. The laser target is replaced with an alignment source on a 3-axis piezo stage. The alignment source consists of a 1-mm diameter stainless steel rod with conical, 100-µm tip that emits K_α x-rays when excited by the electron beam. This rod was press-fitted into the conical hole of a 2-mm diameter graphite disk. A camera is used to observe the source. The graphite emits visible light when it is hit by the 500-µm diameter electron beam, enabling a precise alignment of the beam to the center of the rod forming a Fe K_α x-ray source. A Princeton Instruments PI•LCX:1300 x-ray CCD camera is used to observe the x-ray beam behind the polycapillary. Optimum alignment of the source to the polycapillary axis is achieved by maximizing the x-ray flux using minimal electron current. An optimized CCD image is overlaid in the top left corner of Fig. 3.27a.

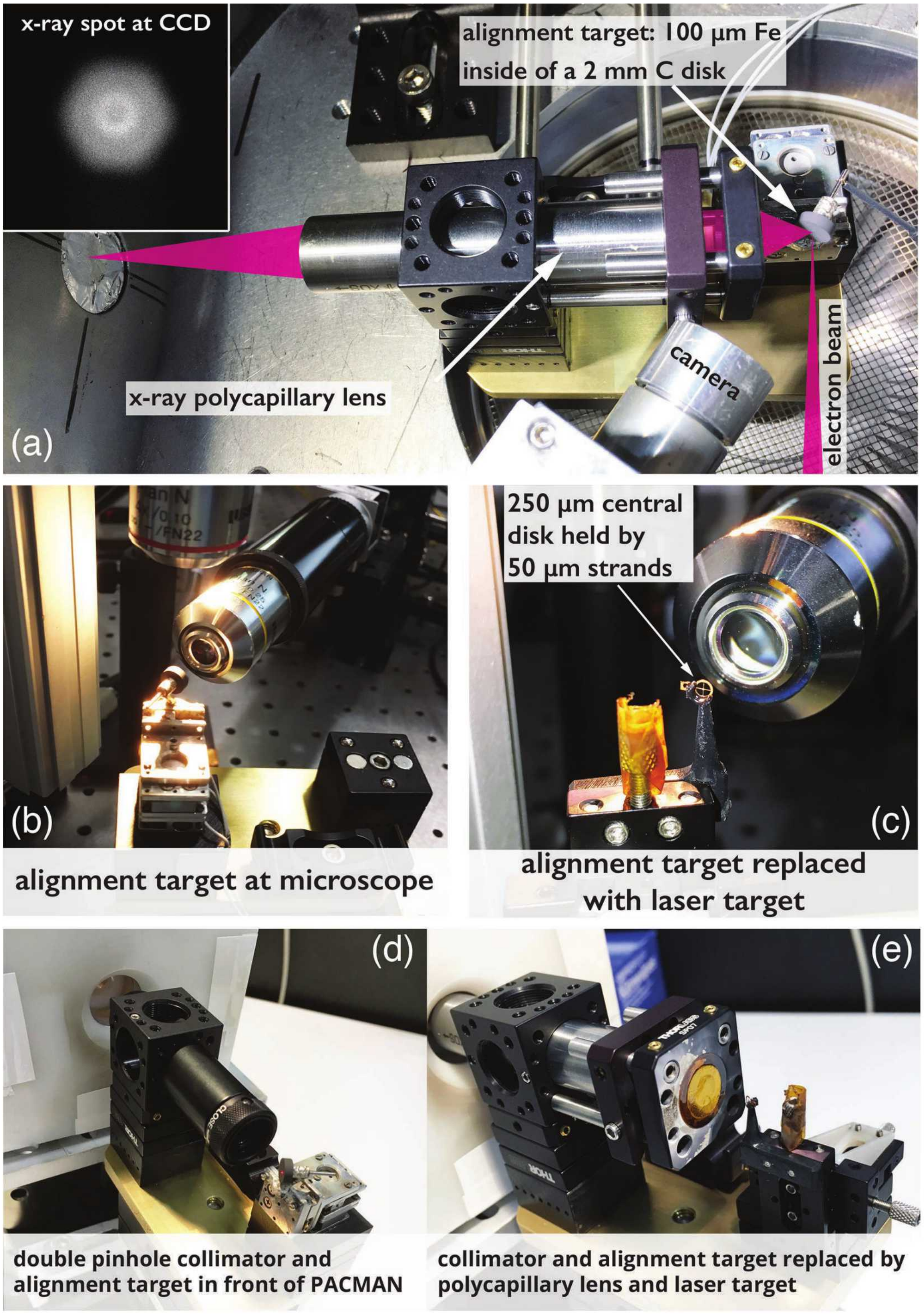

Figure 3.27. Polycapillary alignment procedure. Top: polycapillary lens and alignment target at the electron beam source. The inset shows the CCD image for an aligned polycapillary. Center: the assembly at the long distance microscope, which is used to replace the alignment target (left) with the shot target (right). Bottom: assembly with double pinhole collimator in front of PACMAN (left), and final step showing the polycapillary, debris shield and laser-micro-machined target.

After pre-alignment, the assembly is moved to a long-distance microscope with two cameras, shown in Fig. 3.27b. Using the cameras, the piezo stage and alignment source are replaced with a manual 3-axis stage that holds the laser-micro-machined target (see Fig. 3.27c). Alignment is complete when the disk is centered on the camera fiducials. Next, the assembly is moved to the PACMAN and mounted on the 5-axis stage. Line-of-sight alignment between the polycapillary lens and the XRD sample—which is less critical than the x-ray source alignment—is performed by replacing the polycapillary with a double pinhole collimator that mounts to the same kinematic base plate as the polycapillary. A laser beam serves as the optical axis to which the double pinhole collimator is aligned. Before the x-ray generation shot, the polycapillary lens and laser target are reinstalled and debris shields are installed to protect the lens. Fig. 3.28 shows the final assembly right before it was moved into Chama for a ZPW shot.

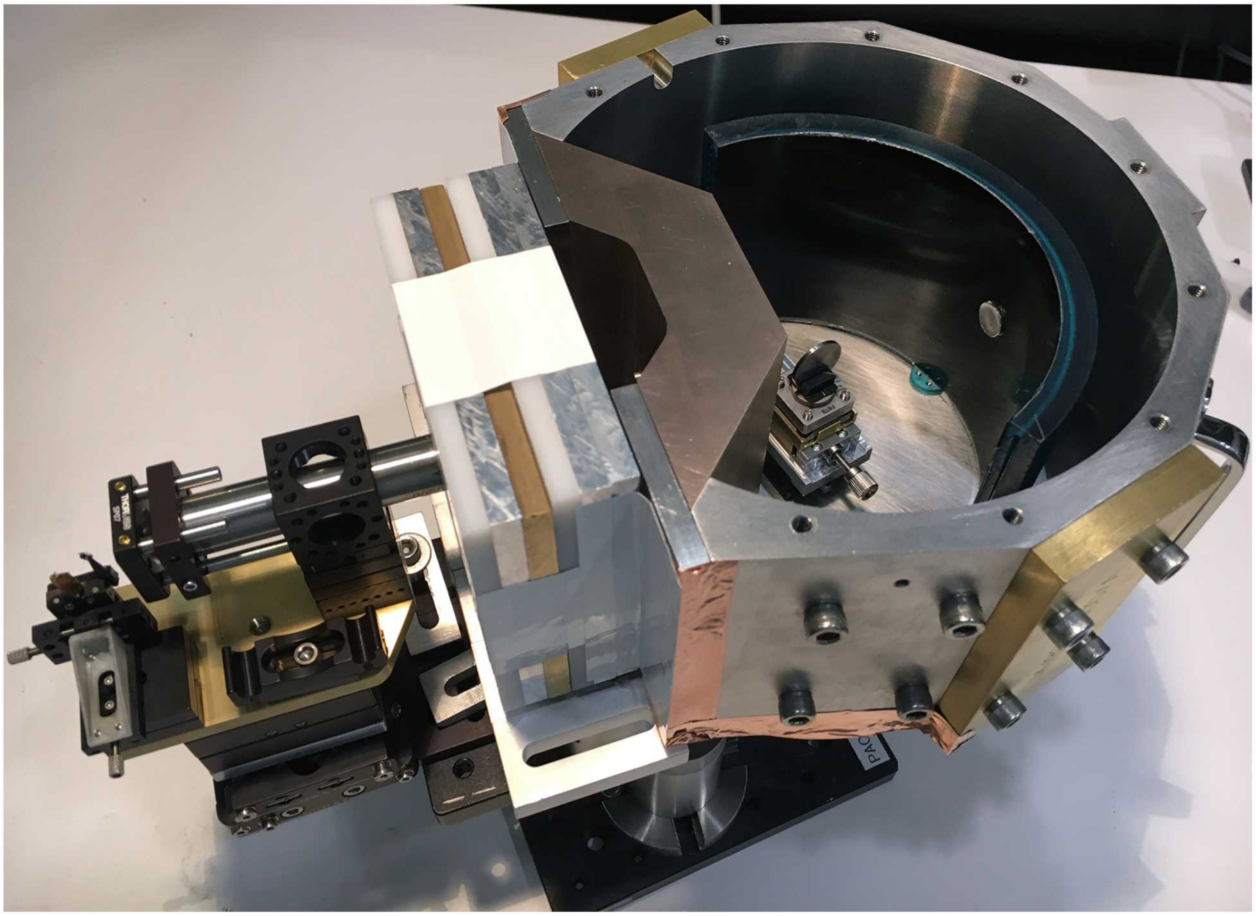

Figure 3.28. Polycapillary and laser target mounted to the PACMAN prior to a static XRD shot without Chaco. A Be disk was used as sample. A stack of six 1/4-in. (6.35 mm) shielding plates (Al, polyethylene, brass) was placed in front of the PACMAN. The Chaco laser entrance hole and PDV fiber cutouts were covered with 1/4-in. (6.35 mm) brass plates to reduce the background.

3.7 Single Photon Counter for Chama

Single-photon-counting x-ray charge-coupled device (CCD) spectrometers are frequently used in laser experiments, mostly for K-shell spectroscopy to determine the absolute x-ray yield [62–64]. For single-photon counting, the incident x-ray flux is attenuated such that the probability that two x-ray photons hit a single pixel is small. Consequently, the charge value of each readout pixel is proportional to the deposited energy from the incident x-ray photon. If the x-ray energy is not too high ($\lesssim$30 keV), a significant fraction of the x-ray photons deposit all their energy in one pixel. In this case, a histogram of the pixel values provides the incident x-ray spectrum. This type of spectrometer has the benefit of requiring no alignment and it provides absolute x-ray flux information.

A single photon counter (SPC) detector, based on a Princeton Instruments PI•LCX:1300 x-ray CCD camera, had been operated at the Z-Backlighter Facility for the first time in October 2008 [65] to measure the Fe He$_\alpha$ x-ray yield generated by ZBL. The SPC was then installed at the 100 TW target area of ZPW one year later to determine the photon yield of 25 keV K$_\alpha$ x-rays [66]. Since then, this diagnostic became a staple of the 100 TW diagnostic suite to measure x-ray yields (e.g., 15.7 keV x-rays from Zr [49]).

Typically, SPCs are positioned a few meters away from TCC to a) reduce the photon signal level impacting the CCD, and b) to reduce the large electromagnetic pulse (EMP) generated when the laser fires [63]. If the horizontal TCC plane of a target chamber is roughly at the same level as the surface of the surrounding optical tables, as for example the 100 TW target chamber, SPCs can be easily installed by placing the CCD on a small pedestal on the table surface. The laser beam line in the Target Bay, however, is much higher (approximately at eye level) to accommodate large equipment such as vacuum pumps and motorized stages underneath the laser optics. Furthermore, the arrangement of the target chambers (Jemez, Pecos, Chama) and connected vacuum beam pipes do not leave much space for additional optical tables. The 4-in. thick Chama chamber doors are equipped with TCC-facing viewports only in the horizontal plane or in a direction pointing up at 12.25°. The SPC requires a direct line of sight to the target at TCC, hence the camera had to be installed opposite of a viewport. Another requirement was that the SPC should be able to look at the target front surface independent of the laser system (ZBL or ZPW) being used. We decided the most suitable installation location was a custom shelf, mounted to the large vacuum flange of the north-west (NW) corner periscope tower (see Figs. 3.1 and 3.2).

The custom structural components of the shelf, shown on the top left in Fig. 3.29, include an anodized Al frame with a breadboard shelf (Thorlabs MB1836). The system can support a maximum of 429.4 lbs ($\approx$200 kg) with a safety factor of 5 based on yield stress. The estimated weight of the single photon counter and optional tungsten shielding is only 80 lbs (36 kg), however, care was taken to ensure that the breadboard would experience minimal deflection under this load. Accordingly, the deflection at the end of the breadboard was 0.4 mm based on a finite element analysis of the structural assembly. The purpose of minimizing deflection was to help maintain alignment of the SPC.

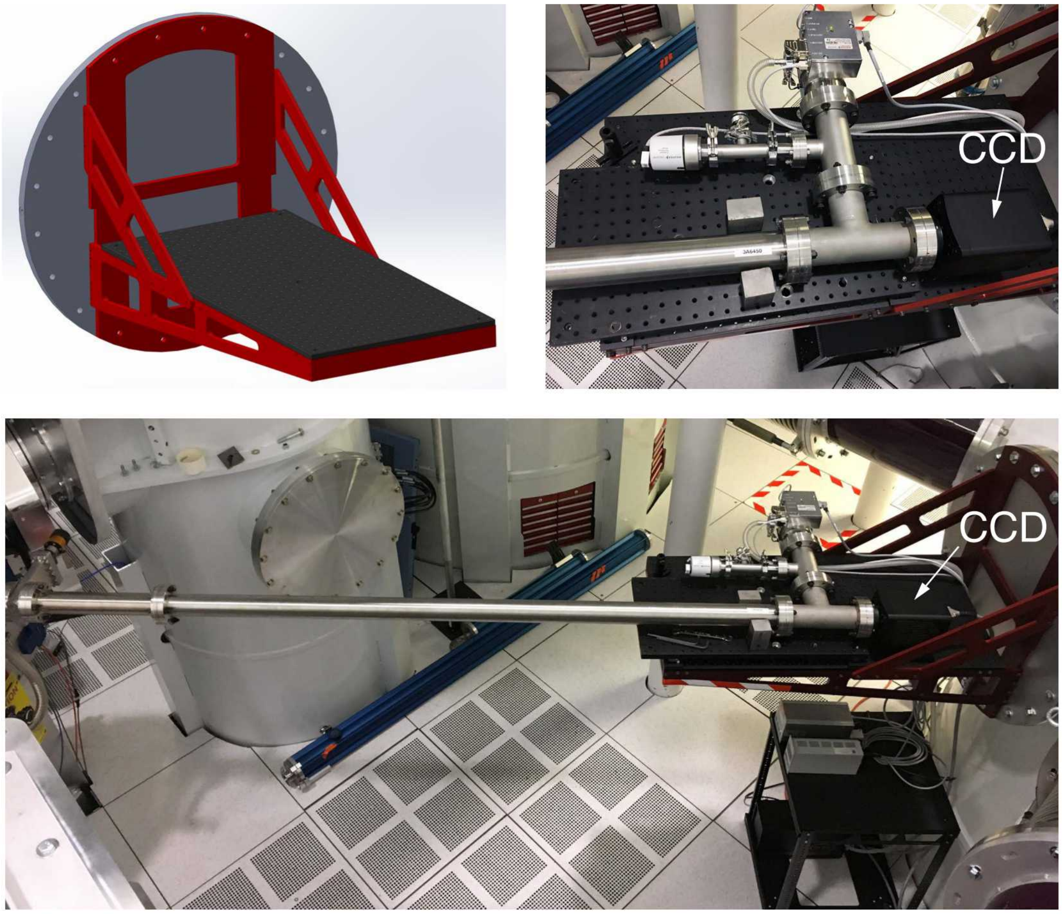

Figure 3.29. Single Photon Counter at Chama. Shown on the top are a rendering of the custom shelf (left) and the CCD camera at the end of the tube plus vacuum equipment (right). The bottom image shows the vacuum pipe connected to Chama on the left and the shelf plus CCD on the right.

An evacuated line-of-sight (LOS) tube extends from Chama to the CCD. The CCD must be evacuated and cooled during operation. To prevent visible light from reaching the CCD, and to attenuate the photons emanating from the laser target, an opaque filter is placed at the entry to the evacuated tube, against the inside surface of the Chama wall. A gate valve is installed at Chama to disconnect the Chama vacuum from the SPC vacuum volume to enable venting of Chama after the experiment without waiting for the CCD to heat to room temperature first. Because the section between Chama and the gate valve is pumped by the Chama vacuum system, a bypass hose with shutoff valve is used to connect the tube volume back to the Chama volume. The vacuum tube is primarily pumped from the SPC vacuum system, consisting of a roughing pump and turbo pump.

The vacuum tube between Chama and the CCD fulfills two requirements: 1) it removes the air between the target and the CCD, which would attenuate low-energy x-rays ($\lesssim$8 keV) below the detection limit, and 2) there is no need for a thin vacuum window at Chama. During WP&C activities in preparation of setting up this diagnostic, the engineer tasked with calculating the safety factor for a thin Kapton vacuum window found an error in the equation that was used previously. Subsequently, we determined that safety factors for such a thin membrane, held by essentially knife edges on the CF flange, cannot be analytically calculated with high confidence. This finding was further confirmed by peers in the industry; the safety factor has to be determined experimentally, which is out of scope of this work. Due to the extremely large vacuum volume connected to Chama when the ZPW gate valve is open, we could not risk rupturing a thin membrane and releasing several MJ of energy. By designing a vacuum system for the SPC we have eliminated this risk.

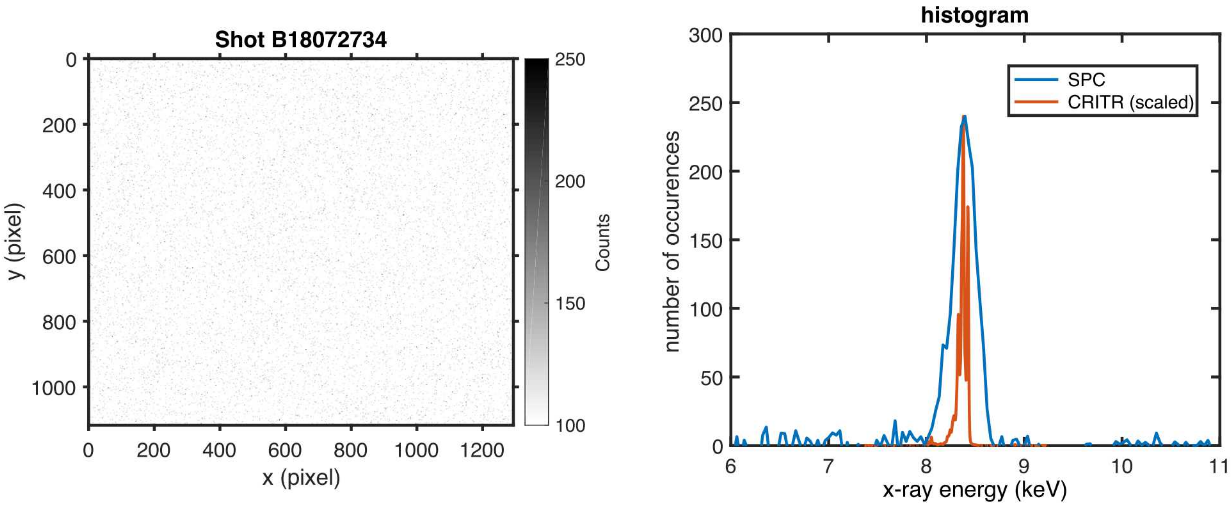

Figure 3.30. Single Photon Counter spectrum. (left) CCD image showing the single photon exposure. (right) Energy-calibrated histogram compared to scaled CRITR spectrum of this shot.

Fig. 3.30(left) shows the CCD image from a ZBL shot on a Cu target as an example. A histogram was generated using the procedure described in [66]. The CCD response vs. single photon x-ray energy was calibrated using the radioactive calibration sources Fe-55 and Cd-109. The right plot shows the resulting spectrum. For comparison, the spectrum measured by the CRITR spectrometer on the same shot is plotted as well. Since the SPC is absolutely calibrated, the spectrum can be integrated and corrected for filter transmission and solid angle captured by the CCD to measure the total yield. In this shot $1.7 \times 10^{14} \pm 10\,\%$ Cu He$_\alpha$ photons were generated, resulting in a laser-to-x-ray energy conversion efficiency of $3 \times 10^{-4} \pm 15\,\%$. Shot-to-shot variations for ZBL Cu conversion efficiency range between $3 - 6 \times 10^{-4}$.

This page intentionally left blank.

4. DIFFRACTION SIMULATION AND ANALYSIS CAPABILITIES

A crystalline solid is a material whose atoms are arranged in a definite, repeating pattern in three dimensions (3D), which form a "Bravais" (crystal) lattice that extends in all directions [67]. In 3D space, there are 14 Bravais lattices that are grouped into 7 lattice systems: triclinic, monoclinic, orthorhombic, tetragonal, cubic, trigonal, and hexagonal. For example, there are 3 lattices in the cubic system: the simple cubic (sc) lattice, the body-centered cubic (bcc) lattice, and face-centered cubic (fcc) lattice. Crystallographic planes are described using Miller indices (hkl), which are derived from the intercepts of the plane with the lattice. The reciprocal lattice represents the Fourier transform of the Bravais lattice that exists in real (physical) space. Analogously, the reciprocal lattice exists in reciprocal space or momentum space (also known as *k-space*). In the process of x-ray diffraction, the momentum difference between incident and diffracted x-rays of a crystal is a reciprocal lattice vector. The x-ray diffraction pattern of a crystal can be used to determine the reciprocal vectors of the lattice, thus elucidating the atomic arrangement of the crystal.

A single crystal or monocrystalline material has an atomic structure that repeats periodically across its whole volume, where each atom is related to every other equivalent atom in the structure by translational symmetry. The entire *monocrystalline* sample is continuous and unbroken to the edges of the sample, with no grain boundaries. A *polycrystalline* material is made up of an aggregate of many small single crystals (crystallites or grains). Polycrystalline materials have a high degree of order over many atomic dimensions. These ordered regions, or single crystal regions, vary in size and orientation with respect to one another, and are separated from one another by grain boundaries.

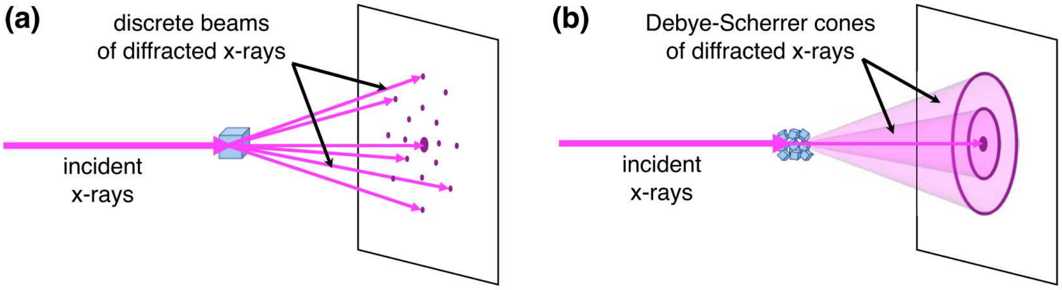

Figure 4.1. Monocrystalline vs. polycrystalline XRD. a) In a monocrystalline material, the individual reciprocal lattice points are projected onto the detector as discrete peaks. b) In polycrystalline material with randomly oriented crystals the reciprocal lattice points for each of the crystallites combine to form Debye-Scherrer cones.

Fig. 4.1 presents the x-ray diffraction (XRD) patterns measured by a 2D detector of ideal mono-crystalline and polycrystalline materials. For an ideal mono-crystalline material, the individual reciprocal lattice points are projected onto the detector as discrete peaks at associated diffraction angles. The locations of the measured peaks are used to determine the values of the (hkl) planes that the x-rays were diffracted from (see Fig. 4.1a). For an ideal polycrystalline material, the numerous small crystallites are randomly oriented with all possible orientations present. The reciprocal lattice points for each of the crystallites combine to form “Debye-Scherrer” cones of diffracted x-rays that produce continuous rings on the detector (see Fig. 4.1b), which is usually called a “powder” XRD pattern. In reality, most polycrystalline materials have grains of varying sizes and some preferential orientation (texture), which tend to produce incomplete or spotty diffraction rings on the detector.

4.1 Modeling of X-Ray Diffraction Patterns

We used the Powder Cell software [68] to model x-ray diffraction patterns of various materials and x-ray energies (wavelengths) to guide the experiments. Structure models used in Powder Cell originate from the Inorganic Crystal Structure Database (ICSD). The following models were used: Zr alpha ICSD #426988; Be hcp ICSD #190781, Al cubic ICSD #606007.

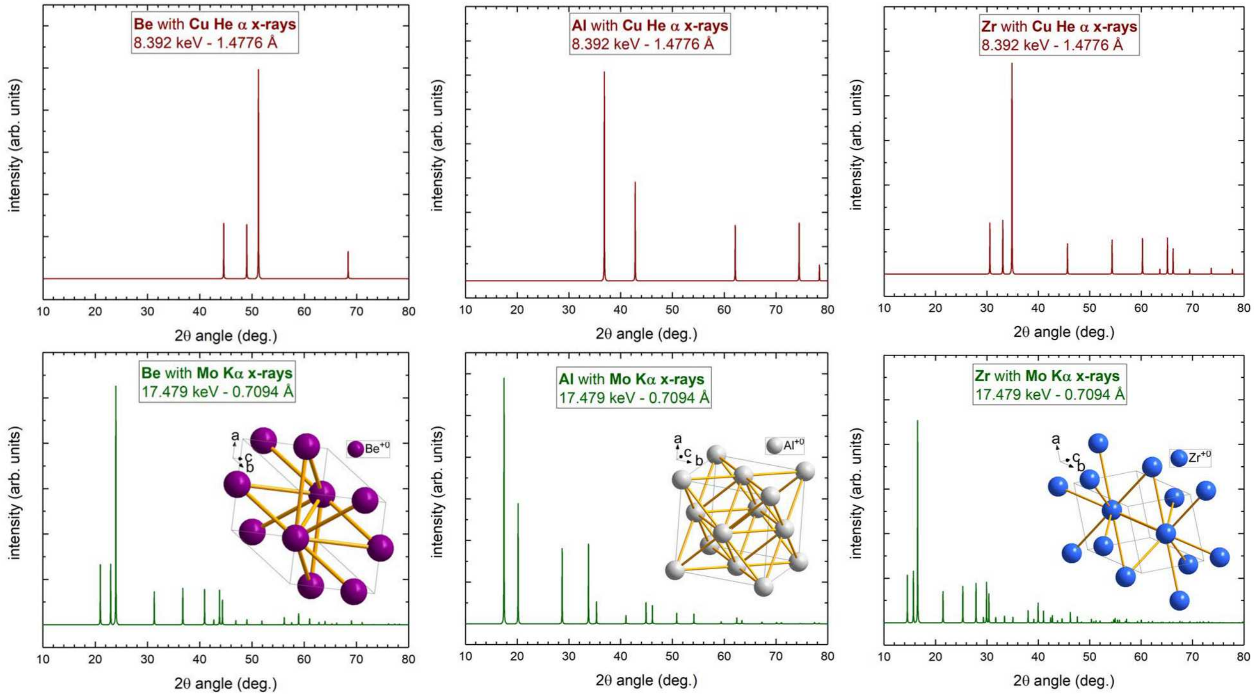

Figure 4.2. X-ray diffraction pattern modeling using Powder Cell of the ambient structure of Be, Al and Zr with two different x-ray energies. Greater energies (smaller wavelength) allow capturing a wider *d*-spacing range within the same angular range of the imaging detector. The insets show the crystal structure. See text for details.

Fig. 4.2 shows x-ray diffraction pattern models of the ambient structure of Be, Al and Zr for two different x-ray energies. The insets show the crystal structure of Al (Fm$\bar{3}$m, space group #225), with a cubic unit cell, and of Zr and Be (both P6_3/mmc, space group #194), with a hexagonal unit cell.

For Cu He$_\alpha$ x-rays at 8.4 keV (upper row), the strongest peaks can be found between $2\theta = 30°$ to 50°. Approximately doubling the x-ray energy to Mo K$_\alpha$ at 17.4 keV (lower row) moves the strongest peaks to approximately half the 2θ value (closer to the x-ray beam axis). At the same time, the diffraction pattern is being compressed in its angular range, which enables capturing a wider d-spacing range within the same angular range of the imaging detector.

4.2 Spatial Integration of Measured Diffraction Patterns

Fig. 4.3 shows an example of a typical XRD pattern measured on the cylindrical IP of the PACMAN instrument, which was "flattened" and scanned to produce the 2D image. The XRD pattern was obtained from a static Be sample using ZBL generated Cu He$_\alpha$ (8.4 keV) x-rays. Multiple diffraction rings were clearly observed around the bright straight-through x-ray beam spot centered at the (x, y) origin. This XRD pattern was obtained using a polycapillary lens and it is further analyzed in Sec. 5.3.1.

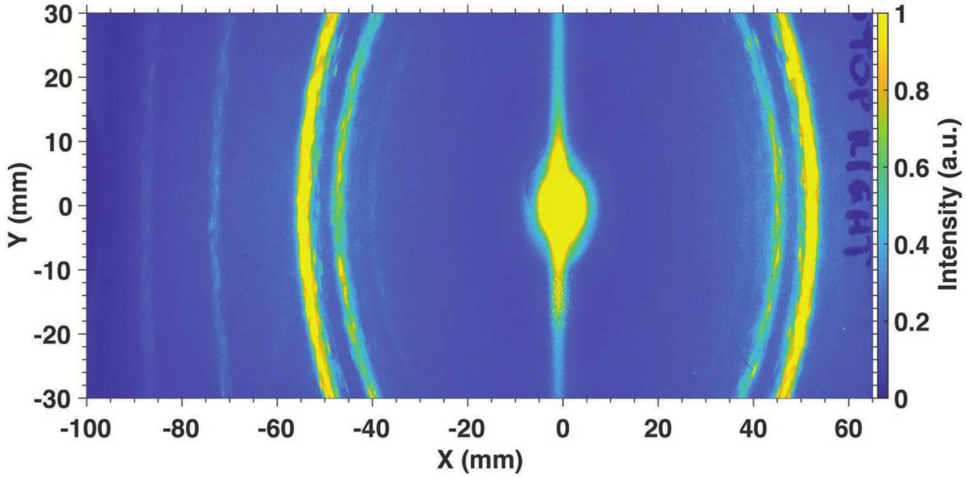

Figure 4.3. Example of an XRD pattern measured on cylindrical IP of the PACMAN instrument. Shot B17110900, ZBL, 1.1 kJ, 8.4 keV Cu He$_\alpha$ x-rays diffracted from a static Be sample.

For a quantitative analysis of the diffraction pattern, the 2D image needs to be integrated spatially to generate an intensity vs. 2θ angle diffraction plot. While freely available software exists for these purposes such as Dioptas [69], we have found that Dioptas is not optimized for cylindrically curved detectors since the vast majority of today's 2D XRD detectors are CCD or CMOS based and therefore flat.

A new analysis code was written using Matlab to integrate the measured XRD pattern, and is included as a "Diffraction Class" in the Sandia Matlab AnalysiS Hierarchy (SMASH) toolbox [70]. The analysis of the XRD pattern starts by remapping the 2D image to a cylindrically curved surface with the appropriate experimental parameters (see Fig. 4.4a). Specifically, the cylindrically curved surface with a radius of curvature of 60 mm was centered around the Be sample located at the (x, y, z) origin. The incident x-rays propagate along the z-axis into the Be sample. The straight-through x-rays exit the Be sample and intersect the bright beam spot on the IP.

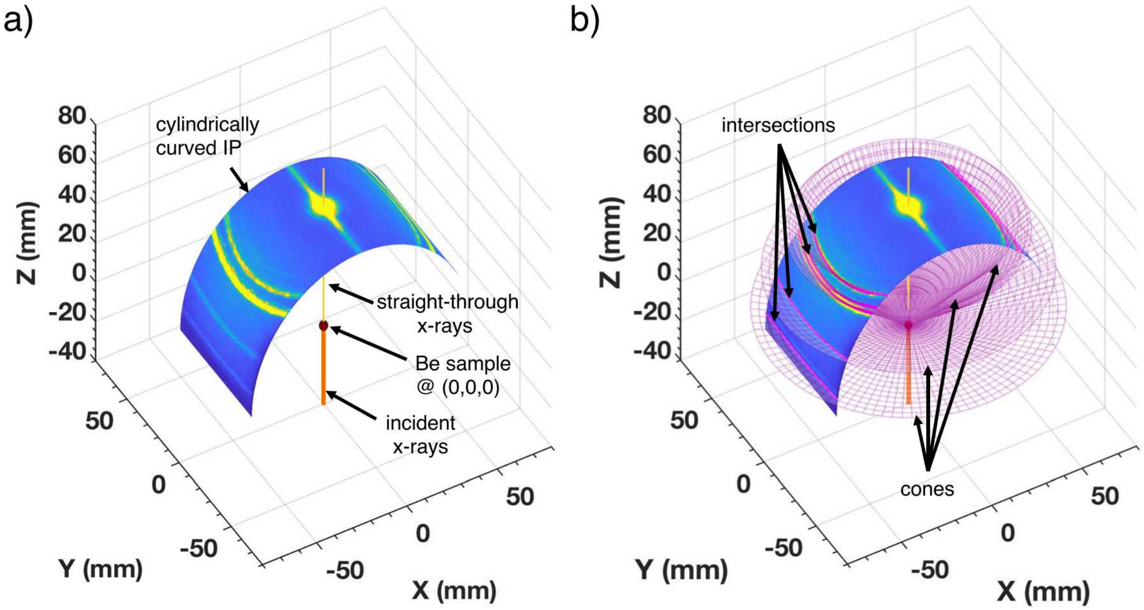

Figure 4.4. Cylindrically curved surface for spatial integration. a) Cylindrically curved surface with Be sample, incident x-rays, and straight-through x-rays. b) Cylindrically curved surface intersections with Debye-Scherrer diffraction cones for known (hkl) planes of ambient Be.

Ambient Be has a hexagonal close-packed (hcp) structure with known diffraction angles for hkl planes of (100), (002), (101), (102), and (110), see top-left in Fig. 4.2. The calculated Debye-Scherrer cones of the diffracted x-rays for these known hkl planes were used to calibrate the XRD pattern as shown in Fig. 4.4b. The intersections of the diffraction cones with the cylindrically curved surface agree very well with the measured diffraction rings, thus validating the analysis parameters.

To complete the analysis, a series of diffraction cones was similarly calculated at varying diffraction angles. For each diffraction cone, its intersection with the cylindrically curved surface generated an arc to integrate along for that specific diffraction angle. Fig. 4.5 shows the resulting linear XRD profile as a function of diffraction angle, which agrees well with the diffraction angles for the known (hkl) planes of ambient Be.

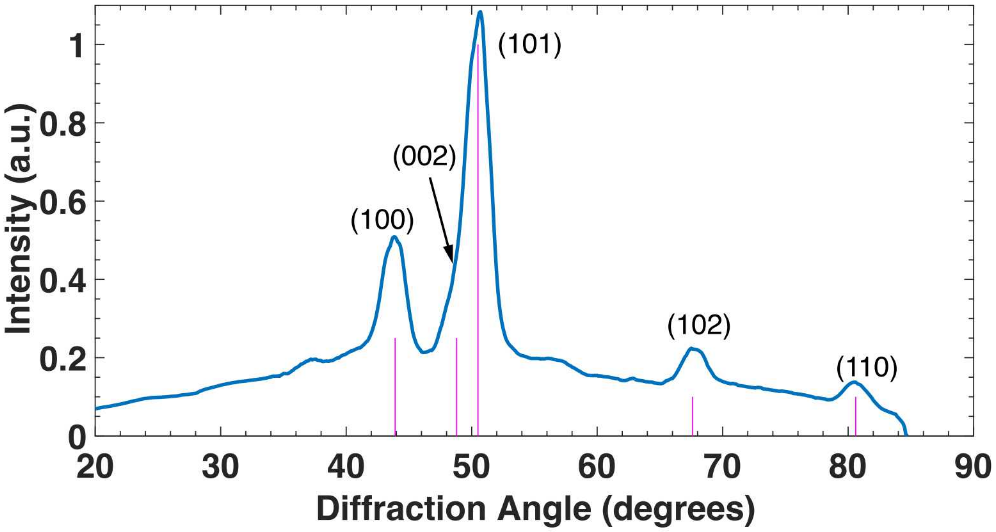

Figure 4.5. Spatially integrated XRD pattern. The linear XRD profile was obtained through arc integration.

4.3 Photometric Calculations

X-ray diffraction is an inherently weak process. Combined with a pulsed photon source with limited energy, it is crucial to estimate the expected detector signal before an experiment is planned. Assuming a kJ of laser energy, the total number of x-ray line radiation photons emitted into 4π generated by the ZBL laser is about 10^{15} below 10 keV (see Sec. 5.2.3). Above this threshold the yield drops steeply. The ZPW short-pulse laser generates $\approx 10^{14}$ photons/kJ for all energies of relevance here. However, currently the ZPW laser is limited to a maximum energy of 250 J until the planned full-aperture upgrade is completed.

Taking the photon number $N_{\text{ph,source}}$ generated by the source, the photon flux on the sample ($N_{\text{ph,sample}}$) can be calculated:

$$N_{\text{ph,sample}} = T \times N_{\text{ph,source}}, \tag{4.1}$$

where T is the throughput of the x-ray optic (see Eq. (3.4)), which of course depends on the geometry. In the following, we use the examples of a 1-mm pinhole in 1-in. distance[1]: $T = \Omega/4\pi = 10^{-4}$, and our best-performing polycapillary lens XOS #8968 ($T \approx 0.8{-}6 \times 10^{-4}$, see Fig. 3.24). Hence, the number of x-ray photons irradiating the sample is about $N_{\text{sample}} \approx 10^{11}{-}10^{12}$ for ZBL and $N_{\text{sample}} \approx 10^{9}{-}10^{10}$ for ZPW with 250 J.

The intensity of the strongest diffraction rings can be estimated using $N_{\text{ph,sample}}$, the coherent scattering cross section σ (see [71]), x-ray attenuation length μ (see [60]) and thickness d of the

---

[1] The PACMAN design limits the minimum distance between source and pinhole to about 1 inch.

material under investigation. The total scattering fraction F is

$$F = \mu_{\mathrm{eff}}\, \sigma\, n_{\mathrm{a}}. \tag{4.2}$$

The sample atomic number density is calculated as $n_{\mathrm{a}} = \rho N_{\mathrm{av}}/M$, where ρ is the density, N_{Av} the Avogadro number, and M the molar mass. The effective attenuation length is $\mu_{\mathrm{eff}} = \min[\mu, d]$, which means the attenuation length is limited by the target thickness for thin targets.

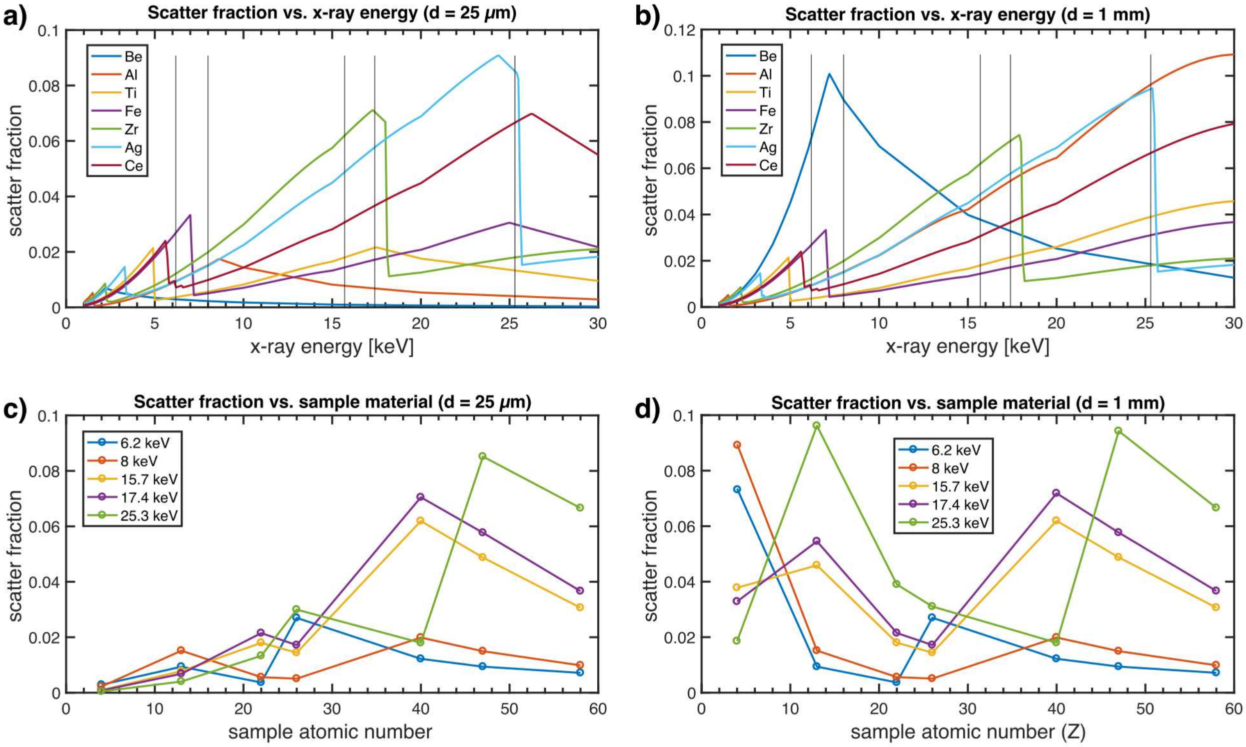

Figure 4.6. Scatter fraction vs. x-ray energy and sample material. a) and c) show the scatter fraction F versus probe x-ray energy and F vs. sample material for these x-ray energies for 25-μm thick samples. b) and d) show the same for a 1-mm thick sample. The incidence angle in both cases is 15° with respect to the surface. The vertical lines in a) and b) mark the x-ray energies shown in c) and d)

Fig. 4.6 shows plots of F versus x-ray energy and F versus material for two different sample thicknesses to show the effect of μ_{eff}. For most thin foils (Figs. 4.6a and 4.6c), the fraction of scattered photons increases with increasing x-ray energy for a given sample, as well as with increasing atomic number for a given x-ray energy. The K-edges of the materials are clearly visible. If the x-ray energy is above the K-edge for the material, the scatter cross section drops very quickly. This suggests the ideal x-ray probe for a specific material should be the K_{α} line from the material with $Z_{\mathrm{source}} = Z_{\mathrm{sample}} - 1$.

For thick samples as shown in Figs. 4.6b and 4.6d, the deeper penetration of harder x-rays results in a larger volume being probed and therefore F can increase a lot. For example, 25.3 keV

Sn K_α x-rays do scatter equally well in Al and Ag (orange and cyan lines in Fig. 4.6b, green line in Fig. 4.6d). In the thin-sample case Al is much less efficient (cf. Fig. 4.6a and c), because the attenuation length is much larger than the foil thickness.

This plot helps choosing the right sample thickness and material for a given x-ray source, or vice versa. For x-ray energies below 10 keV, thick beryllium has the highest scatter fraction of all materials under consideration with $F = 0.1$ for 7.2 keV x-rays. Higher x-ray energies such as Zr K_α at 15.7 keV or Mo K_α at 17.4 keV work best with a Zr sample. The attenuation length is 75 µm (100 µm) for 15.7 keV (17.4 keV), which after correction for the incidence angle is close to the thin-sample thickness and therefore a 25-µm Zr foil should be selected. The scatter fraction is $F = 0.06$ for 15.7 keV and $F = 0.07$ for 17.5 keV.

The diffracted x-rays are detected after a short propagation distance. The 6-cm radius PACMAN IP is usually scanned with 50 μm pixel size ($\Omega_{\text{det}} \approx 7 \times 10^{-7}$). This leads to the final expression for the detector photon fluence:

$$N_{\text{ph,detector}} = N_{\text{ph,sample}} \times F \times \Omega_{\text{det}}/(4\pi). \tag{4.3}$$

The resulting detector photon fluence in a diffraction ring is only $\approx 10^{-9}$ of $N_{\text{ph,sample}}$.

Table 4.1. Selected calculated detector photon fluence data for a 1-mm pinhole at 25 mm distance from the source compared to polycapillary XOS #8968. Values are approximate.

Sample & X-ray Energy	**ZPW, 250 J 10^{18} W/cm^2**	**ZPW, 1 kJ 4×10^{18} W/cm^2**	**ZPW, 1 kJ 10^{20} W/cm^2**	**ZBL, 1 kJ 10^{15} W/cm^2**
1 mm Be, 8 keV				
Pinhole	5	20	110	200
Polycap.	30	100	690	1100
25 µm Al, 8 keV				
Pinhole	0.75	3	20	30
Polycap.	4	16	120	200
25 µm Zr, 17.4 keV				
Pinhole	1	4	28	0.1
Polycap.	1	4	28	0.1
25 µm Ag, 25 keV				
Pinhole	0.5	2.2	17	0.01
Polycap.	0.2	0.8	6	0.004

Tab. 4.3 presents some example calculations for selected materials and x-ray energies. Laser-to-x-ray energy conversion efficiencies were taken from Fig. 5.5. In all cases except for the highest x-ray energy example, the polycapillary optic performs significantly better than a pinhole, while it also reduces the background. Assuming a 1:1 magnification for the pinhole, the polycapillary lens increases the distance between x-ray source and sample by about 3.5×, which would decrease the background by more than 10× for an isotropic source.

Due to the higher conversion efficiency for lower x-ray energies, the 1-kJ ZBL pulse results in an about 10× brighter detector signal compared to a 1-kJ ZPW pulse for 8 keV x-rays, when a lens is used for focusing. If in the future the lens in the FOA is swapped with an off-axis parabola (OAP) that allows focusing the laser to 10^{20} W/cm^2 (1 kJ in 1 ps), the difference is only about 2×. At 17.4 keV this ratio changes and ZPW is the more efficient driver; a 100-ps, 1 kJ pulse is estimated to generate about 4 photons per detector element. This could increase by seven times if an OAP were used. For 25 keV x-rays, due to the reduced polycapillary transmission, a pinhole would be the more efficient optic. However, ZPW experiments suffer from a strong electron and bremsstrahlung background as shown below, which requires strong shielding (few inches of tungsten) and a large distance to the source. For this reason a polycapillary optic and ZPW at maximum intensity and energy appear to be the only option for high x-ray energy XRD. Of course, a significant increase in photon flux (proportional to the distance squared) will be obtained if angular resolution is sacrificed and the detector is moved closer. Determination of the optimum distance will depend on the experiment and is left for future work.

4.4 Diffraction Pattern Changes in Dynamically Compressed Ce

A simulation capability was developed that uses the 1D hydrodynamics simulation code LASLO to simulate the compression of a cerium sample by an incoming pressure pulse. The hydro code does not yet include the effects of laser-plasma interaction. Instead, a 7 ns long tophat pressure pulse of 8 GPa was injected into the simulation. This pulse compressed a 10 µm Ce sample glued onto 100 µm vitreous carbon (VC). A 25 µm Al pusher layer is glued onto the Ce. The three materials are bonded with 1 µm of glue.

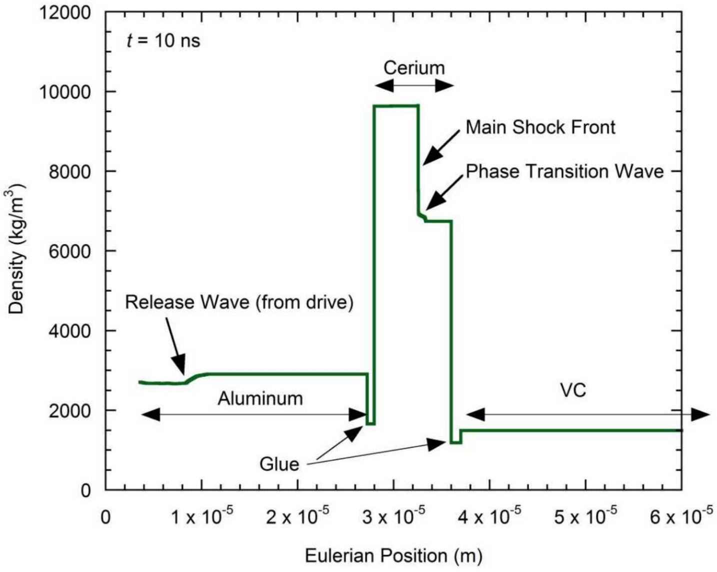

Figure 4.7. Simulated shock-compressed Ce. The density profile is shown in Eulerian coordinates at 10 ns after the start of the simulation.

Fig. 4.7 shows a snapshot of the density profile at 10 ns after the start of the simulation. The shock front has traveled about half-way through the Ce. The pressure behind the shock front has increased enough to induce the $\gamma - \alpha$ phase transition [72].

To calculate diffraction patterns, a crystal structure and input spectrum are assumed. The input spectrum assumed in this simulation are the two $\mathrm{K}_{\alpha_{1,2}}$ lines from Mo at 17.48 keV and 17.37 keV. The density from the hydro simulation is used to determine the lattice parameter and hence d-spacings that satisfy Bragg's Law (as a function of Eulerian position). Then, the input spectrum, d-spacings, and source attenuation due to absorption and scattering are integrated over position and angle. This gives self-consistent relative intensities at a fixed time in the simulation.

The diffracted intensity I of a Bragg plane (hkl) from a "plate" sample is:

$$I_{hkl} = \frac{K}{2\sigma\rho} R_{hkl}, \tag{4.4}$$

where σ is the opacity and ρ is the density of the material. The constant K depends on experimental conditions:

$$K = \left(\frac{I_0\lambda^3}{32\pi r}\right)\left(\frac{e^4}{2m_e^2c^4}\right), \tag{4.5}$$

where I_0 is the incident x-ray intensity, λ the x-ray wavelength, r the sample-to-detector distance, e the electron charge, m_e the electron mass, and c the speed of light. The factor R_{hkl} depends on the crystal structure and the specific diffracting plane:

$$R_{hkl} = \frac{M}{V^2}|F|^2\left(\frac{1+\cos^2(2\theta)\cos^2(2\theta_m)}{\sin^2(\theta)\cos(\theta)}\right)\exp(-2\theta_m), \tag{4.6}$$

where M is the multiplicity of reflection hkl, V the volume of the unit cell, F the structure factor for reflection hkl, 2θ the Bragg angle for reflection hkl, and $2\theta_m$ the source angle with respect to the sample normal. Note that Eqs. (4.4)–(4.6) use cgs units. See "Quantitative Analysis" in [73] for more details.

Fig. 4.8 shows two calculated spectra. The spectrum at 7 ns represents Ce at ambient parameters. The spectrum 7 ns later was generated after the $\gamma - \alpha$ transition occurred, which compresses the cell volume and therefore shifts the pattern to higher angles. Note that the $\gamma - \alpha$ phase transition is a polymorphic transformation from one face-centered cubic structure to another face-centered cubic structure, accompanied by a cell volume decrease of about 18 % [72].

The spectra shown in Fig. 4.7 were taken at times where both phases are well separated. However, during the propagation of the shock front and launching of the release wave, the two Ce phases overlap because parts of the sample are in high pressure phases while other parts are still at ambient conditions.

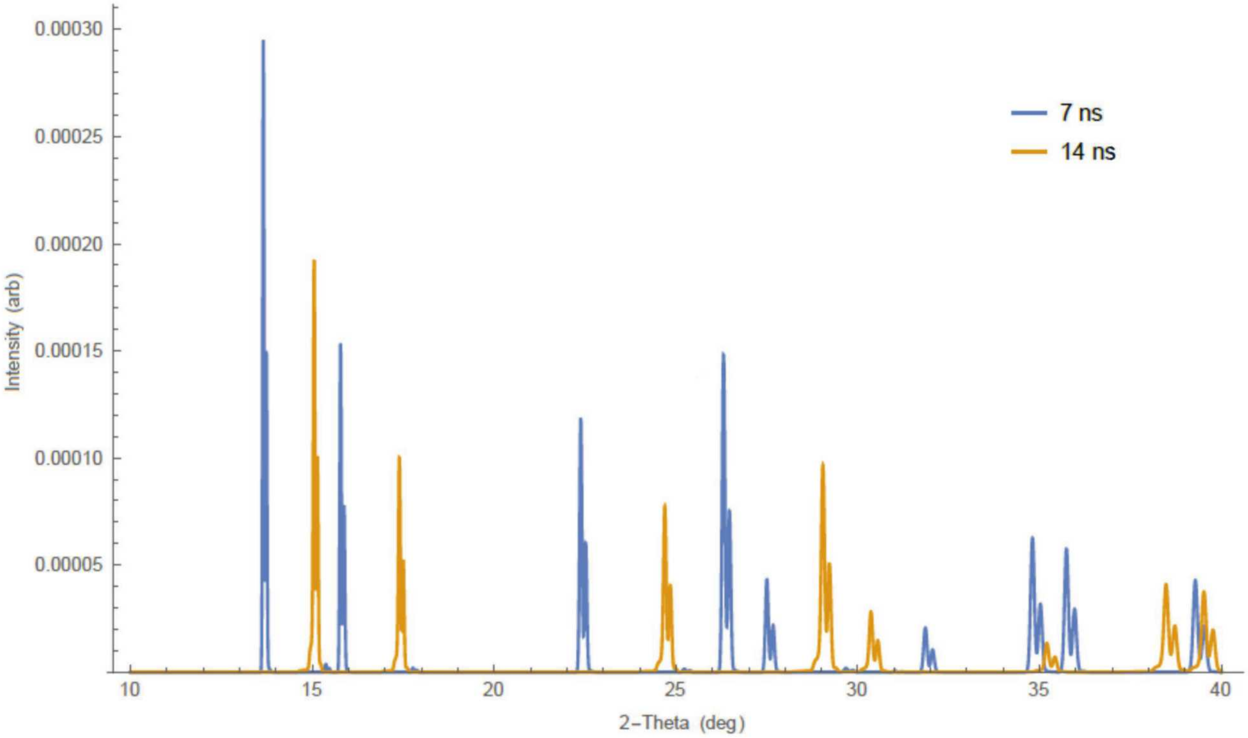

Figure 4.8. Simulated Ce diffraction patterns from hydro simulation.

The simulation results indicate that the minimum drive length is determined by release wave catch-up in aluminum, which results in complex multi-phase diffraction patterns. For the simulation shown, a minimum hold of 7 ns is needed to clearly separate the two crystal phases; a longer pulse length is desirable. A scan using different Al and Ce thicknesses shows that an Al thickness of 20-30 μm (depending on the pulse shape) works best and prevents self-reverberation (waves from Al/Ce interface interacting with drive). Furthermore, thin cerium (<10 μm) samples are likely to provide cleanest diffraction patterns.

5. EXPERIMENTAL RESULTS

5.1 Laser Compression with Chaco

With the advent of high-power pulsed lasers in the early 1970's, a new avenue for achieving ultra-high pressures became available. For several decades, various laser compression techniques have been developed to dynamically compress materials to extreme pressure states. Two standard laser compression schemes, which are typically referred to as "direct drive" [11, 74] and "flyer impact" [33, 75], are presented in Fig. 5.1

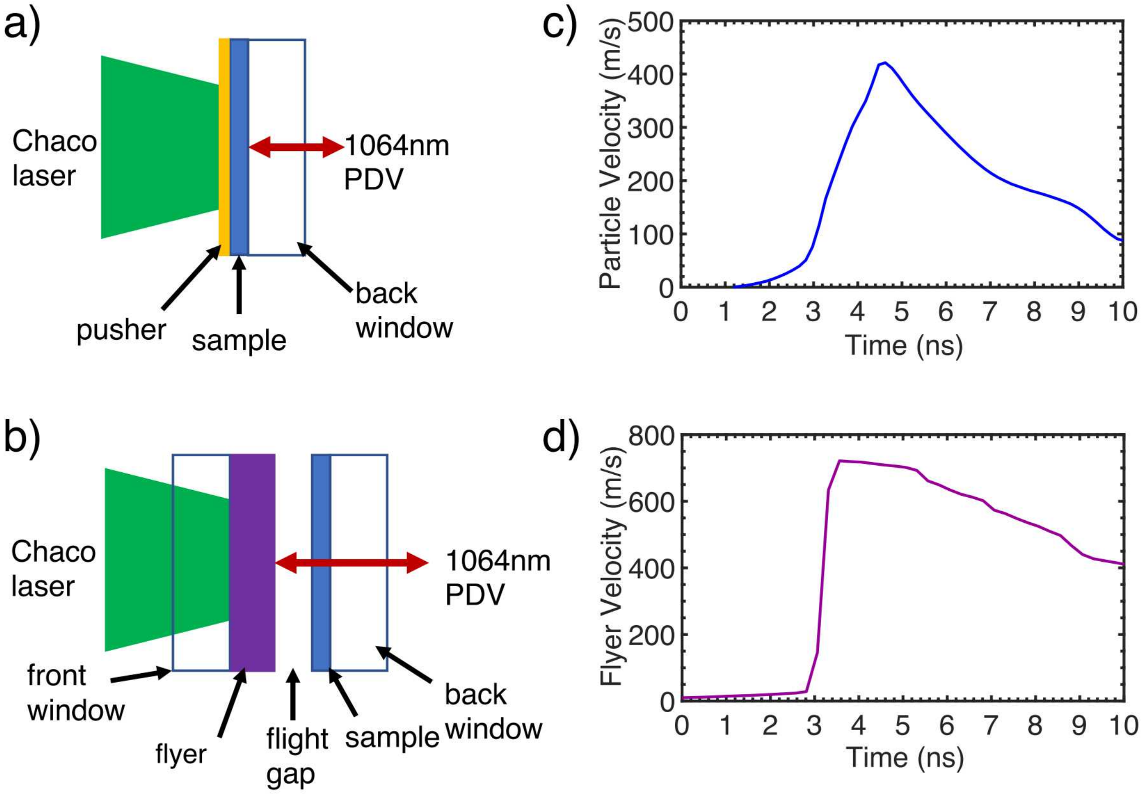

Figure 5.1. Schematic of laser compression schemes and corresponding measured velocity profiles of direct drive (a) & (c), and flyer impact (b) & (d).

In the direct drive scheme (see Fig. 5.1a), the laser is focused onto a target composed of a pusher, a sample, and a back window. The laser ablates the pusher layer causing the vaporized material to expand away from the target surface. As a result of conservation of momentum, a large ablation pressure is produced near the surface causing a compression (shock) wave to propagate into the sample material. As the shock wave passes through the sample, the transparent back window maintains the high-pressure state, which is measured by a velocimetry diagnostic.

In the flyer plate scheme (see Fig. 5.1b), the target consists of two separate components, namely a flyer part and a sample part. The laser is focused through the transparent front window and ablates the flyer material. A flyer plate is launched off the front window and propagates across a flight gap to impact a sample situated on a back window.

The Chaco laser was used in July 2016 to experimentally compare the two laser compression schemes. For the direct drive scheme, the target consisted of a composite mylar (2 μm thick) and epoxy (10 μm thick) pusher, an Al sample (25 μm thick), and a BK7 glass back window (3 mm thick). The Chaco laser (15 J of energy, 2 ns pulse duration, near-flat-top temporal profile) was focused onto the target, and the particle velocity of the Al sample at the back window interface was measured by the 1064-nm PDV system (see Fig. 5.1c). The measured peak particle velocity of 420 m/s corresponded to a shock (Hugoniot) state of 6.7 GPa in the Al sample (see Fig. 5.2). However, the high-pressure state rapidly decreases because it scales with the pulse duration of the laser.

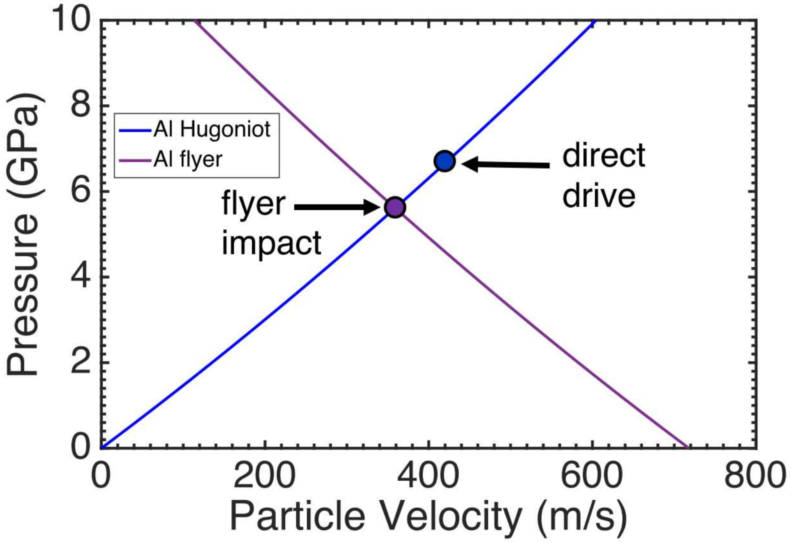

Figure 5.2. Pressure states achieved using laser compression via direct drive and flyer impact.

For the flyer impact scheme, an Al flyer (100 μm thick) glued to BK7 glass front window (3 mm thick) was examined with the Chaco laser (16 J of energy, 2 ns pulse duration). In the experiment, the sample part was not fielded. Instead, the velocity history of the Al flyer was measured directly by the 1064-nm PDV system, which had a peak flyer velocity of 720 m/s (see Fig. 5.1d). If the Al flyer were to be used to impact an Al sample, then it would produce a shock-compressed state with a particle velocity of 360 m/s and a pressure of 5.6 GPa. The flyer impact scheme generates a high-pressure state with longer duration than the direct drive scheme, but with a lower pressure trade-off.

In both cases, the pressure generated by Chaco would be enough to for example induce the γ–α solid-solid phase transition in cerium (see Sec. 4.4). For other targets, for example Al, the compression of the crystal lattice will lead to a shift of the diffraction rings to higher Θ (away from the incident x-ray beam axis). The Chaco laser was out of commission from October 2016 to July 2018, therefore we could not optimize the laser pulse for a higher pressure and/or longer hold time. When the laser came back on-line we could perform an integrated DXRD shot with ZBL (see Sec. 5.6). However, with a lower energy of only 2 J because there were still some damaged components in the system. It is planned to repair Chaco fully and continue with laser compression experiments in the future.

5.2 X-ray Source Characterization

5.2.1 X-ray line radiation from laser plasmas

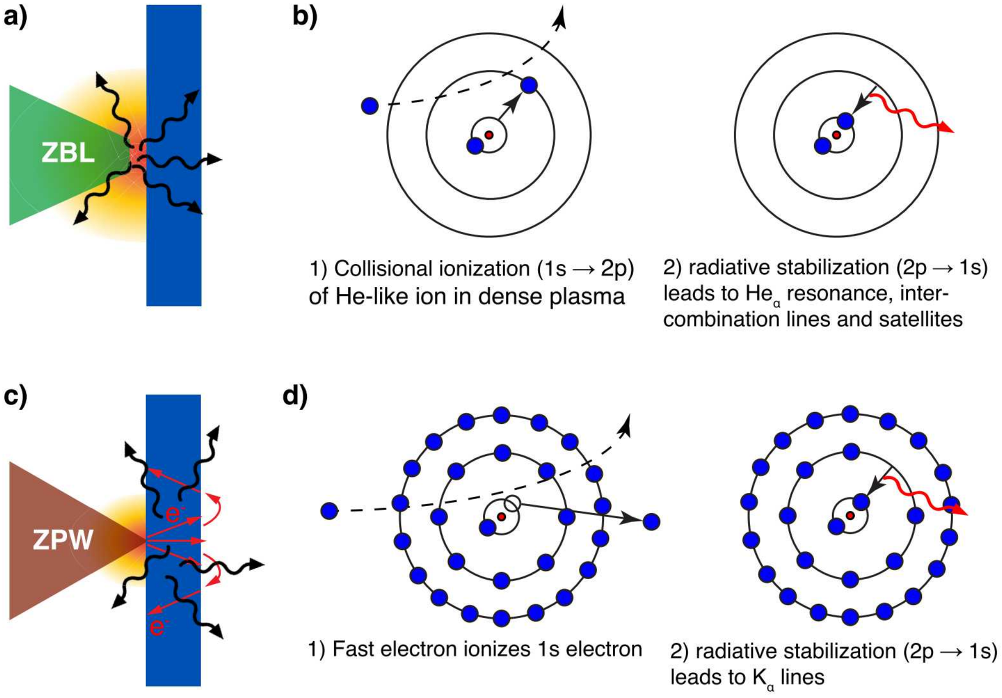

Figure 5.3. Principle of x-ray generation in laser plasmas. a) and b) show thermal He_α generation in the hot surface plasma in ns laser plasmas, c) and d) show K_α generation via fast electrons in the bulk of the material.

When an intense laser pulse is focused onto the surface of a solid it ignites a hot plasma. Details of intense laser plasma interaction have been extensively covered in the literature and will not be explained here. The most important product of this interaction for this work is the generation of brilliant x-ray line radiation, which is used here for XRD. Fig. 5.3 shows a diagram of x-ray generation with either a nanosecond ZBL (a and b) or sub-ns ZPW (c and d) laser pulse. The main difference between these two laser pulses are the pulse duration, focusability and associated intensity. The ZBL laser intensity is about 10^{15} W/cm^2, which generates a thermal ablation plasma at the irradiated target side. Temperatures of this nanosecond laser plasma are on the order of 1–2 keV [76]. This temperature, which is held over nanoseconds, leads to ionization of the target atoms to helium-like charge states. The ions emit He $_\alpha$ K-shell x-rays after collisional ionization and radiative stabilization as depicted in Fig. 5.3b. Using a low-intensity pre-pulse [77, 78] to generate a pre-plasma for enhanced absorption of the main pulse, conversion efficiencies into He-like x-ray emission are on the order of 0.1–0.5 % [79–81].

Short-pulse laser irradiation of a target also leads to a hot plasma at the target front side. However, the much higher intensity of the pulse on the order of 10^{18} W/cm^2 leads to forward-acceleration of fast electrons to MeV energies. These fast electrons are pushed into the still-cold target, which gives rise to K$_\alpha$ x-ray emission via collisional ionization followed by radiative stabilization as depicted in Fig. 5.3c and d.

For short-pulse lasers, the hot electron temperature $k_B T_e$ scales with the square root of the laser intensity (see for example [82, 83]):

$$k_B T_e = m_e c^2 \left(\sqrt{1 + a_0^2} - 1 \right). \tag{5.1}$$

Here, k_B is the Boltzmann constant, m_e is the electron rest mass, c the speed of light, and $a_0^2 = I\lambda^2/1.37 \times 10^{18}$ the normalized electric field amplitude of the laser. The intensity I in the expression for a_0 is given in W/cm^2, the wavelength λ is in μm. For $a_0 > 1$, the thermal energy exceeds the electron rest mass and relativistic effects become important. The total laser-to-hot-electron energy conversion efficiency, which determines the x-ray production efficiency, was measured as $\eta_e = 20 \pm 10\,\%$ (see [84–86] and references therein), independent of laser pulse duration from 1–10 ps at 10^{18}–10^{19} W/cm^2. Out of this energy, about 0.03-0.6 % [86] can be found in 1-3 MeV electrons.

The hot electrons, when interacting with the bulk material, generate K$_\alpha$ line radiation as well as broadband bremsstrahlung. Both radiation types were found to increase with increasing laser intensity. Furthermore, hot electron production is very sensitive to the pre-pulse and pre-plasma levels [86–89]. For example, Jarrott *et al.* [88], using the Titan laser (40 ps, 300 J, 8×10^{17} W/cm^2) at Lawrence Livermore National Laboratory, found a *decrease* in both K$_\alpha$ and bremsstrahlung yield with increasing artificial pre-pulse energy from a second laser pulse, which is accompanied by an *increase* in escaping electron number and energy with increasing pre-pulse. Measurements of the temperature and number of escaping hot electrons by Culfa *et al.* [89] at the Vulcan Petawatt laser (1 ps, 150 J, 10^{20} W/cm^2) at Rutherford Appleton Laboratory also showed that a significantly greater number of hot electrons escaped the targets when longer pre-plasmas were generated. More energy in the form of fast electrons escaping the target results in less energy from fast electrons being deposited into the target, which in turn means reduction in K$_\alpha$ signal. The escaping fast electrons not only reduce K$_\alpha$ yield, but generate bremsstrahlung background when they hit the surrounding hardware in the target chamber.

These two examples represent roughly the operating modes of ZPW at the moment (100 ps, 250 J) and planned for the future (500 fs, 500 J). The current operating parameters of ZPW are somewhat out of the ordinary for short-pulse lasers since the pulse is not fully compressed after amplification to stay within the B-integral limitations (see Sec. 3.3.1). The spectral shape and bandwidth are directly correlated to the temporal pulse shape via Fourier transformation. The incomplete pulse compression most likely leads to a substantial pre-pulse level that reduces K_α generation and may lead to a high chamber background due to escaping fast electrons.

5.2.2 X-ray spectra

Spectra are routinely acquired on each shot with a CRITR spectrometer [31]. The CRITR uses a cylindrical quartz $(10\bar{1}1)$ crystal in Cauchois geometry. The crystal focuses the x-rays in the Bragg diffraction plane onto a curved IP on the Rowland circle, which results in a high spectral resolution on the order of $E/\Delta E \approx 1000$. The instrument covers a spectral range from 7–28 keV, making it an ideal survey spectrometer for our experiments.

Fig 5.4 shows some representative spectra generated with ZBL (left column) and ZPW (right column). All spectra used a laser-micro-machined target (see Fig. 3.26); the ZBL spectra are from targets with a 500-µm diameter central disk, the ZPW spectra are from 250-µm disks. The amplitudes are shown in units of photo-stimulated luminescence (PSL), which is the native format used by the Fuji FLA-7000 scanner. PSL can be converted to photon flux, several conversions exist [90–92], but not all are in agreement with each other. The spectra were kept in PSL units, the XRD patterns shown below were converted to photons using Meadowcroft's calibration [90].

A Cu target irradiated with a 1 kJ ZBL laser pulse emits mainly He-like x-ray lines. The most dominant spectral lines are the resonance line w at 8.392 keV and the intercombination line y at 8.347 keV. The notation w and y is taken from Gabriel [93]. The peak emission is about 3.5 PSL.

Irradiating a Cu target with the ZPW laser results in mainly K_α emission lines (8.048 and 8.028 keV). He_α lines are present as well, but with much lower intensity. Note that ZPW currently is limited to 250 J. Cu spectra from targets of similar size as our 250-µm disks, irradiated by the 1 kJ Omega EP short-pulse laser system [84], show mostly He_α line emission similar to the ZBL spectrum shown in Fig. 5.4a. The relative peak brightness between a) and b) shows the ≈10× difference in conversion efficiency between long-pulse and short-pulse laser system at 8 keV.

Compared to ZBL, the ZPW laser is still efficient for generating higher energy x-ray lines. The spectrum shown in Fig. 5.4d is from a Mo target, the emission lines are the doublet K_{α_1} ($E = 17.479$ keV) and K_{α_2} ($E = 17.374$ keV), and the K_β line ($E = 19.601$ keV). For this high-Z material the front side thermal plasma does not get hot enough to ionize Mo to a He-like charge state. Note that the peak emission is almost as strong as the Cu line in Fig. 5.4b.

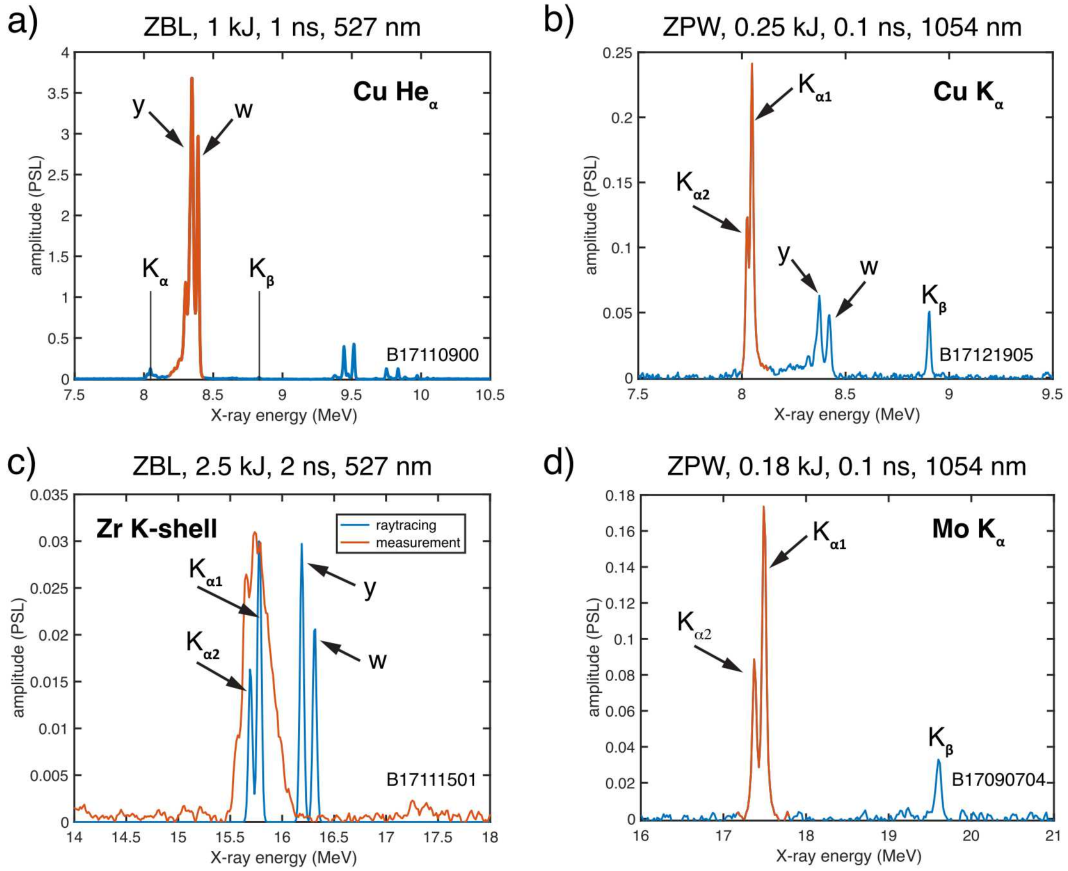

Figure 5.4. X-ray spectra generated with ZBL (left) or ZPW (right). a) The ZBL Cu spectrum shows mainly He$_\alpha$ emission lines. b) The ZPW Cu spectrum shows mainly K$_\alpha$ emission lines. For x-ray energies well above 10 keV, both lasers generate K$_\alpha$ spectra. In all spectra except c) the orange line marks the dominant emission x-ray energy range. In c) the orange line is a measurement and the blue lines mark calculated line positions.

Irradiating a high-Z target with ZBL surprisingly still generates a narrow spectral line with the expected energy. Shown in Fig. 5.4c is the spectrum generated from a Zr target. The spectral calibration for the CRITR for this spectrum was not clear because this is the only line visible on the detector. In subsequent laser shots, absorber foils were placed in front of the detector. The K edges of the foils served as calibration marks. 3D ray-tracing calculations with a custom Matlab routine were performed to compare the expected line/edge positions with the measured ones. This calibration suggests the spectral line measured bears the energy of Zr K$_\alpha$. However, the spectral shape is distorted compared to “regular” K$_\alpha$ spectra. Although with much lower temperature (few ten keV) than short-pulse lasers, nanosecond lasers also generate a population of hot electrons that can generate K$_\alpha$ emission in the cold bulk of the target. The emission peak is very low, about 0.03 PSL which is about 5× lower than the ZPW spectrum shown in Fig. 5.4d (20× lower when corrected for the laser energy difference) but relatively broad, indicating that the contained energy might be enough for an XRD experiment.

These data show that both ZBL and ZPW can be used to generate x-ray sources with fairly narrow-band emission lines that are suitable for DXRD. For low x-ray energies, ZBL generates the stronger spectrum compared to ZPW. The Cu He$_\alpha$ spectrum is broader (peak-to-peak $E/\Delta E \approx 200$) compared to the ZPW Cu spectrum ($E/\Delta E \approx 400$). For higher x-ray energies, the ZPW laser performs better, resulting in a K$_\alpha$ feature without He$_\alpha$ contamination. Surprisingly, ZBL can still be used to excite a 16 keV line feature from Zr, although with relatively poor efficiency.

5.2.3 Laser-to-x-ray energy conversion efficiency

The most important source characteristic is the total photon yield in the spectral bandwidth of interest. The yield was measured using the single photon counter diagnostic (SPC), described in Sec. 3.7. Additionally, some data points could be obtained by integrating and correlating a CRITR spectrum to SPC data. During this project, due to time constraints and other prioritizations, we could not measure conversion efficiencies for many different x-ray materials or laser parameters. However, a database of conversion efficiencies did already exist from previous measurements at 100 TW (ZPW). An efficiency scaling for ZBL was published by Larry Ruggles [80]. Data from this reference were taken but had to scaled up by about 2× to account for the higher efficiency when a pre-pulse is used [77]. Measurements of Cu He$_\alpha$ with ZBL at Chama confirmed this correction. Data points for ZBL conversion into Zr K-shell photons were obtained in this work and added to the database. ZPW data points existed from previous experiments, but were limited to pulse durations below 50 ps. Lens-based focusing, investigated for the first time in this project, requires pulses of 100 ps or longer. Our measurements with 100 ps pulses did not show a measurable difference to the already-existing data, therefore data acquired here could be added to the database without caveats.

Fig. 5.5 shows the laser-to-x-ray energy conversion efficiency into 4π for ZBL (He$_\alpha$) and ZPW (K$_\alpha$), as well as literature data for short-pulse lasers [94]. Below 10 keV x-ray energy, ZBL is superior to ZPW. Above 10 keV the ZPW laser is more efficient. Note that the data have a gap between 10 keV (from Ge) and 15 keV (from Zr) because the materials for these ‘gap’ energies do not exist in pure form as solids.

The differences in conversion efficiency between the ns ZBL and ps ZPW laser can be explained by the different interaction physics between laser and plasma. Nanosecond laser x-ray generation primarily relies on plasma temperature at the frontside, with higher-Z elements requiring a higher temperature to ionize the plasma ions to high charge states. ZBL can only heat the plasma to a few keV, hence the conversion efficiency drops sharply with increasing atomic number and corresponding x-ray energy. The ZPW short-pulse laser generates MeV-level electrons. The energy required for K$_\alpha$ excitation (≈3× the x-ray energy) is negligible compared to the kinetic energy of the electron. Hence, the conversion efficiency scales only weakly with target material. However, the conversion depends strongly on the laser intensity, as indicated by the pink and green-colored bands. The lower-efficiency data were obtained with a laser intensity near 10^{18} W/cm^2, which is below the relativistic threshold for electron acceleration (see Eq. 5.1). For significantly higher

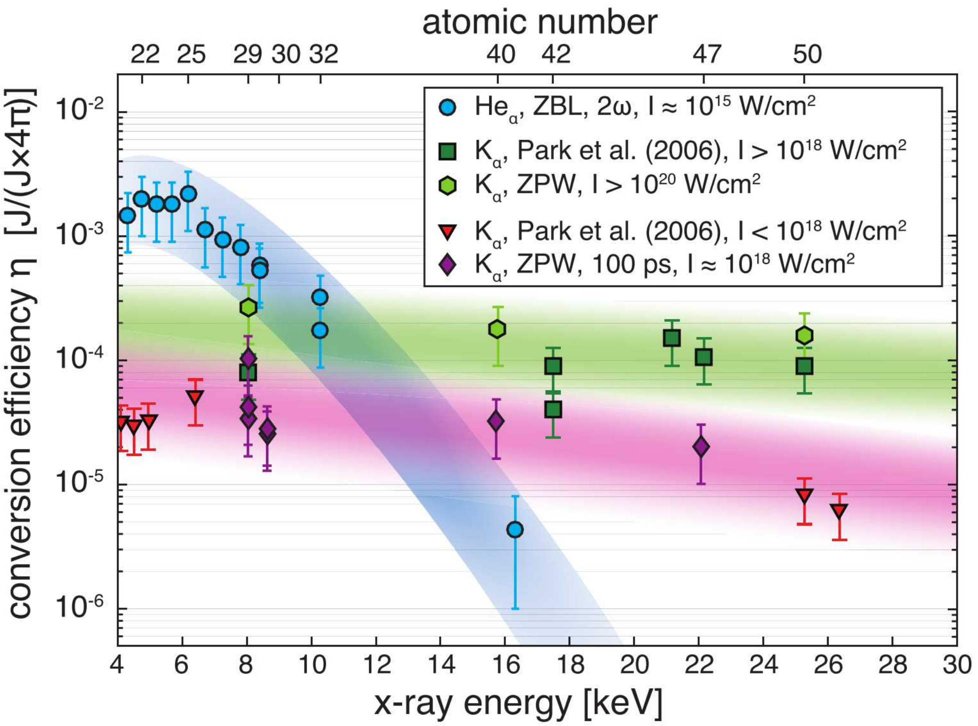

Figure 5.5. Laser-to-x-ray energy conversion efficiency η vs. x-ray energy and target atomic number for ZBL and ZPW, compared to literature data [94]. The plot shows that ns laser systems such as Sandia's ZBL laser have a much higher η for x-ray energies below about 10 keV. Above that, short-pulse laser systems offer a higher η. The short-pulse data are divided into sets for intensities near 10^{18} W/cm^2 (sub-relativistic interaction; diamonds, triangles) and above 10^{18} W/cm^2 (relativistic interaction; squares, hexagons). The shaded bands are guides to highlight the ranges.

intensities well above 10^{18} W/cm^2 the conversion efficiency is about 10× higher, but at the expense of a higher bremsstrahlung background.

Fig. 5.6 shows short-pulse laser-generated K$_\alpha$ conversion efficiency measurements vs. laser intensity for ZPW, the Titan and Callisto lasers at Lawrence Livermore National Laboratory, and Vulcan Petawatt at Rutherford Appleton Laboratory. The laser intensity was varied by modifying laser energy, pulse duration, and laser focus resulting in different laser intensities. The data points are grouped by x-ray energy (color) and pulse duration (symbols). For example, orange circles show Cu K$_\alpha$ ZPW data for short pulses (0.5-50 ps), orange diamonds are used to plot Cu K$_\alpha$ data for 100-ps pulses. The general trend of the data points shows an increase with laser intensity until $I \gtrsim 3 \times 10^{18}$ W/cm^2, above which it remains roughly flat. Above this intensity a large fraction of electrons have hundreds of keV energies, which allows the electrons to volumetrically penetrate the samples and generate K$_\alpha$ emission. Looking only at the ZPW data, there seems to be a stronger sample-Z dependency for 100-ps pulses (diamonds) than for shorter pulses (circles). However, the

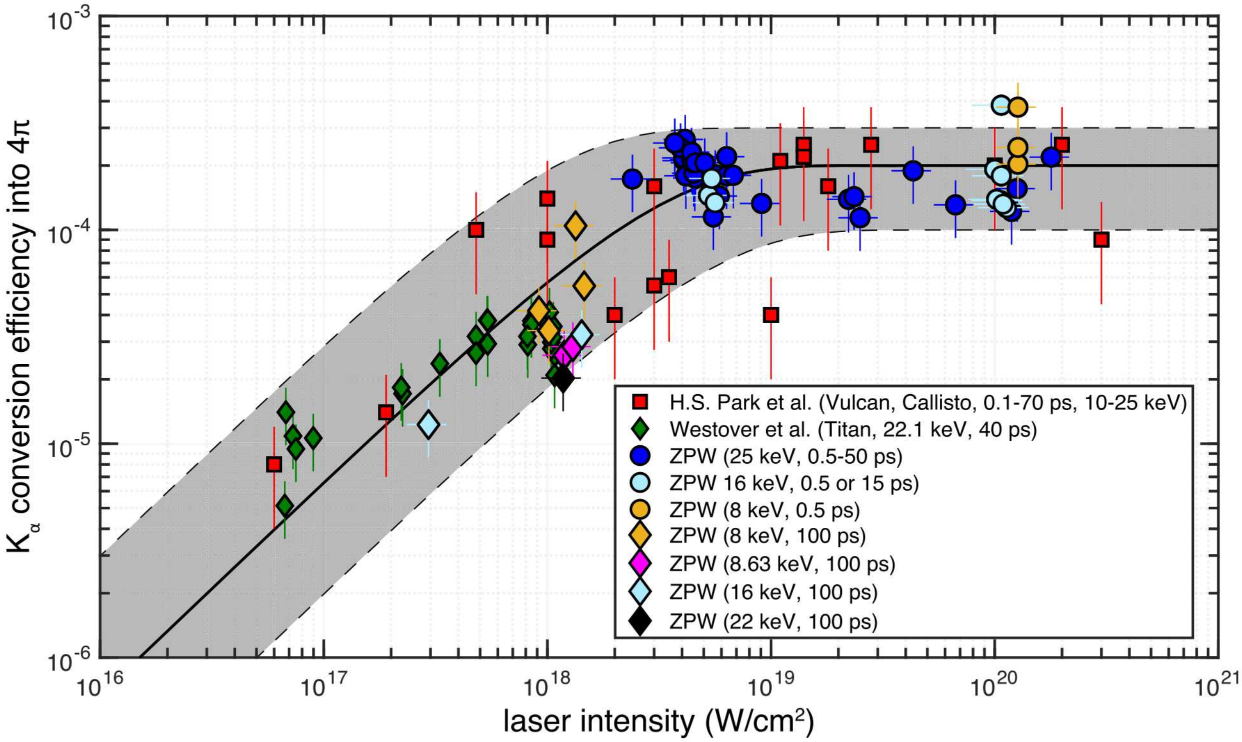

Figure 5.6. K_α conversion efficiency vs. laser intensity for ZPW for various targets and pulse durations, as well as data from Park *et al.* [94] and Westover *et al.* [64]. Diamonds are for 100 ps ZPW (lens-based), circles for 0.5-50 ps (OAP-based). The data suggest an exponential increase with laser intensity (see Eq. (5.2)) up to a few times 10^{18} W/cm^2 above which saturation occurs.

scatter in the data is too much to provide clear evidence. The data can be fitted by an empirical scaling law:

$$\eta_{K_\alpha}(I) = (2 \pm 1) \times 10^{-4} \times \left[1 - \exp\left(-\frac{I}{(3 \mp 2) \times 10^{18}\,\mathrm{W/cm^2}}\right)\right], \tag{5.2}$$

which is shown as the black lines in Fig. 5.6. Eq. (5.2) should be read such that the upper plus/minus symbol in both expressions results in the upper dashed curve, the lower symbol results in the lower dashed curve, and the average value results in the solid black curve, respectively. The data indicate that the upper limit of K_α conversion efficiency in this intensity range is about 1–3×10^{-4}. The laser intensity should be well in the saturation zone to reduce sensitivity to intensity fluctuations from shot to shot. This means the optimum laser intensity is about 5×10^{19}–10^{20} W/cm^2.

5.3 Ambient Diffraction Results

Before we started with dynamic diffraction experiments, we tested various samples and x-ray sources to experimentally verify the photometric calculations (see Sec. 4.3) and to find a source-sample configuration that yields bright diffraction rings with low background. Initial tests were done with ZPW at the 100 TW target chamber as described in Sec. 2.4. In these experiments we discovered that the laser-plasma generates a strong, high-energy background in the PACMAN and we had implement a polycapillary lens to increase the distance and to add shielding between source and sample.

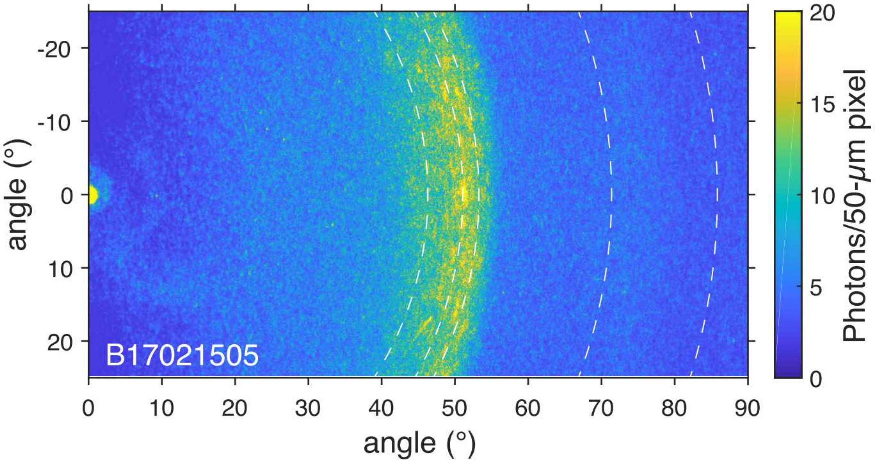

Figure 5.7. First short-pulse laser-generated powder diffraction pattern, obtained with ZPW. A Cu K_α x-ray source target and a Be sample were used. The dashed lines mark the expected line positions from Powder Cell (Sec. 4.1). The shot number B17021505 shows this was the fifth facility shot on Feb. 15, 2017.

The implementation of IfG polycapillary lens #246mls19 (see Tab.3.2) into the PACMAN as described in Sec. 3.6.2, resulted in a Cu K_α diffraction pattern from a 1.3-mm thick, 16-mm diameter Be disk oriented at 15° with respect to the surface. The image plate data are shown in Fig. 5.7. The image plate holder for this shot had a radius of 35 mm (1.38″.) The Cu K_α x-rays probe a relatively large Be volume, which leads to source broadening of the diffraction rings, reducing angular resolution. The diffraction pattern is grainy, indicating texture and larger crystallites in the sample, which is expected.

The laser energy for this shot was 118 J ±10 % in a 100-ps pulse ($I \approx 10^{18}$ W/cm^2). The Fuji MS image plate was scanned with 50 µm pixel size, the data were converted from PSL to photons per pixel using the calibration by Meadowcroft *et al.* [90] (6 mPSL/γ at 8 keV). The background is about (6 ± 1) photons per pixel, the peak signal level is about (8 ± 3) photons/pixel above background. This compares well to the photometric calculations discussed in Sec. 4.3, which result in (6 ± 3) photons/pixel. The largest known errors are from the laser energy (±10 %) and conversion efficiency (±30 %), the throughput error of the polycapillary is unknown.

While this result is very encouraging, it confirms that the photon flux in these experiments is very low and that detector background is a big issue for short-pulse laser experiments with ZPW. Experiments have started to characterize the background further and develop mitigation methods (see Sec .5.4), which will be a multi-year effort. For this reason we investigated XRD with the ZBL laser, particularly to find out if ZBL could be used for 16-keV XRD as a workaround until the ZPW source is available.

5.3.1 8 keV Diffraction on Be Samples

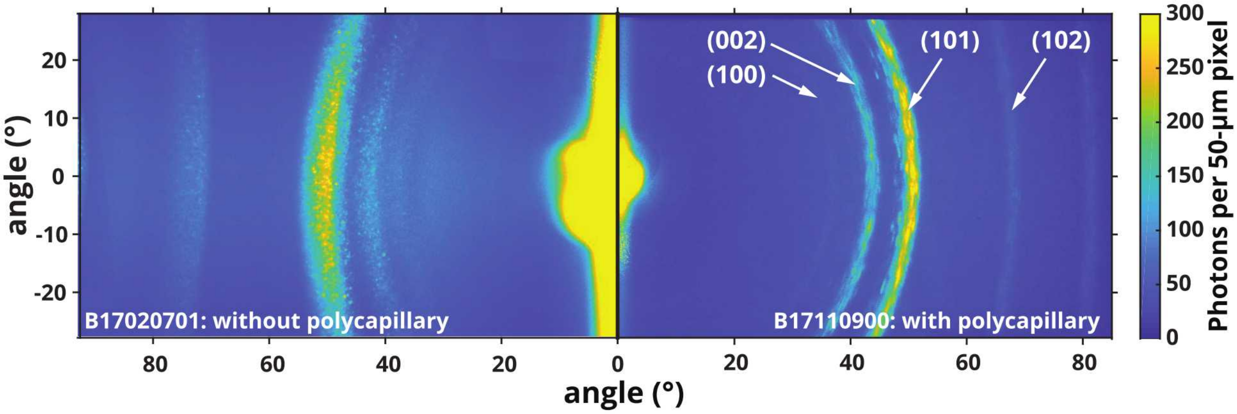

Figure 5.8. Static 8.4 keV Be XRD data obtained with ZBL, with and without polycapillary lens. The arrows denote Miller indices (hkl) associated with the crystal plane for the specific rings.

To compare XRD signal levels with and without polycapillary lens, experiments were performed with a Cu x-ray source and a thick Be sample, which has the highest scatter fraction of the materials investigated here. Fig. 5.8 shows diffraction rings from the same 1.3-mm thick, 16-mm diameter Be disk as used in the previous section, irradiated with 8.4 keV (Cu He_α) x-rays generated by ZBL in a 1.1 kJ, 1 ns laser pulse. The left side of the figure shows the XRD pattern obtained without polycapillary, using a 1-mm diameter pinhole collimator in about 1.2-inch (30 mm) distance. The x-rays irradiated the Be disk at 15° with respect to the surface. The IP detector for this shot had a shorter radius of 4 cm instead of the standard 6 cm. The brightest ring has about 300 photons per pixel above background, which is in line with our photometric calculations of $N_{\mathrm{ph,detector}} = 400 \pm 200$ photons per pixel. The background level is about 100–150 photons/px.

The right side of Fig. 5.8 shows the same diffraction pattern when polycapillary lens #246mls19 is used. The ZBL laser pulse energy was low on this shot, about 730 J. The lens allows for a larger dispersion using the 6-cm IP and a rotation of the Be disk to normal incidence, both of which increase resolution, while maintaining similar photon counts. Grain size effects become more visible in the XRD pattern (irregular brightness along a ring), and fainter rings can be detected. The brightest ring has about 200 photons per pixel above background. The background level is about 40 photons per pixel, which is 2.5 to 4 times lower than with pinhole collimator but not zero. In addition to fluorescence of the sample, some background radiation was likely entering the PACMAN through the gap between polycapillary exit and PACMAN front (see Fig. 3.25). The expected signal level using a 5×10^{-4} conversion efficiency and scatter fraction $F = 0.03$ is $N_{\mathrm{ph,detector}} = 100 \pm 50$ photons/pixel, which is close to the measured data.

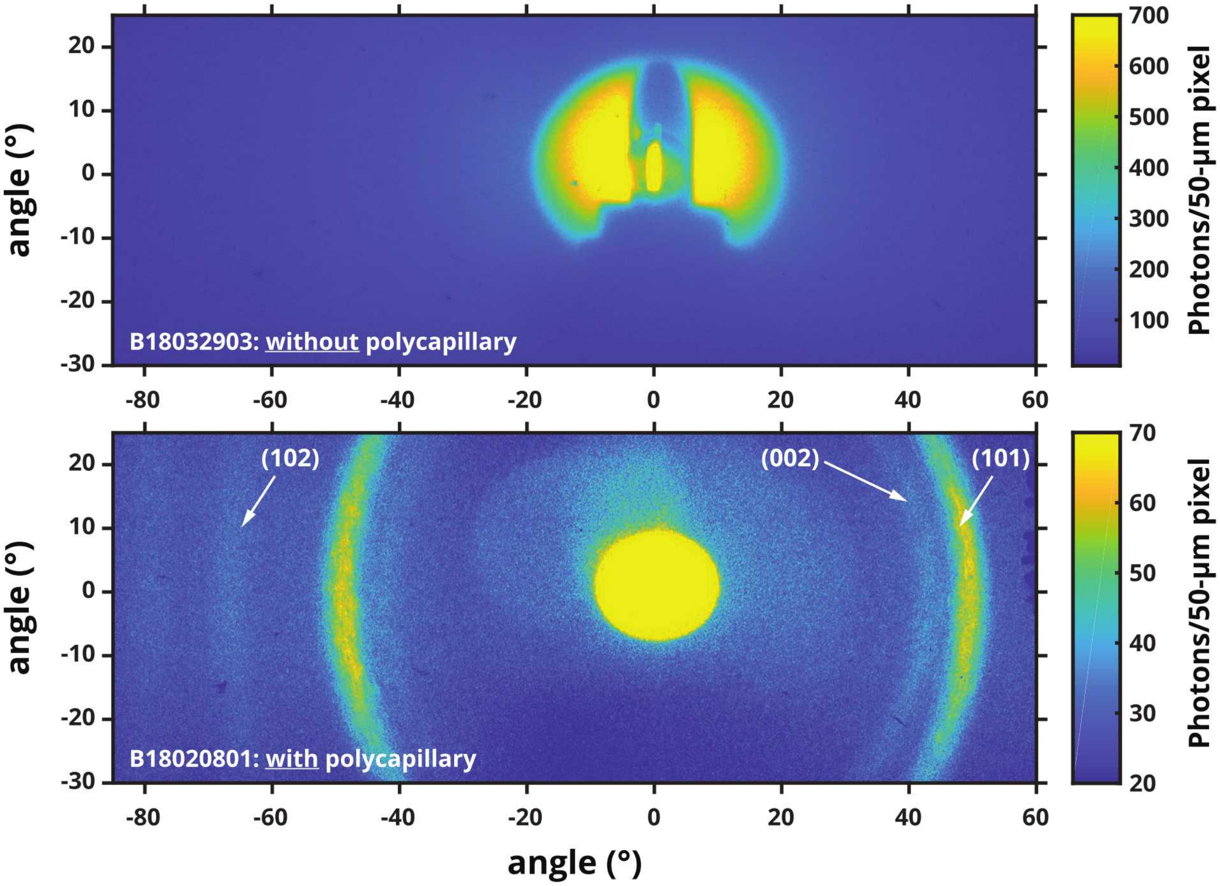

Figure 5.9. Static 8 keV Be XRD data obtained with ZPW, a Cu target and Be sample. Without the polycapillary lens (top), the strong background creates a radiography image instead of an XRD pattern. Use of the polycapillary lens (bottom) enables detection of the XRD pattern. The arrows denote Miller indices (*hkl*) associated with the crystal plane for the specific rings.

In stark contrast to the ZBL results, XRD with ZPW using a Cu K_α x-ray source suffers from a lower conversion efficiency, lower laser energy and a much higher background level. Fig. 5.9 shows image plate data for a shot with pinhole collimator (top) and with XOS #8968 (bottom). The laser energy for the pinhole shot was 230 J ±10 %. A 1.5-mm × 0.5-mm, 1.5-mm thick WCu slot collimator was used, the target-to-pinhole distance was ≈2 inches (50 mm), the target-to-sample distance was 105 mm. Additional layers of Al shielding with central 12.7-mm holes were installed in front of the PACMAN to reduce hot electron background. The Be sample surface was oriented at an angle of 15° with respect to the incoming x-ray beam to increase the scatter fraction. Nonetheless, the result is a radiography image of the target instead of a diffraction pattern. The general background at large angles is about 100 photons/pixel. Towards the center, the bright yellow circle is the projection of the hole in the Al shielding. The rectangular shadow at the bottom of the circle is from the sample holder. The shadow of the Be disk is on top. The bright elongated spot at the center is the pinhole slot image.

The lower image of Fig. 5.9 shows that the polycapillary lens enables the detection of a diffraction pattern that is comparable to Fig. 5.8, left image, but with about four times less laser energy. The ZPW laser delivered 226 J ±10 % for this shot. The polycapillary increases the distance between source and sample to 174 mm. Additional shielding layers are installed, which further reduces the background. Fig. 3.28 shows a photo of PACMAN (without lid) before it was installed at Chama. The central area of the image plate shown in Fig. 5.9 is still swamped by background, but the background at higher angles is low enough to see the diffraction pattern. The brightest diffraction ring is 40±5 photons per pixel above the 30 phot./px. background. Assuming a conversion efficiency of $4 \times 10^{-5} \pm 30\,\%$, scatter fraction $F = 0.12$, and polycapillary throughput $T = 6 \times 10^{-4}$, the expected ring brightness is $N_{\mathrm{ph,detector}} = 30 \pm 10$, which matches the measurement.

5.3.2 16 keV Diffraction on Zr Samples

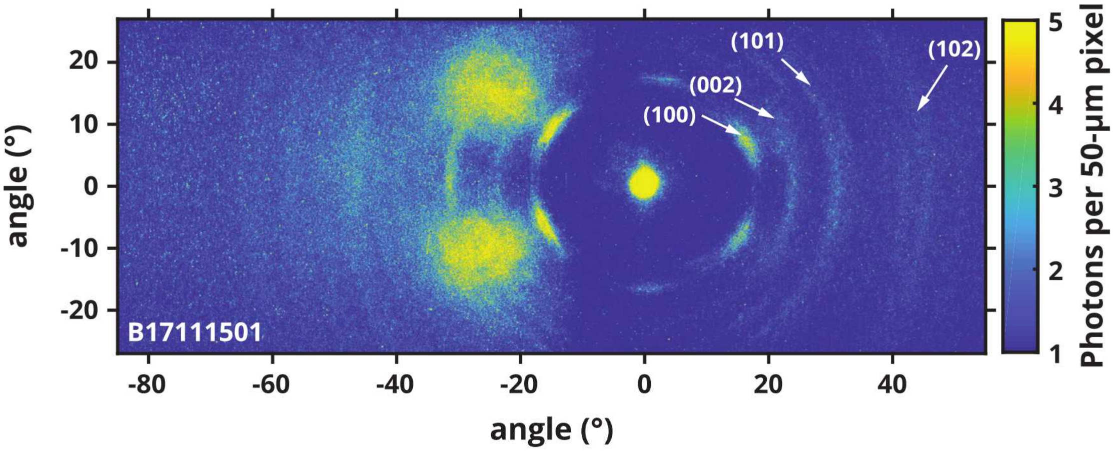

Figure 5.10. Static 16 keV XRD pattern from Zr, obtained with ZBL. The arrows denote Miller indices (hkl) associated with the crystal plane for the specific rings.

Because of the encouraging Zr K-shell spectrum generated with ZBL in test shots in March/April 2017, an experimental campaign was performed in November 2017 with the goal to find out if ZBL—in combination with polycapillary lens IfG #246mls19—could be used to generate a 16-keV

XRD pattern. Fig. 5.10 shows the XRD pattern for a 25-µm Zr sample using 16 keV x-rays from a Zr target irradiated with ZBL. Fig. 5.4c shows the x-ray spectrum measured with the CRITR. The laser energy for this shot was 2486 J ±10 % in a 2 ns pulse. The two large lobes at about -20° in Fig. 5.10 may stem from unfiltered broadband thermal radiation passing through the polycapillary lens and subsequently diffracting from the Zr sample. This hypothesis is supported by the pattern on the right side of the image, where these lobes are absent. X-rays hitting this side of the detector had to pass through the 25 µm Zr foil, which acts as a high pass filter. We are investigating mitigation methods for this unwanted signal in future experiments.

Assuming a conversion efficiency of $(5 \pm 3) \times 10^{-6}$, scatter fraction $F = 0.062$, and polycapillary throughput $T = 3 \times 10^{-5}$, only $\approx 10^8$ photons irradiate the sample and the expected ring brightness is $N_{\mathrm{ph,detector}} = 0.5 \pm 0.4$ photons per 50-µm pixel. The measured diffraction rings are highly structured, indicating strong preferred orientation in the sample. The signal in the bright 'islands' marked by (100) is about 4 photons per pixel. The background is about 1 photon/pixel. An angular average yields about 0.5 photons per pixel, which is again very close to the calculated data.
This measurement demonstrates that ZBL can indeed be used for 16-keV XRD, with an image plate detector in a distance equivalent to 0.1° angular resolution, if the detector background can be kept close to zero. If the angular resolution requirement can be relaxed and the detector moved closer to the sample, the signal can be increased accordingly. Further measurements and dynamic XRD shots are planned for the future.

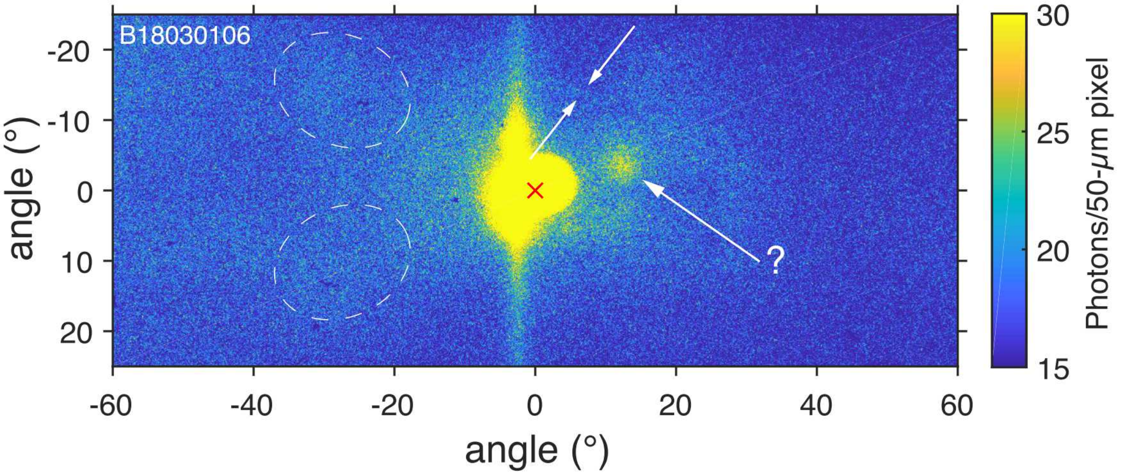

Figure 5.11. Static 16 keV XRD pattern from Zr, obtained with ZPW. The red cross marks the axis of the x-ray beam, the white ellipses and arrows mark a potential signal.

Finally, Fig. 5.11 shows the image plate result for a 25-µm Zr sample, when ZPW is used to create the Zr x-ray source. We used polycapillary lens XOS #8968, which is about five times more efficient at 15.7 keV than IfG #246mls19 used with ZBL. This efficiency enhancement was confirmed by performing ZPW XRD shots using Cu targets and a Be sample (shots B17102507 and B18020801). ZPW delivered 250 J in a 100-ps pulse to the laser target. The 16-keV conversion efficiency for ZPW is about 10× higher than for ZBL, but the laser energy is ten times lower. Because of the more efficient polycapillary lens the expected signal is about five times brighter than the ZBL signal: ≈ 2.5 phot./px. on average, and 20 phot./px. in the bright spots.

No clear diffraction lines are visible. The round feature marked with "?" occurred in other high-Z target shots as well, its origin is so far unknown. The white ellipses mark areas where the signal is slightly higher than the background, similar to the lobes in Fig. 5.10. The white arrows mark a location that could indicate fragments of a ring. However, the data are too noisy to provide evidence of an XRD pattern. The next section describes experiments and simulations that were performed to better understand the origin of the background and to develop mitigation methods.

5.4 ZPW Background Evaluations

Experiments were performed to investigate the nature, directionality and origin of the background. Image plates were placed at the bottom and top lids as well as at the front shield inside the PACMAN. The cylindrical IP was equipped with a Ta step wedge (10 mm wide × 50 mm long, 10 steps from 0.4 mm to 2 mm) and other low/high-Z absorber foils in order to determine the spectrum. In a series of experiments, additional shielding was placed in front of PACMAN or around the source to determine if the background inside PACMAN could be reduced.

Fig. 5.12 shows photographs of the various blocking efforts being tested. The PACMAN was placed at the same distance from the laser target as is needed for polycapillary lens operation. In most of the shots the laser target was a laser micro-machined Cu target. Some shots were performed with a Mo target to evaluate a potential target-Z dependency of the background (i.e., target bremsstrahlung). Starting from the top left of Fig. 5.12, 1-inch thick W bricks with an additional inch of acetal homopolymer plastic (Delrin, $(CH_2O)_n$, 1.4 g/cm^3) were put in front of PACMAN to slow down electrons emitted from the target and to reduce bremsstrahlung. To reduce the entire Chama chamber background, a source enclosure was designed that surrounded the laser target with 1.5 inch of WCu (90/10) in all directions except for the laser entrance and through-focus imaging cones (top center). The enclosure has a removable plug towards the PACMAN to open a line-of-sight (LOS). In shots with open LOS, additional graded-Z shielding plates (high-density polyethylene $(C_2H_4)_n$, 0.95 g/cm^3, Al, brass, each 0.25 inch (6.35 mm) thick) were put in front of PACMAN, again to slow down electrons before they reach the WCu PACMAN front shield.

Laser shots with polycapillary lenses utilized graded-Z shielding plates equipped with a LOS hole, shown on the bottom left, a 3d-printed plastic enclosure that surrounded that target with 0.5 inch ABS-like plastic (acrylonitrile butadiene styrene, $(C_{15}H_{17}N)_n$), Formlabs Resin, 1.2 g/cm^3), shown on the bottom center, or an open target with 1″ W bricks on either side of the polycapillary and a brass x-ray beam tube as shown on the bottom right.

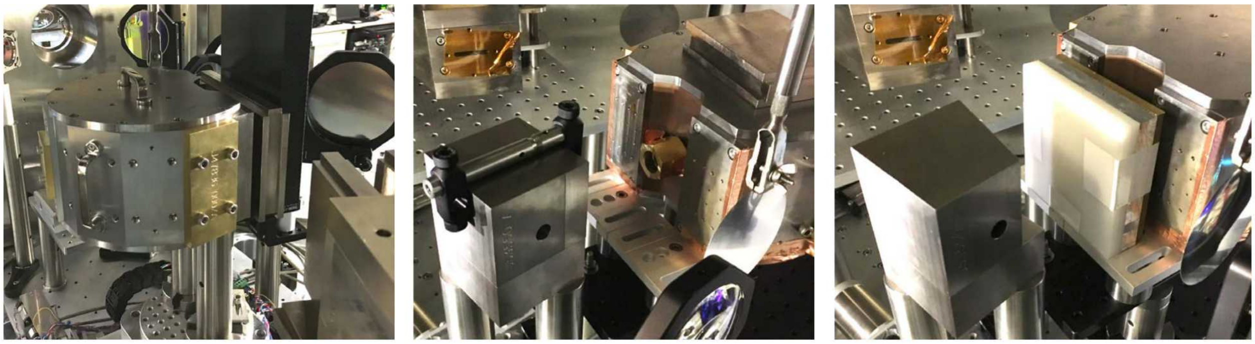

1” W and 1” Delrin plastic

1.5” WCu enclosure, LOS closed

1.5” WCu enclosure, LOS open, graded-Z plates

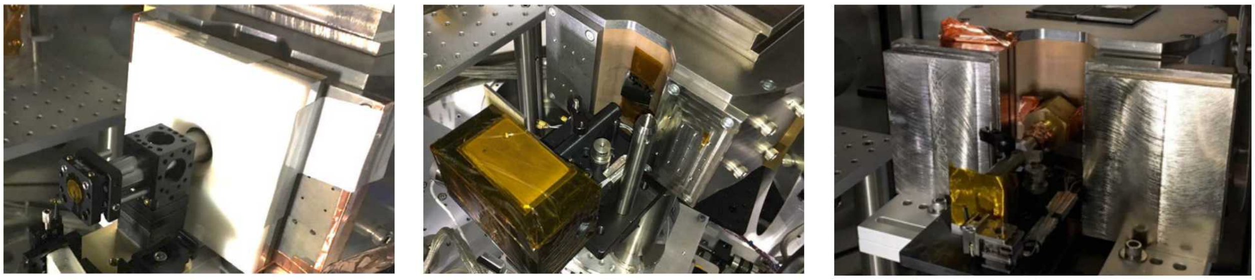

Polycapillary lens and graded-Z plates

3d-printed plastic enclosure

Polycapillary lens, 1” W bricks, brass tube

Figure 5.12. PACMAN line-of-sight shielding efforts. The top row shows shielding efforts used to reduce the PACMAN background close to zero. The bottom row shows shielding efforts in combination with a polycapillary lens.

Without any additional shields, using a Cu target in a 250-J ZPW shot, the baseline background on the cylindrical IP inside PACMAN is 0.7 PSL. The Ta step wedge in front of the cylindrical image plate created a blurry shadow with poor contrast, indicative of a large area, high energy source. The top/bottom image plates showed enhanced signal in locations of inside and outside screw holes, indicating that signal was entering the PACMAN through the lids and side walls. Consequently, all tapped holes were closed with screws. W plates were put on top of/below the PACMAN. Signal entering the PACMAN through the lid and side walls indicates that background is generated from secondary sources, such as the chamber walls and mounting hardware inside Chama.

Tab. 5.1 summarizes the results of the additional shielding efforts. The greatest background reduction could be achieved by the closed WCu enclosure with LOS plug (top center in Fig. 5.12). Here, the IP signal was 35× reduced compared to no additional shielding. Opening the WCu enclosure but adding graded-Z plates to the PACMAN front to keep the LOS closed results in background increase by 2.5× compared to the full enclosure. Without the graded-Z plates, the signal increases by additional 40 % and the background reduction is 10× compared to no shielding.

Removing the source enclosure and putting a similar thickness of W (plus plastic) in front of PACMAN results in a similar signal as the open enclosure with graded-Z plates. This shows that

Table 5.1. Comparison of PACMAN shielding efforts for ZPW Cu laser targets. See text for details.

Method	LOS open?	PSL value	Background decrease
No additional shields	Yes	0.7	1×
WCu enclosure w/plug	No	0.02	35×
Open WCu encl., graded-Z plates	No	0.05	14×
Open WCu encl.	Yes	0.07	10×
1″ W, 1″ plastic	No	0.05	14×
1″ W, 1″ plastic, gap in W	Yes	0.09	8×
Polycap., plastic enclosure	Yes	0.25	3×
Polycap., 1″ W, beam tube	Yes	0.08	9×
Polycap., graded Z	Yes	0.15	5×

the graded-Z plates are equally (in-)efficient in shielding the LOS than 1″ of tungsten, which is an indication of MeV-scale bremsstrahlung since the absorption length of most materials is very similar [95, Fig. 33.19] around 1 MeV. Slightly worse shielding (7.8×) was obtained by moving the 1-in. W bricks apart to open the PACMAN LOS but keeping the Delrin plate. This shows that the background is not entering through the PACMAN entrance hole but is caused by large-area irradiation of the tungsten front. These results are encouraging, showing that in principle the background inside PACMAN can be reduced significantly.

Next we tested if and how the background could be reduced when a polycapillary lens was used. Due to time constraints the WCu enclosure was not designed to be compatible with a polycapillary lens. A 3d-printed plastic enclosure was designed that is compatible with the polycapillary and tested in a few shots. The plastic enclosure was not very efficient as it reduced the background only 3× compared to shots without any shielding. Next, we removed the plastic enclosure and added two 1″ W bricks to the PACMAN front on either side of the polycapillary axis. The gap between polycapillary exit and PACMAN entrance hole was closed with a brass tube (bottom-right photo in Fig. 5.12). This shielding reduced the signal to the same level as the “W + plastic with gap” shots, which means the majority of shielding was obtained by adding the W bricks. It should be noted that the brass beam tube was required to obtain low background. Without it, the background was about 0.5 PSL, close to the unshielded case. At this time we realized the PACMAN, due to its modified use with a polycapillary, had some gaps in the front tungsten shield and two WCu (90/10) wedges were designed to fill these gaps (see Sec. 3.5.3) and to replace the front tungsten bricks. The gap between polycapillary exit and PACMAN front was closed by installing graded-Z shields. While the background reduction was 5×, these measures were not as efficient as using the 1-inch W bricks. These results support the hypothesis that the majority of background signal stems from direct exposure such as MeV-scale electrons or bremsstrahlung emitted by the laser source, and not from secondary sources such as the chamber walls or mounting hardware inside Chama. A thick, at least 2 inch, high-Z shielding in combination with a narrow x-ray beam tube behind the polycapillary lens is required to reduce the background enough for XRD experiments.

In addition to the PACMAN shielding efforts, image plates were sandwiched between two 1 inch thick W bricks ("W sandwich") and placed at different locations/distances inside Chama to measure directionality of the background. The front side of the CRITR spectrometer was blocked in a few shots to measure the signal inside this 1-inch thick stainless steel enclosure near the chamber wall. Image plates were also placed outside the Chama chamber at the door, facing the inside, to test if 4 inches of stainless steel can reduce the signal, and at the laser entrance window for the Chaco laser to test if a large distance reduces the signal. A makeshift particle spectrometer was built using a 0.25 inch diameter, 3 inch long stainless steel collimator, $2'' \times 2''$dipole magnet and a shielded IP enclosure.

When the magnet of the particle spectrometer was removed, the IP was heavily overexposed. After 23 scans a strong central spot with fuzzy halo became visible. With the magnet, the IP was only scanned 10 times before it was no longer overexposed. The central spot had no fuzzy halo, but the region of maximum brightness shifted due to deflection of charged particles in the B-field. Particle tracking simulations were performed, which indicated the signal originates from positively charged MeV-scale ions, for example from protons from hydrocarbon layers at the front side. It is well-known that protons can be accelerated to MeV-energies using short-pulse lasers with pulse durations of 10 ps or less. ZPW is set up for 100-ps pulses, the strength and magnitude of this ion signal was not expected.

The W sandwich measurements indicate that the background signal does not significantly change with distance from target. However, results using different shielding boxes (W sandwich vs. CRITR stainless steel box vs. outside of Chama) indicate that shielding material and thickness may be more important than distance. It was observed that the background does not scale significantly with target material or target thickness, but it depends on the target orientation with respect to the laser and PACMAN.

Lowering the laser intensity will lower the hot electron temperature $k_B T_e$ (see Eq. (5.1)), which will lower the background (and the signal) because it is caused directly or indirectly by the laser-accelerated electrons. Lowering the laser intensity can be achieved by defocusing or temporally stretching the pulse. This was done by Maddox *et al.* [13] to measure Bragg diffraction of laser-generated 17.4 keV x-rays off single crystals at the Omega EP laser facility. The 1 kJ, 200 ps EP laser was used with a nominal intensity of 3×10^{16} W/cm^2. The authors state that this intensity was determined experimentally and provided a high K_α/bremsstrahlung ratio. We have performed a shot with a de-focused laser pulse that lowered the intensity about ten times, however the K_α spectrum measured by the reliable CRITR spectrometer was significantly lower, too low for powder XRD in our configuration.

5.5 Monte Carlo Simulations

Due to the difficulty of directly measuring the background in the chamber and experimentally determining the resulting shielding requirements, we utilized Geant4, a Monte-Carlo particle physics code, to assess the radiation environment and associated shielding options. While Geant4 supports a wide range of particles and physics models [96], [97], these simulations were driven primarily by the EPDL97 data originally developed at Livermore National Laboratory [98].

5.5.1 Thick-target simulations

The initial goal was to ballpark required shielding thicknesses for different materials and radiation environments. The geometry for these simulations is summarized in Figure 5.13a. The materials chosen were lead (common reference), polyethylene (PE, cheap and light, low-Z to stop electrons), stainless steel (SS304, reference for PACMAN body), aluminum (common lightweight shield material), tungsten (high density, safe) and tungsten-copper 70/30 (used in PACMAN). The source term is a 1D beam of electrons with a Maxwell-Boltzmann electron energy distribution, approximating the laser-plasma in the chamber:

$$\frac{df(E_e)}{dE_e} = 2\sqrt{\frac{E_e}{\pi}}\left(\frac{1}{k_B T_e}\right)^{3/2} \exp\left(\frac{-E_e}{k_B T_e}\right). \tag{5.3}$$

Since the exact temperature $k_B T_e$ of the source is unclear, we ran simulations with temperatures of 0.5, 1.0, 1.5, and 2.0 MeV. Using the ponderomotive scaling from Eq. (5.1), this range of energies corresponds to laser intensities from about 4×10^{18} W/cm^2 to 3×10^{19} W/cm^2. $df(E_e)/dE_e$ was discretized in 10 keV bins and truncated at 10.24 MeV. This source was directed into a semi-infinite slab of a shielding material.

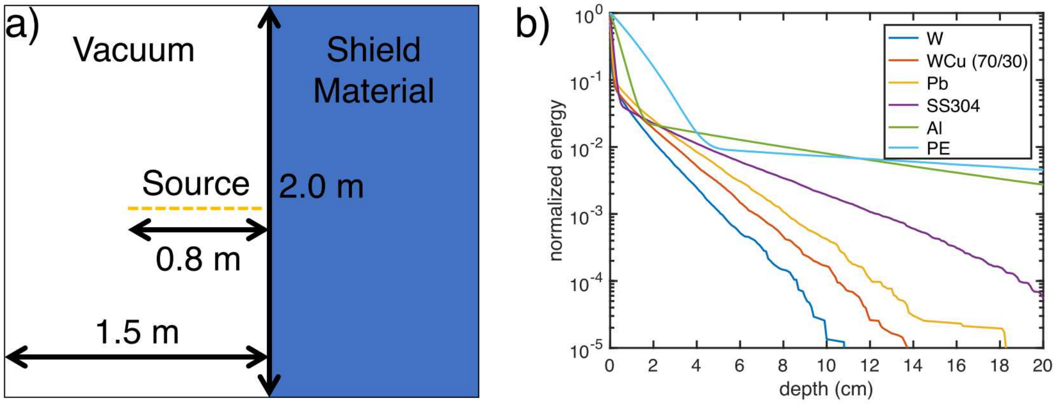

Figure 5.13. Shielding thicknesses for different materials. a) The geometry for the thick slab simulations. b) Normalized energy E/E_0 vs. depth using a 2 MeV thermal electron source. The energy deposition includes energy from the electrons as well as from secondary products such as bremsstrahlung.

The simulation tracked energy deposition vs. depth in the slab (see Fig. 5.13b), along with the fraction F_r of the source energy that was reflected from the slab. For each temperature-shield material pair, we then calculated the shielding thickness required to stop the electrons (Δx) and the thickness of shielding required to attenuate the secondary bremsstrahlung by a factor of 10 (μ_{10}). The results are summarized in Table 5.2. The data for Δx were consistent with NIST attenuation data for electron stopping [99].

As expected, high-Z materials shield electrons and bremsstrahlung much better than low-Z materials. High-Z materials are also more reflective, which is beneficial on shielding near the target (e.g., around the PACMAN). Furthermore, while high-Z materials (Pb, W) are able to stop all electrons within less than 1 mm, secondary products are able to penetrate several cm in our worst case simulation of 2 MeV temperature (see Fig. 5.13b) with only about 100 to 1000× attenuation. This means, if for example the 250-J ZPW electron conversion efficiency into MeV electrons is on the order of 0.05-0.5 % [86] (0.1-1 J), 1-10 mJ of energy is able to penetrate more than 25 mm (1 inch) of tungsten.

Table 5.2. Simulated energy deposition vs. depth results. For each material the thickness of shielding required to attenuate the secondary bremsstrahlung by a factor of 10 (μ_{10}), the fraction of the energy reflected (F_r), and the shielding thickness required to stop the electrons (Δx) are shown. WCu is a tungsten-copper alloy, the numbers in brackets denote the weight percent.

E_{kin} [MeV]	μ_{10} [cm]	F_r	Δx [mm]	μ_{10} [cm]	F_r	Δx [mm]
		polyethylene			lead	
0.5	35.7	0.01	18	3.0	0.31	< 0.5
1.0	37.8	0.01	33	4.2	0.26	< 0.5
1.5	53.2	0.02	40	4.3	0.24	< 0.5
2.0	57.5	0.06	48	4.4	0.24	1
		graphite			WCu (70/30)	
0.5	16.8	0.01	10	2.9	0.25	< 0.5
1.0	26.7	0.01	18	3.2	0.20	< 0.5
1.5	33.0	0.02	22	3.5	0.18	< 0.5
2.0	35.8	0.06	48	4.4	0.24	1
		aluminum			WCu (90/10)	
0.5	13.6	0.04	4	1.9	0.28	< 0.5
1.0	17.2	0.03	10	2.8	0.23	< 0.5
1.5	21.7	0.04	13	2.9	0.20	< 0.5
2.0	27.2	0.07	17	3.4	0.21	< 0.5

5.5.2 Chama chamber

The next step was to simulate a simplified version of the Chama chamber. The chamber was approximated as a cylinder with a 75 cm inner radius and 76 cm interior height. The walls were 4 inch thick stainless steel. The simulated chamber was empty other than the PACMAN unit. The simulation geometry is shown in Figure 5.14. The source term was an isotropic point source of Maxwell-Boltzmann thermal electrons. A cylindrical deposition counter with 6 cm radius and 6 cm height was placed in the center of PACMAN. Particles entering the cylinder are stopped, the final particle energy is added to the deposited energy entering PACMAN. The simulation tracked the total energy that reached the interior of the PACMAN enclosure as a proxy for the background noise on the experiment. Note that these measurements are comparative, not absolute since the absolute energy release is unknown.

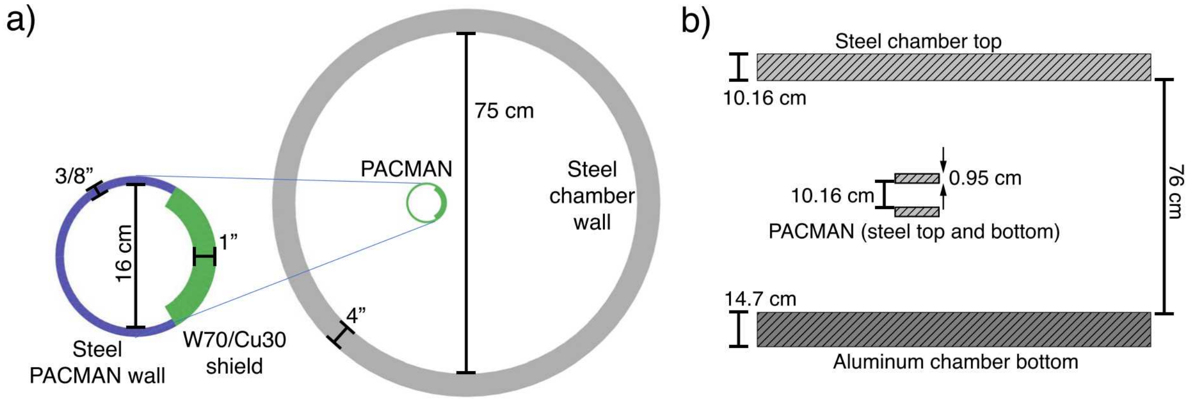

Figure 5.14. Chama chamber as simulated in Geant4. a) Shows the top view of the chamber geometry with PACMAN. b) Shows a cross-sectional view.

Multiple simulations were performed to track where the deposited energy in PACMAN originates. Repeated simulations were performed with geometry components "blacked out" (stopping particles), such as the chamber top, the chamber bottom, the chamber wall, or directly deposited in PACMAN without reflecting off something else. We then compared the tally to the base value. The difference is the fraction passing through a filtered component. This indicates where shielding will be most effective.

Direct exposure through the front shield was found to be the dominant contributor, as shown in Table 5.3, providing further evidence that hot electron bombardment from the source is the root cause of the background and not bremsstrahlung or electron reflection from other objects inside the chamber. This result suggests that enhancement of the front shield should be the main optimization goal. Reducing top and bottom scatter in the PACMAN enclosure is a secondary goal, whereas the contributions from the chamber wall, top and bottom are of lower concern.

Table 5.3. The percentage of energy deposited in PACMAN, which first deflected off each chamber component. Note that these are not exclusive, and consequently do not sum to 100%. This is because an electron could, for example, deflect inside the chamber wall, pass through the PACMAN lid, and deposit inside the PACMAN enclosure. In this case it would contribute to the tally from both the chamber wall and the PACMAN enclosure top/bottom.

Component	**Percentage of Total Deposition**
PACMAN Front Shield	92
Chamber Top and Bottom	6
PACMAN Enclosure Top and Bottom	10
Chamber Wall	2
PACMAN Wall	3

After having confirmed that the majority of the PACMAN signal is from electron bombardment of the front shield, we investigated the scaling of the front shield efficiency and material vs. source temperature. Simulations of an electron beam with $N = 10^6$ ($N = 10^8$ for temperatures below 0.5 MeV for better statistics) primary electrons impacting a 1-in. thick WCu (70/30) or Al plate were performed. The electron energy distribution was set up according to Eq. (5.3). As in the previous simulations, a detector counted the energy E_{dep} deposited behind the WCu plate.

Fig. 5.15 shows the scaling of the fraction $E_{\mathrm{dep}}/E_{\mathrm{tot}}$ versus source electron temperature $k_B T_e$. The total energy is $E_{\mathrm{tot}} = \frac{3}{2} N k_B T_e$. As expected from the electron stopping simulations above, the source temperature dramatically impacts the energy deposition behind the plate. For example, increasing the electron temperature over two orders of magnitude from 0.1 to 10 MeV increases the transmission by about 10^5. The shielding difference of the two plate materials is most important for low temperatures. This appears counterintuitive, but can be explained by the difference in transmission between the materials. At low temperatures, where most of the electrons have low energies, the WCu shields very efficiently. Near 1 MeV the difference between the two materials is the smallest, simply because almost all materials exhibit a minimum in their photon attenuation efficient [99]. The Al data points jump higher for $k_B T_e \gtrsim 5$ MeV; here the material thickness is insufficient to stop all electrons and a large fraction of high-energy electrons can escape at the back side.

The simulated data can be reproduced fairly well by the following model: According to the stopping simulations (Tab. 5.2) the electrons are stopped within a few mm (cm) of WCu (Al), but bremsstrahlung can propagate through the slab. In our model we assume the detector only measures bremsstrahlung energy that propagated through the slab.[1] The photon transmission T_γ of a 1-in. WCu (Al) slab vs. photon energy is shown by the light-gray (dark-gray) line in Fig. 5.15 [50].

---

[1] The model will not be able to reproduce the Al data for $k_B T_e \simeq 5$ MeV where a large fraction of electrons can propagate through the slab.

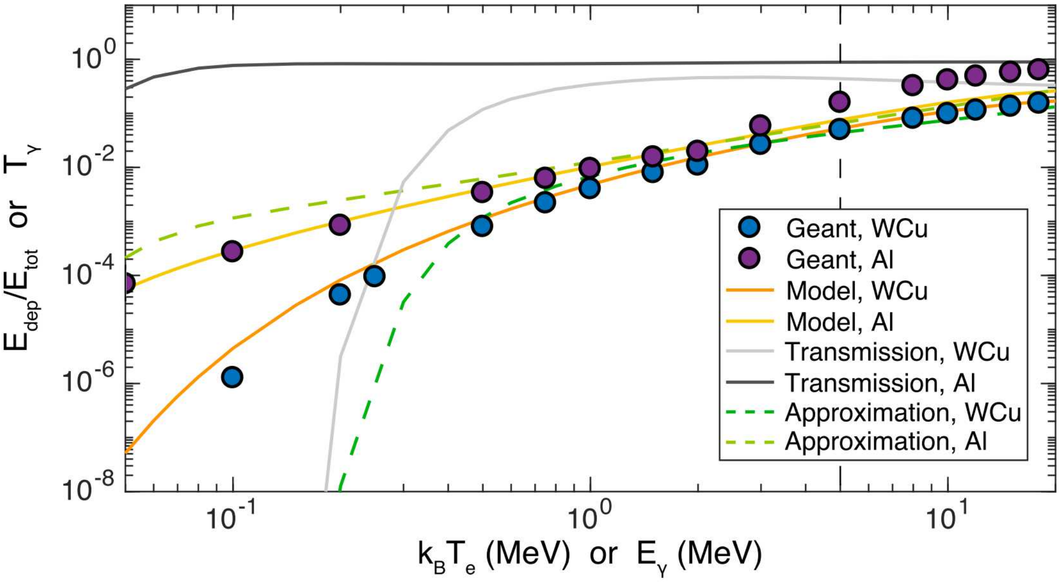

Figure 5.15. Simulated energy deposition behind a 1 in. WCu (70/30) or Al plate vs. electron source temperature. The simulation data points show the deposited energy E_{dep}; $E_{\text{tot}} = \frac{3}{2}Nk_BT_e$. The data can be reproduced by the model explained in the text. The photon transmission vs. energy is shown for comparison. Note the log-log scale of the plot.

The transmission is approximately constant ($T_\gamma(\text{WCu}) \approx 0.4$, $T_\gamma(\text{Al}) \approx 0.85$) for energies above 1 MeV (0.1 MeV for Al). For lower energies T_γ drops very steeply, much steeper than the simulated transmission results. To model the simulated data, we have to take into account the thermal distribution of electron energies (i.e., there is a high-energy tail even for low k_BT_e), the bremsstrahlung spectrum generated per electron, the efficiency of bremsstrahlung generation, and the transmission of the bremsstrahlung photons through the material. The differential bremsstrahlung spectrum is given by Kramer's law [100]:

$$\frac{dS(E_\gamma, E_e)}{dE_\gamma} = KZ\frac{E_e - E_\gamma}{E_\gamma}, \tag{5.4}$$

where E_γ (E_e) is the photon (electron) energy, and Z the atomic number of the sample ($Z = \sum w_i Z_i = 60.5$ for WCu, $Z = 29$ for Al). K is a proportionality constant that depends on E_e, the efficiency of bremsstrahlung generation, and material parameters.

To calculate K, we first take Eq. (IV-20) from [100], which yields the thick-target efficiency of Bremsstrahlung production:

$$\eta = \frac{3 \times 10^{-4} Z E_e}{1 + 3 \times 10^{-4} Z E_e}. \tag{5.5}$$

This efficiency assumes that all electrons are stopped inside the material. If the electron range is too high, not all electron energy is converted to bremsstrahlung and the efficiency term has to be reduced. This can be accomplished using the radiation length X_0, which is the mean distance over which a high-energy electron loses all but $1/e$ of its energy by bremsstrahlung. Data for X_0 were taken from published tables [95]. To correct for the efficiency reduction when the material is thicker than X_0, we define the following correction factor:

$$\varepsilon = \begin{cases} L\rho/X_0, & \text{if } L\rho/X_0 < 1, \\ 1 & \text{otherwise.} \end{cases} \tag{5.6}$$

Here L is the thickness of the material and ρ its density. Now K can easily be calculated by energy conservation. Setting the integral over all photon energies E_γ equal to the electron energy times efficiency:

$$\int_0^{E_e} E_\gamma \frac{dS(E_\gamma, E_e)}{dE_\gamma}\, dE_\gamma \doteq \varepsilon E_e, \rightarrow K = \frac{2\varepsilon\eta}{ZE_e}. \tag{5.7}$$

The so-generated spectrum of photons is then multiplied by the tabulated transmission values T_γ, and the product is integrated over all photon energies up to the energy of the impacting electron to calculate the transmitted energy $E_s(E_e)$:

$$E_S(E_e) = \int_0^{E_e} E_\gamma \frac{dS(E_\gamma, E_e)}{dE_\gamma} \times T_\gamma\, dE_\gamma. \tag{5.8}$$

The transmitted energy now needs to be multiplied by $N\, df(E_e)/dE_e$ (Eq. (5.3)) and integrated over all electron energies to obtain the total bremsstrahlung energy behind the slab:

$$E_{\text{dep}} = N \int_0^{\infty} E_s(E_e) \times \frac{df(E_e)}{dE_e}\, dE_e. \tag{5.9}$$

The final result (in *absolute units*) is plotted by the orange (yellow) line in Fig. 5.15. The calculation matches the simulated data very well.

For rough order-of-magnitude estimates we can now derive a scaling law for E_{dep} vs. k_BT_e. We set $\varepsilon = \eta = 1$. This results in $E_S(E_e) \propto T_\gamma E_e^2$. E_e roughly corresponds to the mean energy of the Maxwell-Boltzmann distribution (Eq. (5.3)), which is $3/2k_BT_e$. Additionally, for $E_e = k_BT_e$, the Maxwell-Boltzmann distribution $df/dE_e \propto 1/k_BT_e$, and therefore

$$E_{\text{dep}} \propto T_\gamma N k_B T_e. \tag{5.10}$$

This scaling is shown by the dashed lines in Fig. 5.15. It matches the Al data fairly well, except for temperatures above ≈5 MeV where electrons can escape the back side. The WCu data is reproduced well for temperatures above 0.4 MeV. Below 0.4 MeV, the approximation breaks down because here the high-energy tail of the Maxwell-Boltzmann distribution still produces some signal.

5.5.3 Enclosure simulations

Based on the PACMAN background simulation results, a full source enclosure with sufficient thickness can be used to stop the source electrons with minimal bremsstrahlung generation and to reduce direct exposure to acceptable levels. Simulations were performed to assess the impact of different shielding configurations. As described in Sec. 5.5.2, an isotropic source was placed in the Chama chamber with $k_B T_e = 2\,\mathrm{MeV}$ and we measured the energy deposition inside the PACMAN. The source was enclosed in an aluminum box with 1 inch thick walls and a 1 inch cube of empty space in the center for the source. For simplicity, the box had no openings for the laser in- or output. The results are shown in Table 5.4.

Compared to a baseline run without any additional shields, the Al enclosure reduces the background by 74 %. Counter-intuitively, switching to a W box of the same size (and much more weight) lowers the signal by only an additional 2 %. The model presented above results in an additional 11 % signal reduction, which is close to the Geant data. This represents the benefit of stopping electrons with low-Z vs. high-Z (≈30× less bremsstrahlung expected from theory). Adding material to the front shield yields diminishing returns, as indirect exposure becomes the dominant source for energy entering the PACMAN enclosure. For example, for the 5.08-cm W shield, 38% of the deposited energy pass through PACMAN top or bottom, 10% of the deposited energy pass through the PACMAN wall, but still 59% of energy pass through the PACMAN front shield.

A direct shielding result can reduce the theoretical exposure by up to 99%; unfortunately, 99.9%+ reduction may be required for a reasonable signal to noise ratio. The nature of the Maxwell-Boltzmann distribution makes this difficult. For a 2 MeV source, 0.1% of the source electrons have energies in excess of 16 MeV (with associated high-energy bremsstrahlung), which are very difficult to shield against given the volume and mass constraints inherent to our system. It is therefore recommended to develop a low-Z enclosure (e.g., aluminum) with at least 2 inch tungsten on the front to significantly reduce exposure relative to the tested tungsten enclosure or no enclosure at all.

Table 5.4. This table shows the reduction in energy deposition in the PACMAN when the source is surrounded by a 1 inch aluminum/tungsten enclosure, and for Al with an additional tungsten shield of a given thickness between the source and the PACMAN enclosure. This reduction is relative to a source with no enclosure or shielding.

Shield Thickness	Percentage Reduction
Al box, 0 cm W (no shield)	74%
W box, 0 cm W (no shield)	72%
Al box, 5.08 cm W	98%
Al box, 10.8 cm W	99%

5.5.4 Magnetic source deflection

Finally, as an alternative approach to prevent electrons from hitting the PACMAN front, we considered magnetically deflecting the source electrons rather than blocking them. Electrons can be easily deflected with a magnetic field. To test which field strengths and magnetic field volumes are required, simulations with a magnetic field from a standard Helmholtz coil pair were performed. The 5-inch diameter coils were separated by 5 inches. Rather than simulating a full chamber, we simulated an isotropic point source 5 inches from an image plane, which is approximately the distance between source and PACMAN front shield when a polycapillary lens is used. We tracked where particles struck the image plane, counting hits in the central 160 mm × 100 mm (roughly the front-facing area of the PACMAN enclosure) as deposited in PACMAN. This allowed us both to approximate the deposition in PACMAN and assess how the field deflects particles overall. The magnetic field was simulated between the source and the image plane, but no actual coil was included in the geometry, so electron-coil collisions are ignored.

We simulated with no magnetic field, creating the reference image shown in Figure 5.16 (top left), then repeated with 0.5 and 1.0 tesla (uniform) fields. The 0.5 tesla field reduced exposure in the PACMAN area by 99.5%, while the 1.0 tesla field successfully deflected all of the electrons. Creating a 1.0 tesla Helmholtz coil of this volume, however, would present a significant challenge due to the large currents involved. Lastly, we considered an approach using a laser-driven current loop to create a strong short-lived field. We based the simulated field strength and duration on [101], while the field shape was approximated as the field from a circular current loop, described in [102]. Based on these sources, we simulated a field from a 0.5 mm radius coil with a peak field of 100 tesla and a 28 ns (exponential) time decay constant. As before, no physical coil was simulated, so electron-coil collisions are ignored, and the results were not sensitive to the decay constant used for the field over a plausible range of values.

We explored a range of loop positions and orientations relative to the source–image plane axis. We treated the source–image plane axis as the Z-axis, and the X-axis as PACMAN's short axis ("height"). In this framework, the optimal orientation found in our (non-exhaustive) search was to rotate the current loop 53° about the Y-axis, and shift the center of the loop 0.2 mm along the Z axis and 0.3 mm along the Y-axis. In essence, the loop serves as an off-axis "lens" focusing electrons away from PACMAN. In this orientation, no electrons reached PACMAN, and the image in Fig. 5.16 (bottom right) was produced. This persisted with a peak field strength as low as roughly 80 tesla.

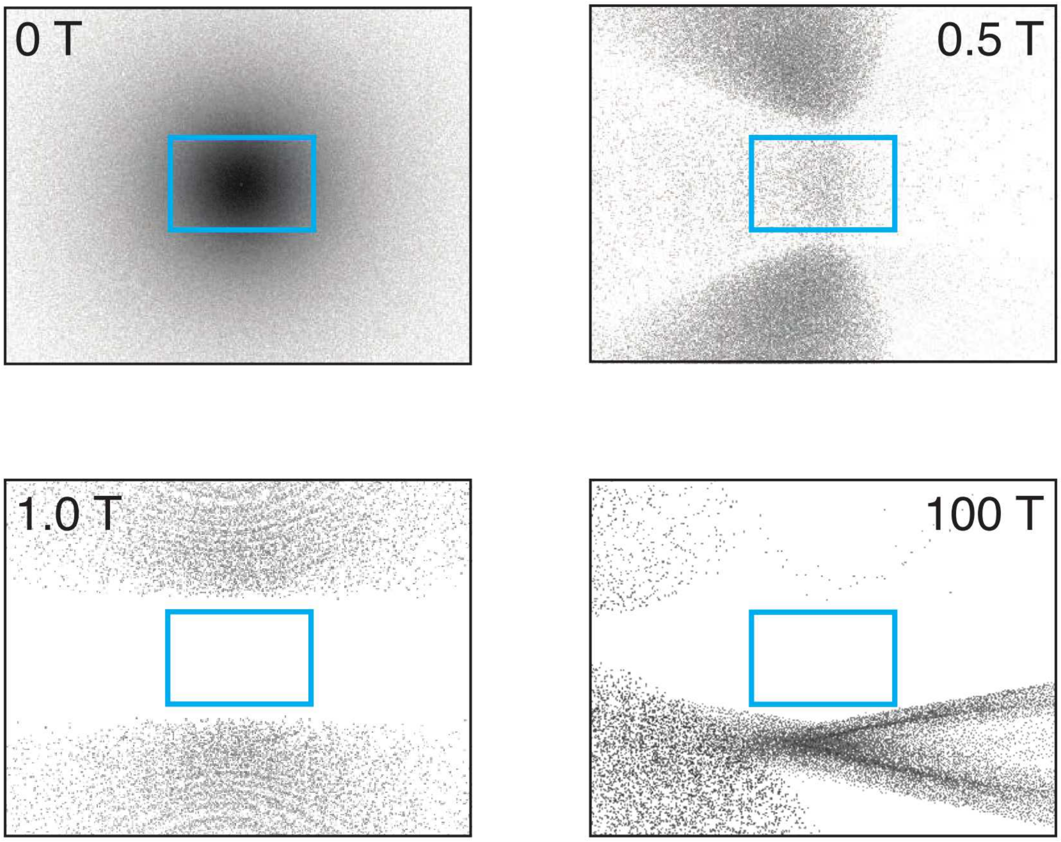

Figure 5.16. Magnetic source deflection simulation. Shown are electron locations on the plane of the PACMAN enclosure vs. magnetic field strength. The rectangle approximately represents the enclosure's profile. 0.5 T and 1 T fields could be generated with permanent dipole magnets or Helmholtz coils. The 100 T magnetic field simulation (bottom right) was based on a laser-induced current loop.

5.6 Dynamic X-ray Diffraction with ZBL

The Chaco laser was finally repaired and fully integrated into the facility shot control software in July 2018. The Chaco pulse delay was adjusted such that the rising edge of the laser pulse arrived 1 ns prior to the ZBL main pulse. This was done by placing a high-speed photodiode (Thorlabs DET025A) detector at TCC. The Chaco and ZBL alignment beams were aligned to both aim at the photodiode to adjust the timing without worrying about cable and propagation delays. After the adjustment, the Chaco beam was pointed back to irradiate the sample inside PACMAN. We confirmed that the propagation distance from the last Chaco steering mirror to TCC and to the sample inside PACMAN was identical to within a few mm (a few ps).

After the delay adjustment we set up a DXRD experiment using the PACMAN. A 25 μm thick, laser-machined Cu target with 500 μm diameter central disk served as x-ray source. The large-diameter XOS polycapillary lens was used. The sample was 27 μm Al glued onto a 12.5-mm diameter, 1064 nm AR-coated, $\lambda/4$ N-BK7 laser window (Edmund Optics #49-148). An 8.4-μm thick epoxy glue layer on top of the Al served as the pusher layer. On the combined DXRD shot, the ZBL laser energy was 1368 J. The Chaco energy was about 2 J, significantly lower than shots discussed in Sec. 5.1. A few components in the laser amplification chain were still damaged, which significantly limited the available energy.

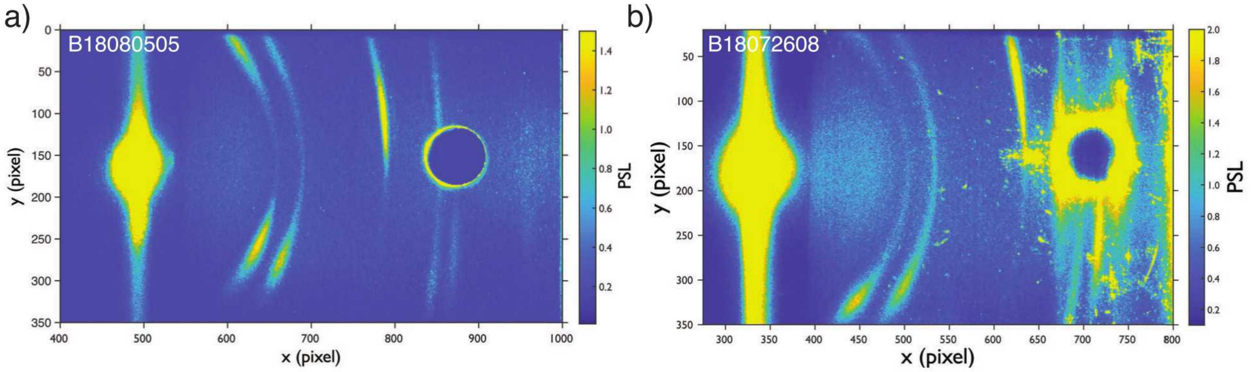

Figure 5.17. 8.4 keV dynamic x-ray diffraction pattern from an Al sample. a) Shows the XRD pattern obtained from a shot on a control sample without firing Chaco. b) Shows the IP data when Chaco was fired together with ZBL to measure an XRD pattern from a compressed sample.

Fig. 5.17a shows the XRD pattern obtained from a control sample without firing Chaco. The diffraction rings are not perfectly smooth, some areas are much brighter and broader. This is due to preferred orientation in the foil, which most likely was created when the manufacturer rolled the foils to the required thickness. The resulting PACMAN diffraction pattern from the combined shot is in shown in Fig. 5.17b. The main diffraction lines are well visible and exhibit a good signal-to-noise ratio. Towards the right side of the image the background increases significantly. This side is where Chaco enters PACMAN through the hole. The sample surface normal points in this direction and any ablated, hot material from the sample front side will propagate in this direction and create background on the IP. A potential difference in the shocked diffraction pattern due to crystal lattice compression or heating is not immediately visible. Overlapping the two patterns graphically or after integration (see Sec. 4.2) shows only a subtle difference, if any. We should point out that just before the combined system shot was performed, Chaco accidentally fired an amplified shot on the sample during a timing check because we forgot to turn off the amplifiers and block the beam, which most likely ablated the glue layer and may have damaged the Al surface. Since Chaco was not available any sooner and we were running out of time, we decided to still shoot this target because otherwise we were risking to not only miss this shot window but to potentially miss any opportunity of demonstrating a real DXRD measurement within the duration of this project.

5.6.1 Quantitative data interpretation with Rietveld structural refinement

The Rietveld method [103] refines user-selected parameters to minimize the difference between an experimental pattern (observed data) and a model based on the hypothesized crystal structure and instrumental parameters (calculated pattern). A Rietveld full profile structural refinement yields information about a single sample, including preferred orientation, a multiphase sample with the relative amounts of each phase. The Rietveld method demands high-quality experimental diffraction patterns, the choice of a structure model that makes physical and chemical sense, and the assignment of a suitable peak and background functions. We describe the crystal structure with the following parameters: space group, lattice parameters, atomic positions, atomic site occupancies, atomic thermal parameters. The instrument (diffractometer) is described by: a background, peak profile parameters (pseudo-Voigt or other profile parameters, asymmetry correction, anisotropic broadening), error correcting parameters (zero shift, specimen displacement, absorption, extinction, roughness, porosity). Each diffraction line acts as an observation. The Rietveld method fits a multivariable structure-background-profile model to experimental data. There is potential for false minima, diverging solutions, etc. The most important variables are refined first, and others are added later, until an adequate solution is realized. The correct solution may not necessarily be found. In the process of Rietveld full profile structural refinements, we aim to minimize the difference between the calculated pattern and the observed data. The goodness of the fit is assessed from a minimized difference pattern, the minimization of the residuals R, or the statistical goodness of fit or χ^2. The residuals R that are minimized during a fitting procedure are: R_{wp} or weighted residual, which is weighted to emphasize intense peaks over background, R_{exp}, which estimates the best value R for a data set (essentially an evaluation of how good the data are), and R_{Bragg}, which tries to modify the R for a specific phase.

Figure 5.18 illustrates Rietveld full profile structural refinements for both ambient XRD (left plot, B18080805) and XRD measured during the integrated shot (right plot, B18072608). Tables 5.5 and 5.6 list the corresponding Rietveld refinement results. The uncertainties on parameters originating from Rietveld refinements (unit cell parameters, unit cell volume) are taken as 3σ of the uncertainties resulting from the refinement. The ambient refinement (Fig. 5.18a) is an excellent match to the structure of aluminum at ambient pressure and temperature. Some preferred

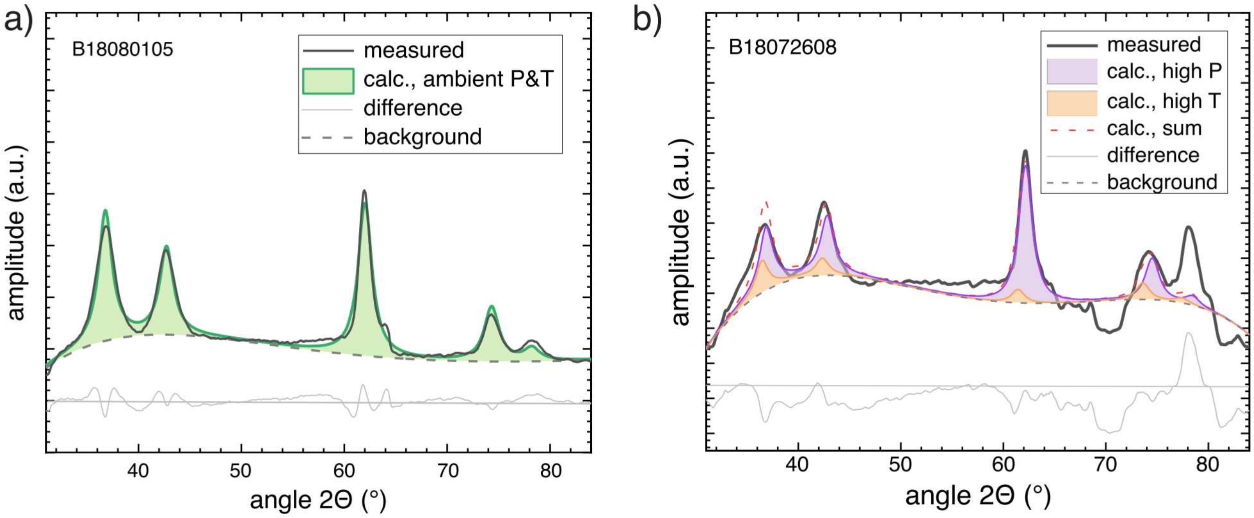

Figure 5.18. Rietveld full profile structural refinement of Al. a) shows the unshocked results with ZBL only. Pressure P and temperature T are for ambient conditions. b) shows the integrated shot with ZBL and Chaco combined. A good match is obtained using a combination of higher-than-ambient pressure and temperature.

orientation is present, which is consistent with the sample being a rolled Al foil. The Rietveld refinement of the integrated shot shown in Fig. 5.18b is a 2-phase Rietveld structural refinement. The overall refinement is good. There are some issues with background intensity at highest angles due to masking around the Chaco laser opening in the image plate. To match the data, the pattern is composed of ≈80% compressed and ≈20% heated Al phases. The Chaco laser drive causes both compression and heating: the heated Al unit cell volume increase is +2.5 % and the compressed Al unit cell volume decrease is - 0.7 % with respect to the ambient pressure (P) and temperature (T) unit cell volume. In other words, the expansion due to heating takes over the shrinking due to the compression drive. We may be detecting heating/expansion if the x-ray beam is timed too late with respect to Chaco, which first compresses the sample on the order of a few nanoseconds. Latent heating propagates within the sample on a time scale longer than the shock pulse.

Table 5.5. Results of Rietveld full profile refinement for the ambient shot (#B18080805).

100 wt.% Al, ambient p & T							
Crystal system	cubic					a (Å)	4.056(9)
Space group	Fm$\bar{3}$m (#225)					V (Å^3)	66.8(5)
Z	2					ρ (g/cm^3)	2.69(2)
						R_{wp}	6.71
Label	Site	x	y	z	Atom	Occupancy	B (temp)
Al1	4a	0	0	0	Al	1	1.414

Table 5.6. Results of Rietveld full profile refinement for the integrated shot (#B18072608).

80 wt.% compressed Al							
Crystal system	cubic					a (Å)	4.05(1)
Space group	Fm$\bar{3}$m (#225)					V (Å^3)	66.3(6)
Z	2					ρ (g/cm^3)	2.70(2)
						R_{wp}	17.44
Label	Site	x	y	z	Atom	Occupancy	B (temp)
Al1	4a	0	0	0	Al	1	1

20 wt.% expanded Al							
Crystal system	cubic					a (Å)	4.09(4)
Space group	Fm$\bar{3}$m (#225)					V (Å^3)	68.5(7)
Z	2					ρ (g/cm^3)	2.62(3)
						R_{wp}	17.44
Label	Site	x	y	z	Atom	Occupancy	B (temp)
Al1	4a	0	0	0	Al	1	1

This page intentionally left blank.

6. CONCLUSIONS

6.1 Summary of Accomplishments

This LDRD project required significant infrastructure developments, such as the activation of a target chamber for three large laser systems, development of several diagnostic instruments, their operating procedures and work planning and control (WP&C) documentation. New capabilities developed during this project include:

- Commissioning of the Chama target chamber for experiments with either one or all of the three laser systems Chaco, ZBL and ZPW.
- Demonstration that lens-based focusing of ZPW is a viable option to generate K_α x-rays.
- Development of a laser compression platform using direct drive or flyer impact compression with the Chaco laser.
- Development of a high-shot rate (up to 3 ZBL + 3 ZPW shots/day) DXRD platform for Sandia.
- Demonstration that x-ray polycapillary lenses are an enabling technology for DXRD on Z.
- Development of a 1064-nm Photonic Doppler Velocimetry system that is compatible with facility laser safety regulations.
- Installation of a single photon counter diagnostic and CRITR spectrometer as standard diagnostics for all ZBL/ZPW experiments in Chama, which direct comparisons between both laser systems and a quick determination if an x-ray source is suitable for XRD.
- Development of XRD-specific analysis codes and photometric calculations for quantitative data analysis.

We have achieved about 6 GPa sample pressure in standalone laser-compression experiments, which should be sufficient to drive for example the $\gamma - \alpha$ iso-structural phase transition in cerium. After repair of still-damaged laser components and small improvements (e.g., a more-efficient 2ω conversion crystal), we expect that Chaco should be able to drive samples to 10–20 GPa, which is directly comparable to gas guns and will enable very interesting comparisons due to different strain rates of the two approaches.

We have shown that both ZBL and ZPW can be used to perform DXRD experiments at 8 keV x-ray energy. A first demonstration experiment was performed, where Chaco was used to compress an Al sample and ZBL was used to generate the x-ray source. From an operational standpoint, there is no difference if ZPW or ZBL are fired together with Chaco, which means that the platform is ready for DXRD experiments. Polycapillary lenses were found to be essential for successful XRD with ZPW, but they also offer great benefits for ZBL experiments due to the increase in x-ray collection efficiency and increased shielding distance compared to a pinhole collimator. With a polycapillary lens, we have demonstrated 16-keV XRD with ZBL on a high-Z sample.

6.2 Path Forward

X-ray diffraction has become a key measurement on a variety of platforms across the nation. It was, however, less than obvious whether such a capability could be enabled on the Z facility, largely because we do not have a free electron laser, a synchrotron x-ray source, or tens of kJ of laser light (as on Omega or NIF) to create the x-ray source needed for diffraction. This LDRD looked at methods to see whether $\approx$1 kJ of laser energy could be used to create sufficient x-rays for diffraction measurements. While it is still uncertain whether the strong background radiation on Z can be overcome sufficiently to enable this measurement, this LDRD has succeeded in pushing the frontiers of what is possible using x-ray sources available to the programs on Z.

Specifically, we envision that polycapillary lenses will be included in the existing 6–8 keV x-ray diffraction instrument developed for Z, as well as other diagnostics such as for example backlighter radiography or x-ray self-emission imaging. Within the next few years, polycapillary lenses will enable XRD experiments with x-ray energies above 10 keV using the proven ZBL laser to generate the x-ray source on Z.

The ZPW laser is currently undergoing an upgrade to full aperture, which will enable short-pulse laser experiments at 1–2 kJ laser energy. If the final focusing optic is exchanged by an off-axis parabolic mirror, ZPW will be able to operate in a very large range of intensities from below 10^{16} W/cm^2 up to 10^{20} W/cm^2. This will help determining the optimum laser intensity, which balances K_α generation efficiency and background generation.

In addition to that, the DXRD experiment will be re-designed to include the new polycapillary lenses with longer output focal length (50 cm and 100 cm). The longer system length will allow us to add significantly more shielding between the laser target and PACMAN (or a PACMAN2). It will also generate enough distance to place an electron deflection magnet between source and sample for bremsstrahlung reduction at the faceplate of PACMAN. Before the experimental hardware will be built, the newly developed Geant4 simulation capability can be used to simulate the effects of various source parameters in order to optimize shielding and reduce the detector background.

A successful demonstration of DXRD with the long-focus polycapillary lenses in Chama experiments paves the way for XRD on Z that require a dedicated containment device. The polycapillary lenses can be used to inject x-rays through a small entrance port in the containment device and to guide the x-rays to the sample.

REFERENCES

[1] D. V. Morgan, M. Grover, D. Macy, M. Madlener, G. Stevens, and W. D. Turley. *Observations of shocked metal surfaces with single-pulse x-ray diffraction*. Tech. Rep., International Centre for Diffraction Data (2010). 15

[2] P. A. Rigg and Y. M. Gupta. *Time-resolved x-ray diffraction measurements and analysis to investigate shocked lithium fluoride crystals*. Journal of Applied Physics **93**, 3291 (2003). 15

[3] D. V. Morgan, D. Macy, and G. Stevens. *Real-time x-ray diffraction measurements of shocked polycrystalline tin and aluminum*. Review of Scientific Instruments **79**, 113904 (2008).

[4] B. R. Maddox, M. C. Akin, A. Teruya, D. Hunt, D. Hahn, J. Cradick, and D. V. Morgan. *Single-pulse x-ray diffraction using polycapillary optics for in situ dynamic diffraction*. Review of Scientific Instruments **87**, 083901 (2016). 49, 56

[5] P. Kalita, P. Specht, S. Root, N. Sinclair, A. Schuman, M. White, A. L. Cornelius, J. Smith, and S. Sinogeikin. *Direct Observations of a Dynamically Driven Phase Transition with in situ X-Ray Diffraction in a Simple Ionic Crystal*. Physical Review Letters **119**, 255701 (2017).

[6] S. J. Tracy, S. J. Turneaure, and T. S. Duffy. *In situ X-Ray Diffraction of Shock-Compressed Fused Silica*. Physical Review Letters **120**, 135702 (2018). 15

[7] D. Milathianaki, S. Boutet, G. J. Williams, A. Higginbotham, D. Ratner, A. E. Gleason, M. Messerschmidt, M. M. Seibert, D. C. Swift, P. Hering, et al. *Femtosecond visualization of lattice dynamics in shock-compressed matter.* Science **342**, 220 (2013). 15

[8] D. Kraus, A. Ravasio, M. Gauthier, D. O. Gericke, J. Vorberger, S. Frydrych, J. Helfrich, L. B. Fletcher, G. Schaumann, B. Nagler, et al. *Nanosecond formation of diamond and lonsdaleite by shock compression of graphite.* Nature Communications **7**, 10970 (2016).

[9] J. Wang, F. Coppari, R. F. Smith, J. H. Eggert, A. E. Lazicki, D. E. Fratanduono, J. R. Rygg, T. R. Boehly, G. W. Collins, and T. S. Duffy. *X-ray diffraction of molybdenum under ramp compression to 1 TPa*. Physical Review B **94**, 104102 (2016).

[10] C. E. Wehrenberg, D. McGonegle, C. Bolme, A. Higginbotham, A. Lazicki, H. J. Lee, B. Nagler, H.-S. Park, B. A. Remington, R. E. Rudd, et al. *In situ X-ray diffraction measurement of shock-wave-driven twinning and lattice dynamics*. Nature Communications **550**, 496 (2017). 15

[11] D. H. Kalantar, J. F. Belak, G. W. Collins, J. D. Colvin, H. M. Davies, J. H. Eggert, T. C. Germann, J. Hawreliak, B. L. Holian, K. Kadau, et al. *Direct Observation of the α-e Transition in Shock-Compressed Iron via Nanosecond X-Ray Diffraction*. Physical Review Letters **95**, 075502 (2005). 15, 16, 75

[12] J. R. Rygg, J. H. Eggert, A. E. Lazicki, F. Coppari, J. A. Hawreliak, D. G. Hicks, R. F. Smith, C. M. Sorce, T. M. Uphaus, B. Yaakobi, et al. *Powder diffraction from solids in the terapascal regime.* Review of Scientific Instruments **83**, 113904 (2012). 40, 43

[13] B. R. Maddox, H.-S. Park, J. Hawreliak, A. Elsholz, R. van Maren, B. A. Remington, A. Comley, and J. S. Wark. *Bragg diffraction using a 100 ps 17.5 keV x-ray backlighter and the Bragg diffraction imager*. Review of Scientific Instruments **81**, 10E522 (2010). 92

[14] A. Higginbotham, P. G. Stubley, A. J. Comley, J. H. Eggert, J. M. Foster, D. H. Kalantar, D. McGonegle, S. Patel, L. J. Peacock, S. D. Rothman, et al. *Inelastic response of silicon to shock compression*. Scientific Reports **6**, 24211 (2016). 15

[15] M. J. Suggit, A. Higginbotham, J. A. Hawreliak, G. Mogni, G. Kimminau, P. Dunne, A. J. Comley, N. Park, B. A. Remington, and J. S. Wark. *Nanosecond white-light Laue diffraction measurements*

of dislocation microstructure in shock-compressed single-crystal copper. Nature Communications **3**, 1224 (1). 15

[16] A. J. Comley, B. R. Maddox, R. E. Rudd, S. T. Prisbrey, J. A. Hawreliak, D. A. Orlikowski, S. C. Peterson, J. H. Satcher, A. J. Elsholz, H.-S. Park, et al. *Strength of Shock-Loaded Single-Crystal Tantalum [100] Determined using* In Situ *Broadband X-Ray Laue Diffraction*. Physical Review Letters **110**, 115501 (2013).

[17] F. Zucchini, S. N. Bland, C. Chauvin, P. Combes, D. Sol, A. Loyen, B. Roques, and J. Grunenwald. *Characteristics of a molybdenum X-pinch X-ray source as a probe source for X-ray diffraction studies*. Review of Scientific Instruments **86**, 033507 (2015). 15

[18] M. K. Matzen, M. A. Sweeney, R. G. Adams, J. R. Asay, J. E. Bailey, G. R. Bennett, D. E. Bliss, D. D. Bloomquist, T. A. Brunner, R. B. Campbell, et al. *Pulsed-power-driven high energy density physics and inertial confinement fusion research*. Physics of Plasmas **12**, 055503 (2005). 15

[19] M. E. Cuneo, M. C. Herrmann, D. B. Sinars, S. A. Slutz, W. A. Stygar, R. A. Vesey, A. B. Sefkow, G. A. Rochau, G. A. Chandler, J. E. Bailey, et al. *Magnetically Driven Implosions for Inertial Confinement Fusion at Sandia National Laboratories*. IEEE Transactions on Plasma Science **40**, 3222 (2012). 15

[20] J.-P. Davis, C. Deeney, M. D. Knudson, R. W. Lemke, T. D. Pointon, and D. E. Bliss. *Magnetically driven isentropic compression to multimegabar pressures using shaped current pulses on the Z accelerator*. Physics of Plasmas **12**, 056310 (2005). 15

[21] R. W. Lemke, M. D. Knudson, D. E. Bliss, K. Cochrane, J.-P. Davis, A. A. Giunta, H. C. Harjes, and S. A. Slutz. *Magnetically accelerated, ultrahigh velocity flyer plates for shock wave experiments*. Journal of Applied Physics **98**, 073530 (2005).

[22] C. T. Seagle, J.-P. Davis, M. R. Martin, and H. L. Hanshaw. *Shock-ramp compression: Ramp compression of shock-melted tin*. Applied Physics Letters **102**, 244104 (2013). 15

[23] P. Rambo, J. Schwarz, M. Schollmeier, M. Geissel, I. Smith, M. Kimmel, C. Speas, J. Shores, D. Armstrong, J. Bellum, et al. *Sandia's Z-Backlighter Laser Facility*. Proc. of SPIE **10014**, 100140Z (2016). 15, 26

[24] P. K. Rambo, I. C. Smith, J. L. Porter, M. J. Hurst, C. S. Speas, R. G. Adams, A. J. Garcia, E. Dawson, B. D. Thurston, C. Wakefield, et al. *Z-Beamlet: a multikilojoule, terawatt-class laser system*. Applied Optics **44**, 2421 (2005). 16

[25] P. K. Rambo, D. J. Armstrong, J. Schwarz, I. C. Smith, J. E. Shores, C. S. Speas, and J. L. Porter. *Injection of a Phase Modulated Source into the Z-Beamlet Laser for Increased Energy Extraction*. Tech. Rep. SAND2014-20011, Sandia National Laboratories (2014). 16

[26] J. Schwarz, P. Rambo, M. Geissel, M. Kimmel, E. Brambrink, B. Atherton, and J. Glassman. *A hybrid OPCPA/Nd: phosphate glass multi-terawatt laser system for seeding of a petawatt laser*. Optics Communications **281**, 4984 (2008). 16

[27] J. Schwarz, P. Rambo, M. Geissel, A. Edens, I. Smith, E. Brambrink, M. Kimmel, and B. Atherton. *Activation of the Z-petawatt laser at Sandia National Laboratories*. Journal of Physics: Conference Series **112**, 032020 (2008). 16

[28] J. D. Colvin and D. H. Kalantar. *Scaling of Pressure with Intensity in Laser-Driven Shocks and Effects of Hot X-Ray Preheat*. AIP Conference Proceedings **845**, 1413 (2006). 16, 31

[29] A. Silber, *Adaptive Project Management*, Leading Complex and Uncertain Projects (BookLocker.com, St. Petersburg, Florida, 2017). 19

[30] J. Schwarz, P. Rambo, M. Geissel, M. Kimmel, M. Schollmeier, I. Smith, J. Bellum, D. Kletecka, A. Sefkow, D. Smith, et al. *Z-Backlighter facility upgrades: a path to short/long pulse, multi-frame, multi-color x-ray backlighting at the Z-Accelerator*. Proc. SPIE **8080**, 80800E (2011). 26

[31] D. B. Sinars, D. F. Wenger, S. A. Pikuz, B. Jones, M. Geissel, S. B. Hansen, C. A. Coverdale, D. J. Ampleford, M. E. Cuneo, L. A. McPherson, et al. *Compact, rugged in-chamber transmission*

spectrometers (7–28 keV) for the Sandia Z facility. Review of Scientific Instruments **82**, 063113 (2011). 27, 28, 79

[32] E. S. Field, J. C. Bellum, and D. E. Kletecka. *How reduced vacuum pumping capability in a coating chamber affects the laser damage resistance of* HfO_2*/*SiO_2*antireflection and high-reflection coatings*. Optical engineering **56**, 011005 (2017). 29

[33] A. D. Curtis, A. A. Banishev, W. L. Shaw, and D. D. Dlott. *Laser-driven flyer plates for shock compression science: Launch and target impact probed by photon Doppler velocimetry*. Review of Scientific Instruments **85**, 043908 (2014). 33, 75

[34] H. Kiriyama, M. Mori, Y. Nakai, T. Shimomura, H. Sasao, M. Tanaka, Y. Ochi, M. Tanoue, H. Okada, S. Kondo, et al. *High-spatiotemporal-quality petawatt-class laser system.* Applied Optics **49**, 2105 (2010). 33

[35] W. W. Simmons, D. R. Speck, and J. T. Hunt. *Argus laser system: performance summary.* Applied Optics **17**, 999 (1978). 34

[36] W. Seka, J. Soures, O. Lewis, J. Bunkenburg, D. Brown, S. Jacobs, G. Mourou, and J. Zimmermann. *High-power phosphate-glass laser system: design and performance characteristics.* Applied Optics **19**, 409 (1980). 34

[37] J. Caird. *Advanced conceptual design report for the Z-Beamlet laser backlighter*. Tech. Rep. UCRL-ID-134409, Lawrence Livermore National Laboratory (LLNL), Livermore, CA (United States) (1999). 35

[38] K. Strehl. *Über Luftschlieren und Zonenfehler*. Zeitschrift für Instrumentenkunde **22**, 213 (1902). 36

[39] O. T. Strand, D. R. Goosman, C. Martinez, T. L. Whitworth, and W. W. Kuhlow. *Compact system for high-speed velocimetry using heterodyne techniques*. Review of Scientific Instruments **77**, 083108 (2006). 38

[40] T. Ao and D. H. Dolan. *SIRHEN: A data reduction program for photonic Doppler velocimetry measurements*. Tech. Rep. SAND2010-3628, Sandia National Laboratories (2010). 38

[41] D. H. Dolan. *Accuracy and precision in photonic Doppler velocimetry*. Review of Scientific Instruments **81**, 053905 (2010). 38

[42] M. F. Ahmed, A. House, R. F. Smith, J. Ayers, Z. S. Lamb, and D. W. Swift. *X-ray diffraction diagnostic design for the National Ignition Facility*. Proc. SPIE **8850**, 88500N (2013). 40

[43] R. M. Vignes, M. F. Ahmed, J. H. Eggert, A. C. Fisher, D. H. Kalantar, N. D. Masters, C. A. Smith, and R. F. Smith. *TARDIS-C: A target diagnostic for measuring material structure at high pressure*. Journal of Physics: Conference Series **717**, 012115 (2016). 40

[44] M. D. Knudson and R. W. Lemke. *Shock response of low-density silica aerogel in the multi-Mbar regime*. Journal of Applied Physics **114**, 053510 (2013). 41

[45] W. L. Bragg, *The Diffraction of Short Electromagnetic Waves by a Crystal*, vol. 17 (Proceedings of the Cambridge Philosophical Society, 1912). 41

[46] G. Fiksel, F. J. Marshall, C. Mileham, and C. Stoeckl. *Note: Spatial resolution of Fuji BAS-TR and BAS-SR imaging plates*. Review of Scientific Instruments **83**, 086103 (2012). 43

[47] T. Ao, E. C. Harding, J. E. Bailey, G. Loisel, S. Patel, D. B. Sinars, L. P. Mix, and D. F. Wenger. *Relative x-ray collection efficiency, spatial resolution, and spectral resolution of spherically-bent quartz, mica, germanium, and pyrolytic graphite crystals*. Journal of Quantitative Spectroscopy and Radiative Transfer **144**, 92 (2014). 43

[48] L. R. Benedetti, J. H. Eggert, J. D. Kilkenny, D. K. Bradley, P. M. Bell, N. E. Palmer, R. B. Petre, B. F. Heidl, J. R. Rygg, T. R. Boehly, et al. *Conceptual design for time-resolved x-ray diffraction in a single laser-driven compression experiment*. AIP Conference Proceedings **1979**, 160004 (2018). 43

[49] M. Schollmeier, M. Geissel, P. K. Rambo, J. Schwarz, A. Sefkow, M. Vargas, and J. L. Porter, *Development of a shortpulse laser-driven 15.7 keV x-ray probe for bent-crystal imaging and spectroscopy*

(2013), URL `http://absimage.aps.org/image/DPP13/MWS_DPP13-2013-000590.pdf`. 44, 61

[50] J. H. Hubbell and S. Seltzer, *X-Ray Mass Attenuation Coefficients*, NIST (1996), URL `https://www.nist.gov/pml/x-ray-mass-attenuation-coefficients`. 44, 96

[51] M. Bargheer, N. Zhavoronkov, R. Bruch, H. Legall, H. Stiel, M. Woerner, and T. Elsaesser. *Comparison of focusing optics for femtosecond X-ray diffraction*. Applied Physics B **80**, 715 (2005). 48, 49

[52] M. A. Kumakhov and F. F. Komarov. *Multiple reflection from surface X-ray optics*. Physics Reports (Review Section of Physics Letters) **191**, 289 (1990). 48

[53] D. Gibson and W. Gibson. *Polycapillary optics: An enabling technology for new applications*. Tech. Rep., International Centre for Diffraction Data (2002).

[54] P. J. Schields, D. M. Gibson, W. M. Gibson, N. Gao, H. Huang, and I. Y. Ponomarev. *Overview of polycapillary X-ray optics*. Powder Diffraction **17**, 70 (2002). 49, 52

[55] C. A. MacDonald. *Focusing Polycapillary Optics and Their Applications*. X-Ray Optics and Instrumentation **2010**, 867049 (2010). 48, 49

[56] I. V. Tomov, J. Chen, X. Ding, and P. M. Rentzepis. *Efficient focusing of hard X-rays generated by femtosecond laser driven plasma*. Chemical Physics Letters **389**, 363 (2004). 49

[57] R. Tommasini, R. Bruch, E. Fill, and A. Bjeoumikhov. *Convergent-beam diffraction of ultra-short hard X-ray pulses focused by a capillary lens*. Applied Physics B **82**, 519 (2006).

[58] L. Miaja-Avila, G. C. O'Neil, J. Uhlig, C. L. Cromer, M. L. Dowell, R. Jimenez, A. S. Hoover, K. L. Silverman, and J. N. Ullom. *Laser plasma x-ray source for ultrafast time-resolved x-ray absorption spectroscopy*. Structural Dynamics **2**, 024301 (2015). 49

[59] P. Mabey, N. J. Hartley, H. W. Doyle, J. E. Cross, L. Ceurvorst, A. Savin, A. Rigby, M. Oliver, M. Calvert, I. J. Kim, et al. *Characterization of x-ray lens for use in probing high energy density states of matter*. Journal of Instrumentation **10**, P04010 (2015). 49

[60] B. L. Henke, E. M. Gullikson, and J. C. Davis. *X-Ray Interactions: Photoabsorption, Scattering, Transmission, and Reflection at E = 50-30,000 eV, Z = 1-92*. Atomic Data and Nuclear Data Tables **54**, 181 (1993). 51, 69

[61] M. Schollmeier, A. B. Sefkow, M. Geissel, A. V. Arefiev, K. A. Flippo, S. A. Gaillard, R. P. Johnson, M. W. Kimmel, D. T. Offermann, P. K. Rambo, et al. *Laser-to-hot-electron conversion limitations in relativistic laser matter interactions due to multi-picosecond dynamics*. Physics of Plasmas **22**, 043116 (2015). 56

[62] C. Stoeckl, W. Theobald, T. C. Sangster, M. H. Key, P. Patel, B. B. Zhang, R. Clarke, S. Karsch, and P. Norreys. *Operation of a single-photon-counting x-ray charge-coupled device camera spectrometer in a petawatt environment*. Review of Scientific Instruments **75**, 3705 (2004). 61

[63] C. Stoeckl, V. Y. Glebov, P. A. Jaanimagi, J. P. Knauer, D. D. Meyerhofer, T. C. Sangster, M. Storm, S. Sublett, W. Theobald, M. H. Key, et al. *Operation of target diagnostics in a petawatt laser environment (invited)*. Review of Scientific Instruments **77** (2006). 61

[64] B. Westover, A. MacPhee, C. Chen, D. Hey, T. Ma, B. Maddox, H. Park, B. Remington, and F. Beg. *Study of silver Kα and bremsstrahlung radiation from short-pulse laser-matter interactions with applications for x-ray radiography*. Physics of Plasmas **17**, 082703 (2010). 61, 83

[65] A. D. Edens. *PCD cal analysis*. Tech. Rep. Memo, (unpublished), Sandia National Laboratories (2008). 61

[66] M. Schollmeier, M. Geissel, and A. D. Edens. *25 keV tin K-shell radiation conversion efficiency studies with a single photon counting x-ray CCD detector*. Tech. Rep. Memo, (unpublished), Sandia National Laboratories (2009). 61, 63

[67] C. Kittel and P. McEuen, *Introduction to Solid State Physics*, 8th Edition (John Wiley & Sons, Inc, 1996), ISBN 0-471-41526-x. 65

[68] W. Kraus and G. Nolze. *POWDER CELL - a program for the representation and manipulation of crystal structures and calculation of the resulting X-ray powder patterns*. J. Appl. Cryst. **29**, 301 (1996). 66

[69] C. Prescher and V. B. Prakapenka. *DIOPTAS: a program for reduction of two-dimensional X-ray diffraction data and data exploration*. High Pressure Research **35**, 223 (2015). 67

[70] D. H. Dolan, T. Ao, and S. C. Grant. *The Sandia Matlab AnalysiS Hierarchy (SMASH) toolbox*. Tech. Rep. SAND2016-6848, Sandia National Laboratories (2016). 67

[71] M. J. Berger, J. H. Hubbell, S. Seltzer, J. Chang, J. S. Coursey, R. Sukumar, D. S. Zucker, and K. Olsen, *XCOM: Photon Cross Sections Database*, NIST (2018), URL `https://www.nist.gov/pml/xcom-photon-cross-sections-database`. 69

[72] E. G. Zukas, R. A. Pereyra, and J. O. Willis. *The Gamma to Alpha Phase Transformation in Cerium*. Metallurgical Transactions A **18**, 35 (1987). 73

[73] R. L. Snyder and D. L. Bish, *Reviews in Mineralogy, Volume 20*, Modern Powder Diffraction (Mineralogical Society of America, 1989), ISBN 0-939950-24-3. 73

[74] R. J. Trainor, J. W. Shaner, J. M. Auerbach, and N. C. Holmes. *Ultrahigh-Pressure Laser-Driven Shock-Wave Experiments in Aluminum*. Physical Review Letters **42**, 1154 (1979). 75

[75] W. M. Trott, R. E. Setchell, and A. V. J. Farnsworth. *Development of Laser-Driven Flyer Techniques for Equation-of-State Studies of Microscale Materials*. AIP Conf. Proc. **620**, 1347 (2002). 75

[76] J. E. Bailey, T. Ao, E. Harding, S. B. Hansen, M. P. Desjarlais, R. W. Lemke, G. A. Rochau, J. Reneker, and D. Romero. *X-Ray Thomson Scattering Measurements of Warm Dense Matter*. Tech. Rep. SAND2012-7998, Sandia National Laboratories, Albuquerque (2012). 78

[77] D. B. Sinars, G. R. Bennett, M. C. Herrmann, I. C. Smith, C. S. Speas, L. E. Ruggles, and J. L. Porter. *Enhancement of x-ray yield from the Z-Beamlet laser for monochromatic backlighting by using a prepulse*. Review of Scientific Instruments **77** (2006). 78, 81

[78] D. Babonneau, M. Primout, F. Girard, J.-P. Jadaud, M. Naudy, B. Villette, S. Depierreux, C. Blancard, G. Faussurier, K. B. Fournier, et al. *Efficient multi-keV X-ray sources from laser-exploded metallic thin foils*. Physics of Plasmas **15**, 2702 (2008). 78

[79] J. Workman and G. A. Kyrala. *Scaling of x-ray K-shell sources from laser-solid interactions*. Proc. SPIE **4504**, 168 (2001). 78

[80] L. E. Ruggles, J. L. Porter, P. K. Rambo, W. W. Simpson, M. F. Vargas, G. R. Bennett, and I. C. Smith. *Measurements of 4-10 keV x-ray production with the Z-Beamlet laser*. Review of Scientific Instruments **74**, 2206 (2003). 81

[81] M. A. Barrios, K. B. Fournier, S. P. Regan, O. Landen, M. May, Y. P. Opachich, K. Widmann, D. K. Bradley, and G. W. Collins. *Backlighter development at the National Ignition Facility (NIF): Zinc to zirconium*. High Energy Density Physics **9**, 626 (2013). 78

[82] M. S. Schollmeier. *PhD thesis: Optimization and control of laser-accelerated proton beams*. Ph.D. thesis, Technische Universitaet Darmstadt, Darmstadt (2008). 78

[83] T. Kluge, T. Cowan, A. Debus, U. Schramm, K. Zeil, and M. Bussmann. *Electron Temperature Scaling in Laser Interaction with Solids*. Physical Review Letters **107** (2011). 78

[84] P. M. Nilson, A. A. Solodov, J. F. Myatt, W. Theobald, P. A. Jaanimagi, L. Gao, C. Stoeckl, R. S. Craxton, J. A. Delettrez, B. Yaakobi, et al. *Scaling Hot-Electron Generation to High-Power, Kilojoule-Class Laser-Solid Interactions*. Physical Review Letters **105**, 235001 (2010). 78, 79

[85] P. M. Nilson, A. A. Solodov, J. F. Myatt, W. Theobald, P. A. Jaanimagi, L. Gao, C. Stoeckl, R. S. Craxton, J. A. Delettrez, B. Yaakobi, et al. *Scaling hot-electron generation to long-pulse, high-intensity laser–solid interactions*. Physics of Plasmas **18**, 056703 (2011).

[86] T. Ma, H. Sawada, P. Patel, C. Chen, L. Divol, D. Higginson, A. Kemp, M. Key, D. Larson, S. Le Pape,

et al. *Hot Electron Temperature and Coupling Efficiency Scaling with Prepulse for Cone-Guided Fast Ignition*. Physical Review Letters **108**, 115004 (2012). 78, 94

[87] M. S. Schollmeier, A. B. Sefkow, M. Geissel, P. K. Rambo, and J. Schwarz. *Z-Petawatt Driven Ion Beam Radiography Development*. Tech. Rep. SAND2013-7201, Sandia National Laboratories (2013).

[88] L. C. Jarrott, A. J. Kemp, L. Divol, D. Mariscal, B. Westover, C. Mcguffey, F. N. Beg, M. Suggit, C. Chen, D. Hey, et al. *Kα and bremsstrahlung x-ray radiation backlighter sources from short pulse laser driven silver targets as a function of laser pre-pulse energy*. Physics of Plasmas **21**, 031211 (2014). 78

[89] O. Culfa, G. J. Tallents, E. Wagenaars, C. P. Ridgers, R. J. Dance, A. K. Rossall, R. J. Gray, P. McKenna, C. D. R. Brown, S. F. James, et al. *Hot electron production in laser solid interactions with a controlled pre-pulse*. Physics of Plasmas **21**, 043106 (2014). 78

[90] A. L. Meadowcroft, C. D. Bentley, and E. N. Stott. *Evaluation of the sensitivity and fading characteristics of an image plate system for x-ray diagnostics*. Review of Scientific Instruments **79**, 3102 (2008). 79, 84

[91] B. R. Maddox, H.-S. Park, B. A. Remington, N. Izumi, S. Chen, C. Chen, G. Kimminau, Z. Ali, M. J. Haugh, and Q. Ma. *High-energy x-ray backlighter spectrum measurements using calibrated image plates*. Review of Scientific Instruments **82**, 023111 (2011).

[92] M. J. Haugh, J. Lee, E. Romano, and M. Schneider. *Calibrating image plate sensitivity in the 700 to 5000 eV spectral energy range*. Proc. SPIE **8850**, 885007 (2013). 79

[93] A. H. Gabriel. *Dielectronic Satellite Spectra for Highly-Charged Helium-Like Ion Lines*. Monthly Notices of the Royal Astronomical Society **160**, 99 (1972). 79

[94] H.-S. Park, D. M. Chambers, H. K. Chung, R. J. Clarke, R. Eagleton, E. Giraldez, T. Goldsack, R. Heathcote, N. Izumi, M. H. Key, et al. *High-energy Kα radiography using high-intensity, short-pulse lasers*. Physics of Plasmas **13**, 056309 (2006). 81, 82, 83

[95] M. Tanabashi, K. Hagiwara, K. Hikasa, K. Nakamura, Y. Sumino, F. Takahashi, J. Tanaka, K. Agashe, G. Aielli, C. Amsler, et al. *Review of Particle Physics*. Physical Review D **98**, 030001 (2018). 91, 98

[96] Geant4 Collaboration, S. Agostinelli, J. Allison, K. Amako, J. Apostolakis, H. Araujo, P. Arce, M. Asai, D. Axen, S. Banerjee, et al. *Geant4-a simulation toolkit*. Nuclear Instruments and Methods in Physics Research Section A **506**, 250 (2003). 93

[97] Geant4 Collaboration, *Physics Reference Manual* (2017). 93

[98] D. E. Cullen, J. H. Hubbell, and L. Kissel. *EPDL97: the Evaluated Photon Data Library, '97 Version*. UCRL-50400 **6** (2013). 93

[99] M. J. Berger, J. S. Coursey, M. A. Zucker, and J. Chang, ESTAR, PSTAR, and ASTAR: Computer Programs for Calculating Stopping-Power and Range Tables for Electrons, Protons, and Helium Ions (1993), URL `http://physics.nist.gov/Star`. 94, 96

[100] H. W. Koch and J. W. Motz. *Bremsstrahlung Cross-Section Formulas and Related Data*. Reviews of Modern Physics **31**, 920 (1959). 97

[101] S. Fujioka, Z. Zhang, K. Ishihara, K. Shigemori, Y. Hironaka, T. Johzaki, A. Sunahara, N. Yamamoto, H. Nakashima, T. Watanabe, et al. *Kilotesla Magnetic Field due to a Capacitor-Coil Target Driven by High Power Laser*. Scientific Reports **3**, 1170 (2013). 100

[102] J. C. Simpson, J. E. Lane, C. D. Immer, and R. C. Youngquist. *Simple Analytic Expressions for the Magnetic Field of a Circular Current Loop*. Tech. Rep. NASA/TM-2013-217919, NASA (2013). 100

[103] H. M. Rietveld. *A profile refinement method for nuclear and magnetic structures*. Journal of Applied Crystallography **2**, 65 (1969). 103

DISTRIBUTION:

1 Model World LLC
Attn: Joel Long
12129 Menaul Blvd NE, Apt. 3
Albuquerque, NM 87112

1 Mission Support and Test Services, NM Operations
Attn: Dane Morgan
2900 East Road
Los Alamos, NM 87544

5	MS 1106	Tommy Ao, 1646
1	MS 1106	Sakun Duwal, 1646
1	MS 1106	Patricia Kalita, 1646
1	MS 1106	Brian Stoltzfus, 1651

1	MS 1189	John Benage, 1640
1	MS 1189	Kyle Cochrane, 1641
1	MS 1189	Jean-Paul Davis, 1646
1	MS 1189	Michael Desjarlais, 1600
1	MS 1189	Daniel Dolan, 1646
1	MS 1189	Dawn Flicker, 1640
1	MS 1189	Thomas Mattsson, 1641
1	MS 1189	Andrew Porwitzky, 1641
1	MS 1189	Christopher Seagle, 1646
1	MS 1189	Luke Shulenburger, 1641
1	MS 1189	Paul Specht, 1646
1	MS 1189	Jack Wise, 1646

1	MS 1192	Anthony Colombo, 1682
1	MS 1192	Raymond Fasano, 1682
1	MS 1192	Ella Field, 1682
1	MS 1192	Benjamin Galloway, 1682
1	MS 1192	Matthias Geissel, 1682
1	MS 1192	Michael Jones, 1691
1	MS 1192	Mark Kimmel, 1682
1	MS 1192	Quinn Looker, 1682
1	MS 1192	Patrick Rambo, 1682
1	MS 1192	John Porter, 1682
5	MS 1192	Marius Schollmeier, 1682
1	MS 1192	Jens Schwarz, 1682

1	MS 1192	Ian Smith, 1682
1	MS 1193	Daniel Sinars, 1680
1	MS 1195	Justin Brown, 1646
1	MS 1195	Michael Cuneo, 1650
1	MS 1195	Chad McCoy, 1646
1	MS 1195	Seth Root, 1646
1	MS 1195	Joshua Townsend, 1641
1	MS 1196	Gregory Rochau, 1683
1	MS 0359	D. Chavez, LDRD Office, 1171
1	MS 0899	Technical Library, 9536 (electronic copy)

Sandia National Laboratories